INFRARED LASER-MEDIATED POLYMERASE CHAIN REACTION IN A POLYMER MICROFLUIDIC DEVICE

A Thesis
Presented to
The Academic Faculty

by

Christopher R. Phaneuf

In Partial Fulfillment
of the Requirements for the Degree
Doctor of Philosophy in the
The George W. Woodruff School of Mechanical Engineering

Georgia Institute of Technology
December 2014

INFRARED LASER-MEDIATED POLYMERASE CHAIN REACTION IN A POLYMER MICROFLUIDIC DEVICE

Approved by:

Professor Craig R. Forest, Advisor
The George W. Woodruff School of Mechanical Engineering
Georgia Institute of Technology

Professor James P. Landers
Department of Chemistry
University of Virginia

Professor Suman Das
The George W. Woodruff School of Mechanical Engineering
Georgia Institute of Technology

Professor Hang Lu
School of Chemical and Biomolecular Engineering
Georgia Institute of Technology

Professor Peter J. Hesketh
The George W. Woodruff School of Mechanical Engineering
Georgia Institute of Technology

Date Approved: November 13, 2014

ACKNOWLEDGEMENTS

There are many people to thank for supporting me during my graduate career. First, I want to thank my family for being a constant source of love, encouragement, and inspiration. To my mother for being the core of my family and always setting an example of hard work, honesty, and strength. To my father for teaching me the fun of tinkering, the value of curiosity, and the satisfaction of craftsmanship. To my sister, Whitney, for supporting my academic pursuits and opening my eyes to the worlds of music and art. To my twin brother, Alex, for his kindness, passion, and originality. I am lucky to have such a talented and loving brother.

Thank you to the past and present members of the Precision Biosystems Laboratory. To my advisor, Craig Forest, for taking a risk and hiring me as his first graduate student. His enthusiasm for research has been infectious and his commitment to solving real problems with creative solutions has been inspiring. In addition, I am grateful for the energy he invests in the future success and happiness of his students. To Melissa Li, for answering my endless questions during my early days in the lab, for helping ignite my love of science, and for being the champion swimmer on the lab triathlon team. To Nikita Pak, for being a tireless researcher while working with me as both an undergraduate and graduate student, for sharing my love of bad movies, for being a great friend, and for being the dominant (and shamefully fresh-legged) runner on the lab triathlon team. To Curtis Saunders, for the patient and rigorous work he conducted mostly in darkness and for the unparalleled history knowledge he brought to the lab trivia team (Half Human Half Walrus!). And to the many other lab members who helped along the way, including Mike Dergance, Suhasa Kodandaramaiah, Greg Holst, Nicholas Sondej, Matthew Marchese, Matt Emerick,

Steven Culpepper, Jamison Go, Nikita Nagpal, Joav Birjiniuk, and Nathan Hotaling.

Thank you to the members of the Landers Lab at the University of Virginia. For being generous and helpful collaborators. For allowing me to spend a summer in your lab to share knowledge and absorb your many pioneering techniques. Specifically, I want to thank James Landers, Dan Leslie, Brian Poe, Kyudam Oh, and Jenny Lounsbury.

Thank you to the masters of the BME Machine Shop, Mark McJunkin and Marty Jacobson. For their valuable design advice and for creating a workspace in which I was afforded the tools and freedom to thrive as a fabricator.

Thank you to the CDC employees who believed in our ideas and supported our research as collaborators. For welcoming me into their facilities for a week to observe their workflow. For performing supplementary experiments and providing an endless supply of precious reagents. Specifically, I want to thank Suxiang Tong, Susan Ruone, and Christina Chommanard.

Thank you to the Emory / CHOA employees who helped secure seed funding for our research. For showing us an environment in which diagnostic technologies are actually implemented and providing insight into how the diagnostic process can improve. For patiently working with us to get IRB approval and providing clinical specimens. Specifically, I want to thank Andi Shane and Robert Jerris for their efforts.

Lastly, I want to thank some of the great friends I made while living in Atlanta, including David Torello, Drew Owen, Ashley Allen, Hommood Alrowais, Becky Katz, and BJ Muldrey.

TABLE OF CONTENTS

LIST OF TABLES

LIST OF FIGURES

SUMMARY

The ability to rapidly, sensitively, and accurately detect the presence of a pathogen is a vital capability for first responders in the assessment and treatment of scenarios such as disease outbreak and bioterrorism. Nucleic acid tests such as the polymerase chain reaction (PCR) are supplanting traditional techniques due to the improved speed, specificity, sensitivity, and simplicity. Still, amplification by PCR is often the bottleneck when processing genetic samples. Conventional PCR machines are bulky, slow, and consume large reagent volumes and an affordable, compact, efficient, easy-to-use alternative has yet to emerge.

In this work, a microfluidic PCR platform was developed consisting of a low-cost, multi-chamber polymer microchip and a laser-mediated thermocycler capable of independent thermal control of each reaction chamber. Innovations in polymer microchip modeling, fabrication, and characterization yielded a low-cost solution for sample handling. A simple optical system featuring an infrared laser diode and solenoid-driven optical shutter was combined with a microfluidic temperature measurement system utilizing embedded thermocouples to achieve rapid thermocycling capable of multiplexed temperature control. We validated the instrument with sensitive amplifications of multiple viral targets simultaneously. This technology is a breakthrough in practical microfluidic PCR instrumentation, providing the foundation for a paradigm shift in low-cost, high-throughput genetic diagnostics.

CHAPTER I

INTRODUCTION

1.1 Motivation

Viral respiratory, gastrointestinal, and encephalitis diseases are often associated with significant morbidity and mortality. Diagnoses of the agents responsible for cases of these diseases are difficult because the clinical symptoms for different pathogens are often similar or indistinguishable. For example, the SARS virus, responsible for the first pandemic of the 21st century, exhibits non-specific respiratory infection symptoms [1]. The current epidemic of Ebola virus in West Africa is another example of the dangers of a pathogen known to present symptoms easily confused with other infectious agents [2, 3]. The need for timely diagnosis of infections, which applies to not only these extreme cases but also to the routine care provided by hospitals and clinics everywhere, is not being adequately met by current detection technologies.

This thesis focuses on the development of a microfluidic platform capable of rapid, parallelized genetic sample sample preparation, representing a milestone in the performance and accessibility of diagnostic tools. Efforts were focused on the design, fabrication, and validation of a practical, reliable, and affordable instrument capable of sensitive, multiplexed virus detection while minimizing reagent consumption and maximizing ease-of-use.

1.2 Polymerase chain reaction

Traditional techniques for virus detection include immunoassays, direct fluorescent antigen testing, and viral culturing. These methods are still widely used but suffer

from numerous limitations. For example, culturing a virus can take 3–30 days, requires trained personnel, and clinical trials have shown this method to be less sensitive than modern alternatives [4, 5, 6]. Gradually, the bench tops of microbiology labs are evolving with our increasing knowledge of genetics and the appearance of assays and accompanying instrumentation that harness the power of nucleic acid tests for faster, more reliable diagnoses.

One such technique is the polymerase chain reaction (PCR), which provides a highly specific and sensitive method for exponentially amplifying a DNA sequence from as little as a single copy by thermocycling a biochemical cocktail [7]. PCR has become a ubiquitous tool in the fields of biology and medicine for countless applications involving the study of nucleic acids, including forensics, personalized medicine, and pathogen detection for scenarios ranging from routine clinical care to outbreak response and surveillance [8].

The essential reagents for performing PCR include buffer solution, $MgCl_2$, dNTPs (dATP, dCTP, dGTP, dTTP), a thermostable polymerase, primers, and the template nucleic acid (either DNA or RNA that has a complementary strand generated via reverse transcription, also known as cDNA) containing the sequence of interest. The key discovery that enabled this technique was the use of polymerase enzyme isolated from the thermophilic bacterium *Thermus aquaticus*, known as *Taq* polymerase. This enzyme can survive the high temperatures required for denaturing DNA, a necessary step for the replication process. The specificity of PCR is based on the primers, which are short oligonucleotides (typically around 20 bases in length) that bracket the sequence of interest.

PCR is a temperature-driven process, with the sample undergoing thermocycling, where each cycle consists of three critical phases: 1) Heating to the DNA denaturing temperature of 95°C, separating the strands; 2) Cooling to the annealing temperature, which is determined by characteristics of the primer set and typically ranges

from 40–70°C, allowing primers to anneal to the template strands; 3) Heating to the extension temperature of the polymerase, which is typically 72°C, where dNTPs are incorporated to generate complimentary strands to complete the replication. At each phase, the sample is maintained at the corresponding temperature to allow time for the biochemical activity to take place. These three phases are repeated for n cycles (typically around 30), to achieve a 2^n fold increase in the sequence being amplified. In practice, the reaction does not perform with perfect efficiency and $final\ copy\ number$ can be represented as $starting\ copy\ number \times (1 + E)^n$, where E represents the efficiency of the reaction.

Conventional PCR thermocyclers make use of a thermoelectric heating / cooling system to control the temperature of an aluminum block, which features cavities typically sized for standard 0.2 mL polypropylene PCR tubes and allows for temperature cycling of the samples contained in those tubes. These instruments have been a mainstay in laboratories working with nucleic acids for many years and remain extremely common for their ease of use and reliability. Still, there are numbers opportunities for innovations to overcome the limitations of conventional thermocyclers, including the large required reaction volumes (>5 µL), slow analysis time (>30 min), and susceptibility to thermal inconsistencies [9, 10]. Further, despite the high sample capacities of most PCR instruments, operation is typically limited to uniform thermal conditions and, in some case, a thermal gradient can be used, which is almost exclusively employed for the process of developing reaction protocols. Yet, different genetic targets have corresponding optimal annealing temperatures that depend on the sequence length and GC content of their primers. Consequently, conventional instruments only allow a single type of reaction or multiple reactions that can work at the same conditions, which cannot always be easily accommodated. Some thermoelectric instruments can generate a temperature gradient across a set of samples but

the method remains slow and cannot achieve arbitrary, independently selectable conditions. As such, this feature has only penetrated niche applications such as primer annealing temperature optimization.

Having described the fundamentals of PCR, there are several variants to review that are relevant to this work. When faced with the task of screening samples for multiple targets, a standard PCR reaction will only amplify a single target, requiring a time-consuming serial process of sample preparation and thermocycling. A solution to this problem is a technique known as multiplex PCR, which was developed in the 1980s [11] and has since become commonplace. Using multiplex PCR, one can amplify multiple gene targets simultaneously using multiple primer sets designed for a common annealing temperature in a single PCR mixture. Drawbacks to multiplex PCR most notably include amplification bias due to efficiency variations, PCR drift, and the high likelihood of primer-primer interactions [12, 13]. In addition, skilled primer design and finely tuned reagent concentrations are required and cannot always accommodate all desired target sequences [14].

Another variant is consensus degenerate PCR, a form of "broad" PCR. Instead of utilizing known pathogen genomic signatures to detect known pathogens, this technique is capable of effectively identifying novel emerging pathogens or unsuspected pathogens. The Centers for Disease Control and Prevention (CDC) use this method for both routine screening and for the discovery of novel viruses. The method involves designing specialized primers, known as consensus degenerate hybrid oligonucleotide primers (CODEHOP), for targeting highly conserved regions across a viral family and/or genera [15, 16, 17, 18]. Briefly, consensus degenerate primers work by observing conserved motifs in the protein sequences of a gene family. From this, a pool of primers is designed with a common 5' end, known as the consensus clamp that contains a "best guess" sequence for the nucleotides flanking the target motif, and a heterogeneous 3' end, known as the degenerate core region containing all possible

codons for 3–4 amino acids. This methodology not only amplifies nucleic acids from known pathogens but also detects related novel pathogens due to the evolutionary relationships of the organisms.

In parallel with the use of our technology for virus detection, we explored its application to the challenge of rapid gene expression measurement in collaboration with researchers studying stem cell differentiation. Gene expression measurement is an essential tool for molecular biology studies. For example, understanding gene expression patterns is fundamental to the study of mechanisms underlying stem cell pluripotency and self-renewal [19, 20]. A variety of tools have been developed for quantitative gene expression analysis across many genes and many cells. DNA microarrays allow one to probe virtually the entire transcriptome [21] and have become widely used in profiling expression of hundreds to hundreds of thousands of genes [22], although results can be noisy [23, 24]. Fluorescence *in-situ* hybridization (FISH) is commonly used when knowledge about the spatial distribution of gene expressions in cells or tissues is necessary and has been done in fixed [25] and live [26] cells and has been advanced further using quantum dots [27] and fluorescent tags [28]. However, scalability of this technology to multiple genes in multiple cells and tissues is hindered by expensive equipment and the need for long recording times and high-intensity illumination [25]. RNA sequencing technologies can be used to map a sample with no prior knowledge of the samples genome by directly counting number of reads [29], albeit at relatively high cost and long measurement duration.

The limited sensitivity, slow turnaround, and high costs of these techniques have led to the common practice of gene expression profiling with another variant of PCR known as quantitative, reverse transcription, polymerase chain reaction (qRT-PCR) [30]. This technique, now widely regarded as the "gold standard," allows for highly specific, sensitive, and reproducible RNA quantification with a high dynamic range by reverse transcribing RNA into DNA and then exponentially amplifying the target

sequence from as little as a single copy by thermally cycling, or thermocycling, a biochemical cocktail.

Miniaturized, or microfluidic, PCR systems have focused primarily on either increasing the number of genes able to be simultaneously measured [30, 24], increasing the sensitivity of the system to single-cell analyses [31, 32, 33, 34, 35, 36, 37], or developing systems with sample-in answer-out capabilities [38, 39, 40, 41, 42, 43]. Reports of large sample arrays [30, 24, 44] of sub-microliter reaction chambers have been published for high-throughput qRT-PCR that amplify as few as 5 starting copies of RNA in each chamber, effectively bridging the gap between the high-throughput capabilities of microarrays and the sensitivity of qPCR [30]. In addition, researchers have worked to expand the spatial frequency of single-cell analysis by separating and measuring the gene expression of 300 single cells simultaneously [33].

While these tools are powerful, they require hours or days per analysis. However, gene expression patterns can change across a broad range of timescales, from slow events during development and pathogenesis (i.e., hours to days) to rapid responses to environmental signals (i.e., minutes to hours) [45, 32, 46]. If the measurement frequency can approach the gene expression timescales, real-time observation and intervention becomes possible. There is therefore a need for technologies capable of high temporal frequency sampling, governed by the Nyquist rate, to measure gene expression kinetics in single cells or cell populations in real-time.

1.3 Microfluidic PCR

While PCR has become the gold standard for genetic sample preparation, it is often more expensive than conventional approaches [47]. Louie et al. [48] estimates the cost of PCR, when considering reagents, equipment, dedicated space, personnel training, and labor, to be as high as $125 per reaction. In order to reduce PCR costs, reducing the reaction volume or diluting the reaction mixture offer potential

solutions but these approaches face a number of obstacles. For example, conventional PCR tubes are impractical for volumes less than 5 µL due to issues such as in-tube evaporation and inadequate heat transfer due to the reduced ratio of heated surface area to open air surface area of the samples. In addition, at these low volumes, difficulties with accurate sample handling and dilution have been shown to produce low-quality PCR products [49, 50]. Microfluidics presents the ideal solution for handling smaller volumes, not only preserving precious reagents, therefore reducing costs, but also reducing the thermal mass of the system, enabling faster thermal response and lower power consumption compared to macroscale equivalents. Potential drawbacks to the use of microfluidics for PCR can include the high surface-area-to-volume ratios (SA:V) exhibited by typical microfluidic geometries. This can present problems such as exaggerated surface chemistry phenomena and unfavorable parasitic heat loss that creates problems for isolating heat generation on-chip.

Microfluidic PCR devices, which emerged in the late 1980s and early 1990s [51, 52, 53, 43], have proven to be effective tools in the research setting and, to some extent, commercially for handling lower volumes and providing faster turnaround times [54, 55]. The low thermal mass of the microfluidic reaction volumes not only enable faster thermal response but can also help increase specicity due to reduced transition times between PCR steps and improved temperature uniformity throughout the sample [56]. Other advantages include integration of upstream and downstream sample processing on the same device [43, 39, 57, 58] and portability for point-of-care applications [59, 60, 40, 61].

Planar microchips for PCR, some of the earliest appearing in the mid-1990s [52], have become the preferred format. These devices can be made from a variety of substrates, such as silicon, glass, and, more recently, polymers including poly(methyl methacrylate) (PMMA), cyclic olefin copolymers (COC), polycarbonate (PC), polyethylene terephthalate (PET), and polydimethylsiloxane (PDMS); PMMA,

PC, COC, and PE are microfluidic substrates that fall in the "glassy polymers" category. The advantages and disadvantages for common microfluidic substrates can be seen in Table 1. Microfluidic device fabrication in polypropylene is rare, though not unheard of [30], because of the challenges of material shaping processes for micro-scale features and bonding. Microchips are fabricated using a wide range of techniques such as chemical etching [62, 63], thermoforming [64, 65], casting [66], and laser etching [67].

Table 1: Comparison of relevant properties of substrate materials for microchips used for PCR.

	glass	**PDMS**	**PET**	**PMMA**
cost	\$40	\$2	\$0.15	\$0.50
fabrication time	24 hrs	24 hrs	<10 min	2 hrs
batch fabricated?	yes	yes	no	no
reproducibility	moderate	excellent	good	excellent
durability	low	moderate	low	high
biochemical compatibility	excellent	good	limited	limited

Despite the many advances in the field of microfluidic PCR, there are factors limiting large-scale adoption. For instance, while PCR recipes typically call for a polymerase concentration of 0.02–0.025 U/µL, the recipes for microfluidic PCR frequently require 2–20× more than the conventional polymerase concentration [68, 38, 69]. Within the field of virology, demonstrations of such devices are typically limited to common amplifications at relatively high starting template concentrations (e.g., 0.1–100 ng) [70, 71, 58]. More challenging reactions that are useful in clinical and research settings, such as broad-range PCR using consensus degenerate primers, have not been widely demonstrated with microfluidic systems. Ideally, innovations in the fabrication and characterization of polymer microfluidics can produce a device capable of attaining sensitivity and specificity comparable to conventional PCR tubes without the need to increase polymerase or template concentration.

1.4 Laser-mediated PCR

The task of integrating heating systems with microdevices has been carried out at various degrees of accuracy and complexity. The implementation and effectiveness of the heat transfer modes: conductive, convective, and radiative, depend on material selection, fabrication allowances, and the performance requirements of the respective application. While many microfluidic devices have increased throughput with smaller sample volumes, they continue to rely on conventional conductive heating from macroscale thermoelectric heating blocks [54, 72]. Resistive [73, 62] and convective [74] heating have also been implemented. The Roche LightCycler makes use of circulating hot air to perform thermocycling for 10 µL samples contained in glass capillaries [75].

Radiative heating has been utilized for faster, more controllable microfluidic heating systems for applications including PCR (as the primary [76] or supplementary [77, 78] heat source), cell lysis [79], liquid handling via melting of wax valves [80], and DNA trapping via thermophoresis [81, 82]. Configurations range from broadband sources to focused, monochromatic sources and offers the unique advantage of direct, non-contact heating for greater efficiency and ramping rates as compared with resistive and convective heating instruments. Broadband sources such as a tungsten filament lamp can provide fast thermocycling of small volumes for rapid PCR [39, 71, 76, 83]. Laser-mediated radiative heating offers similar advantages and has been demonstrated for rapidly thermocycling droplets [84, 85, 77]. The smaller spatial scales and faster heating and cooling rates of microfluidic PCR systems can complicate temperature sensing and control. Techniques used in previous work include reference chambers with thermocouples [76], uorescent dyes [85], pyrometers [86], resistance measurements [73], and open-loop control [87].

Of the heat transfer modes for microchip temperature control, radiative heating offers several unique advantages. By matching a source of radiation to strongly

absorptive wavelengths of a particular liquid, radiative heating efficiently transfers energy to the medium of interest and can yield rapid temperature ramping (e.g., 32 °C/s for water [77]). Additionally, an external source keeps microchip design and fabrication simple and mediates the risks of adsorption and reaction inhibition due to the presence of incompatible materials embedded in the device, as encountered in other microfluidic heating schemes [62]. The external source also makes a disposable microchip platform more feasible. The Landers group at the University of Virginia has pioneered the use of radiative, or non-contact, temperature cycling for genetic analysis instrumentation. For example, using a tungsten filament lamp, sample volumes of 270 nL can be thermocycled 25 times in only 5 min to achieve high-speed PCR. Other developments in radiative heating include the work of Yasuda [77] and Faris [84], using infrared laser radiation to perform real-time PCR in 10-30 nL droplets suspended in mineral oil with amplification times of 3.5 and 6 min, respectively. This approach represents great potential for fast, high-throughput microfluidic solutions for temperature-dependent processes.

1.5 Functional requirements

Based on the many challenges of achieving rapid, affordable, and commercially viable detection of genetic targets, we devised a microfluidic PCR platform with a set of functional requirements to be addressed in each proceeding Chapter. To summarize, our PCR platform must enable:

Microfluidic sample handling: Repeatably load 1 µL sample volumes in a microchip without the need for external pumps.

Thermocycling: Control sample temperature within a 0.5°C tolerance for repeated denaturing at 94°C, annealing over a range of 40–70°C, and extension at 72°C.

DNA amplification: Perform sensitive amplification at clinically relevant template starting copy numbers by combining accurate thermocycling with strategies for minimizing sources of inhibition such as bubble formation and reagent loss due to surface adsorption.

Thermal multiplexing: Independently control sample temperature to perform PCR amplification of two distinct genetics targets simultaneously.

This final functional requirement requires some elaboration. By exploiting the degree of optical control of our temperature control system and the thermal isolation achieved with our polymer microchip, we devised an alternative to traditional multiplex PCR for targeting multiple gene sequences via "thermal multiplexing," in which the reaction temperatures for an array of samples are controlled independently to achieve multiple, distinct thermal profiles for multiple, optimal amplifications. The end goal is the same as the biochemical approach of multiplex PCR: by targeting multiple sequences at once, additional information may be gained from a single amplification run that otherwise would require more time and reagents. Unlike traditional multiplex PCR, thermally multiplexed PCR does not require specialized reaction design and allows the consolidation of any set of pre-existing reactions into a single instrument run.

In this work we present a system designed for thermally multiplexed PCR comprising a simple, pressurized microfluidic chip, an infrared laser thermocycler that allows for direct heating of the samples, and a closed-loop temperature control method. We demonstrate the ability of this system to simultaneously generate different annealing temperatures in a microchip using a single radiative heat source. We model, characterize, and apply this system to amplifications for a pair of distinct DNA targets as a demonstration.

To perform thermally multiplexed PCR, a heat source is uniformly distributed,

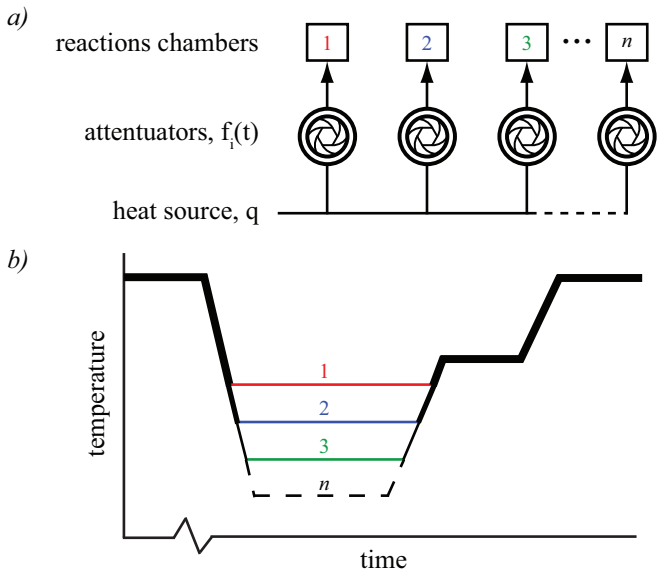

Figure 1: (a) Thermal multiplexing can be generalized to a uniformly distributed and independently attenuated heat source delivered to an array of reaction chambers. (b) Theoretical temperature profiles for n reactions illustrating the capability of maintaining a set of distinct annealing temperatures simultaneously for optimal amplification of unique DNA targets.

independently and arbitrarily modulated, and directed to an array of reaction chambers as depicted in Figure 1a. The heat source delivers a constant power, q, divided equally amongst n chambers as q/n. Each attenuator (e.g., optical shutter, valve, filter, variable resistor) modulates the power q/n according to a unique programmed function (e.g., pulse width modulated square wave), $f_i(t)$ for $1 < i < n$ and $0 f_i(t) 1$. Each chamber is thus heated to temperature profile $T_i(t)$, shown in Figure 1b, by the power profile $q_i(t) = (q/n) f_i(t)$.

CHAPTER II

DISPOSABLE PCR MICROCHIP

In the development of a viable microfluidic technology that offers not only high performance but ease of use and affordability, the most critical element is the microfluidic device. This chapter will describe the process of designing, fabricating, and testing a microchip for laser-mediated PCR. Design efforts were driven by finite element modeling, which helped identify the most desirable material properties and geometries for the device. A non-traditional approach to fabrication via micro-milling allowed us to rapidly iterate designs and yield geometries unattainable by conventional methods. Towards the implementation of the device for viral screening applications, a thorough characterization of biochemical compatibility with PCR reagents was undergone to arrive at a low-cost polymer microchip capable of rapid and efficient amplification of genetic targets.

2.1 Design

As a starting point for the design of our microfluidic device, a basic layout was established for the device consisting of three essential features required for static PCR: a reaction chamber where the microfluidic sample would be isolated and subjected to thermocycling, ports for loading the sample into the device (i.e., world-to-chip interface), and fill channels for transporting the sample from the ports to the reaction chamber. In order to size these features, select appropriate materials and fabrication methods, and develop the necessary treatments and protocols for the implementation of this device, extensive modeling and experimental characterization was employed.

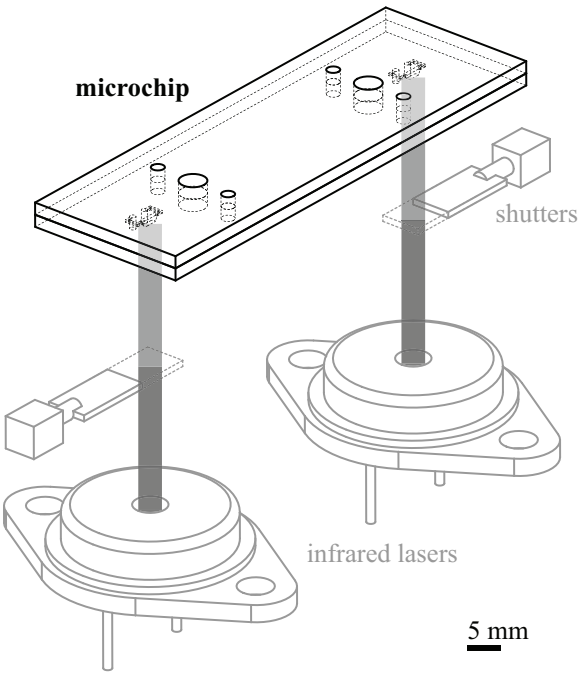

Figure 2: A simplified version of our dual-laser microfluidic PCR system. The microchip, featuring two 1 µL reaction chambers, is aligned over two infrared lasers with mechanical shutters positioned in the optical paths for modulation of radiation. (Optics, pressurization, and temperature sensors excluded for clarity.)

2.1.1 Optical and heat transfer model of radiative heating

Controlling the temperature of liquids in a microfluidic device is often a critical functional requirement in the design of miniaturized systems for biological analyses. In addition to the precise temperature control required for PCR thermocycling, Inducing elevated temperatures is commonly utilized for cell lysis [88, 89], protein denaturation [90], heat shock DNA transformation [91], and activating the lambda red genetic pathway for homologous recombination experiments [92]. Generating reliable dynamic thermal conditions is also important for applications such as melting curve analysis and enzyme reaction control [93]. Therefore, a modeling tool for the reliable prediction of thermal response in a microfluidic device would be valuable for the design of any of these technologies.

Developing such a tool was an important first step towards the deterministic design our microchip platform. A combination of analytical and finite element models

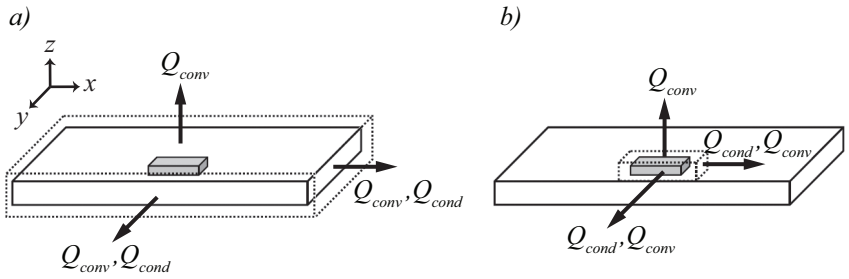

Figure 3: Control volumes for thermal modeling can include either (a) both the reaction chamber and surrounding substrate, where the dominant in-plane heat transfer mode is convection, or (b) only the reaction chamber, where the dominant in-plane heat transfer mode is conduction through the substrate.

were used to predict the thermal behavior of a microchip, notably the sample and its microenvironment, when subjected to a radiation source. The start point for this effort was to examine previous work on glass microchips in which reaction chamber design was optimized using heat transfer analysis that modeled the sample and immediately surrounding substrate as an *effective medium* for a simple lumped capacitance treatment [94]. From there, a more generalized approach was taken to model the steady state and transient behavior for radiative heating in a microchip. Specifically, we used optical modeling to determine the theoretically absorbed input radiation then applied closed-form analytical equations and finite element methods to model the thermal responses for specific cases of aqueous samples in glass and polymer microchips irradiated by broadband blackbody and monochromatic sources. We compared these models with experimental measurements. These generalized models apply to any source, materials, and geometry for which the optical and material properties are known.

Modeling was performed for the radiative heating of a simplified microchip consisting of a pair of closely spaced reaction chambers containing liquid samples surrounded by a substrate material. Control volumes were drawn either around both the chamber and immediately surrounding material, for the *effective medium* approach (Figure 3a), or only around the reaction chamber (Figure 3b).

Since virtually all microfluidic devices are fabricated with thin substrates, heat transfer out of the plane (z-direction) is dominated by convection. In-plane heat transfer (x-y plane) will involve both conduction and convection and the relative dominance of one or the other depends heavily on the thermal properties of the substrate material and area over which radiative heating occurs. Without making any presumptions regarding the appropriateness of a particular model, both lumped capacitance and finite element methods were applied.

The initial modeling approach applied the assumption that both the liquid sample and surrounding material are at a uniform temperature, corresponding to the control volume illustrated in Figure 3a. This problem has known boundary conditions and can be solved with lumped capacitance treatment, for which an energy balance is applied as

$$V\rho c_p \frac{\mathrm{d}T}{\mathrm{d}t} = Q_{rad,in} - Q_{cond,out} - Q_{conv,out} - Q_{rad,out} \ , \tag{1}$$

where

$$Q_{cond,out} = \frac{k_s A_{cond} \Delta T}{L} \ , \tag{2}$$

$$Q_{conv,out} = hA_{conv}\Delta T \ , \tag{3}$$

and

$$Q_{rad,out} = FA_t\varepsilon_s\sigma\left(T^4 - T_\infty^4\right). \tag{4}$$

With the exception of $Q_{rad,in}$, the terms of the energy balance differential equation are detailed in previous literature that describes the optimization of a glass microchip design [94]. Briefly, T is the temperature, V is the total volume of the heated region, and material properties such as density, ρ, and specific heat at constant pressure, c_p, which apply to the entire effective medium, are calculated with mass-weighted averages of the constituent liquid and solid properties. $Q_{cond,out}$ is the conduction losses to unheated parts of the microchip (if applicable), given by Equation 2 in

which k_s is the thermal conductivity of the substrate, A_{cond} is the cross-sectional area at the interface, and L is the length of the conducting region in the direction of conduction. $Q_{conv,out}$ is the free convection out, given by Equation 3 where A_{conv} is the total convecting surface area of the medium and h is the heat transfer coefficient. This is calculated from the Nusselt number, which is found using an empirical correlation with the Rayleigh and Prandtl numbers based on the particular geometry of the convecting body. $Q_{rad,out}$ is the radiation out, calculated by Equation 4, where F is the shape factor, A_t is the total exposed area of the control volume, ε_s is the emissivity of the medium, and σ is the Stefan-Boltzmann constant.

The theoretical radiation into the control volume, $Q_{rad,in}$, was calculated from the optical properties of the source and the geometric and absorptive properties of the absorbing media. For the source, spectral irradiance data was scaled by integrating over its full spectrum and equating it to the known total power output. This yielded the scaled spectral power distribution, $P_0(\lambda)$. The losses due to reflection at the air-glass and glass-water interfaces were calculated to be 4% and 0.5% respectively based on simplified reflection coefficient equations for near-normal incidence. Using absorption coefficients, $\alpha(\lambda)$, of the absorbing media and the path length, l, through which the radiation travels, the absorbed power $P_{abs}(\lambda)$ was calculated using the Beer-Lambert law as $P_{abs}(\lambda) = P_0(\lambda)(1 - 10^{-\alpha(\lambda)l})$. This was integrated with respect to wavelength and, in the case that the focal spot was larger than the control volume, adjusted for the incident area and, if necessary, the intensity distribution, in turn providing the radiative power into the control volume. For the spatial and temporal scales we are concerned with in this study, the quasi-Gaussian distribution of the laser and the lamp focal spots were assumed uniform. The sum of all absorbing bodies that constitute the effective medium yields $Q_{rad,in}$.

Considerations when determining the radiant power from an incandescent lamp included the power supply dependent spectral curve, which shifts towards blue with

higher power. Calculations accounting for this shift within our practical power range indicated a negligible effect (e.g., less than 5%) on the final absorbed radiation calculation.

Equation 1 was first solved algebraically for the steady state temperature of the effective medium $\left(\frac{\mathrm{d}T}{\mathrm{d}t} = 0\right)$. The energy balance was solved for $T(t)$ using an explicit numerical method, specifically Runge-Kutta via MATLAB's *ode*45 solver, to calculate the transient response.

The second modeling approach applied the assumption that thermal gradients in the substrate cannot be neglected and the control volume must be drawn as in Figure 3b. This is relevant for cases in which either the substrate does not readily absorb the spectral range of the source or the spatial distribution of the radiation is highly localized to the chamber. Modeling such a scenario was best accomplished with finite element analysis.

The geometry of the microchip was first created in COMSOL finite element software and divided into subdomains and boundaries, each of which was assigned the specific parameters of the problem. Subdomains were assigned appropriate material properties, along with a heat generation value for each absorbing subdomain. This heat generation term was calculated from the same optical modeling described above for determining $Q_{rad,in}$ in the previous approach, which must then be divided by the volume of the absorbing region for units of W/m^3. For the exterior boundary conditions, a heat transfer coefficient, h, was calculated from the Nusselt number, as earlier described. For the interior boundaries, continuity was applied.

The transient response was then solved from a set of differential equations for the subdomains, the external boundaries, and internal boundaries. The subdomains are governed by

$$\delta_{ts}\rho c_p \frac{\partial T}{\partial t} + \nabla \cdot (-k\nabla T) = Q \ , \tag{5}$$

where δ_{ts} is the time scaling coefficient which is equal to 1 for the transient case, ρ is

the material density, c_p is the heat capacity at constant pressure, T is temperature, t is time, k is the thermal conductivity of the material, and Q is the heat generation. External boundaries were defined as

$$-\mathbf{n} \cdot (-k\nabla T) = h\left(T_{inf} - T\right) + \varepsilon\sigma\left(T_{amb}^4 - T^4\right), \tag{6}$$

where $\mathbf{n}$ is a normal vector, k is the thermal conductivity, T is the temperature, h is the heat transfer coefficient, T_{inf} and T_{amb} are the external ambient temperatures, ε is the surface emissivity, and σ is the Stefan-Boltzmann constant. For the internal boundaries

$$-\mathbf{n_u} \cdot (-k_u\nabla T_u) - \mathbf{n_d} \cdot (-k_d\nabla T_d) = 0\ , \tag{7}$$

where $\mathbf{n}$ is a normal vector, k is the thermal conductivity, and T is temperature. The u and d subscripts refer to the two different subdomains that meet at the internal boundary.

Once initial conditions were set, the geometry was meshed and the problem was evaluated for specified duration. A mesh sensitivity test was performed by refining the mesh until the results did not change between successive simulations.

The above described models were implemented and experimentally validated for radiative heating in glass and plastic microchips coupled to blackbody and monochromatic radiation sources. The glass device is a two-chamber microchip designed for PCR with 500 nL samples, courtesy of James Landers at the University of Virginia. The device is made of borosilicate glass and was fabricated using standard photolithography, wet-etching, and thermal bonding techniques. The plastic device is made of poly (methyl methacrylate) (PMMA) and possesses geometry that approximates that of the glass device. It was fabricated in-house by laser etching the features with a CO_2 laser cutter (VersaLASER, VLS3.50). The dimensions were confirmed with surface profilometry (Dektak 3030) and the enclosed two-layer device was thermally bonded in boiling water [95].

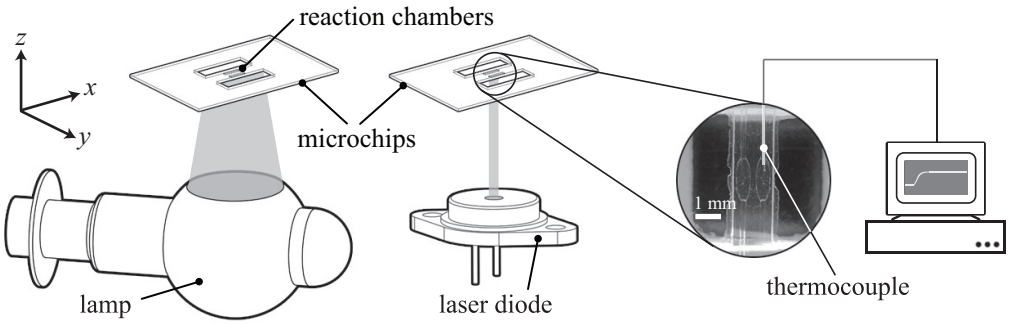

Figure 4: Experimental validation of the heat transfer modeling involved glass and polymer microchips irradiated by a blackbody tungsten-filament lamp (*left*) and a monochromatic infrared laser diode (*center*). Thermocouples inserted to the edge of the reaction chamber (*right*) allowed temperature monitoring. (Not to scale.)

A 50 W tungsten-filament incandescent projector lamp (Eiko, CXL/CXR 8 V 50 W) was used for the blackbody source and a 600 mW 1450 nm laser diode (Hi-Tech Optoelectronics, LMD-1450-600-33) for our monochromatic source, which was selected to match an absorption band of water. The experimental setup is depicted in Figure 4. For the lamp, the total power output was calculated from the electrical power supplied, $P = V \times I$, where V is the voltage and I is the current. Spectral data for determining the absorbed radiation was transcribed from a spectral irradiance curve with a resolution of 25 nm for the range from 300 to 5000 nm. For the laser, the power output is a known function of the supply current and was confirmed with a thermal power meter (Thorlabs, PM10-3). The Gaussian beam profile of the laser diode was sampled with a spectral resolution of 0.5 nm for the short-wavelength infrared range of 1440–1460 nm.

Since the blackbody radiation of the lamp tended to melt the PMMA microchip, this combination was excluded from practical testing, leaving three cases for modeled and experimental validation: 1) lamp heating of water in glass, 2) laser heating of water in glass, and 3) laser heating of water in polymer. Temperatures were kept between the ambient 25°C and 100°C to avoid damaging the PMMA microchip, which has a glass transition temperature of approximately 105°C. Therefore, the radiative

sources were not always operated at full power.

The lumped capacitance and finite element approaches were both implemented for each case. As earlier mentioned, the thin substrates of most microfluidic devices result in negligible thermal gradients across the thickness dimension (z), leaving convection as the primary mode of heat loss. On the other hand, thermal gradients across the width (y) and length (x) of a device may not be sufficiently uniform for the application of the lumped capacitance assumption. As a preliminary assessment of this temperature uniformity, a three-dimensional finite difference model, programmed in computation software Engineering Equation Solver (EES) using Equation 1, calculated the steady state temperatures for a set of nodes representing the heating cases for heating in a glass chip for the lamp and laser.

The transient solutions for each case were first calculated by applying the lumped capacitance approach and were solved using the Runge-Kutta method. The cases were then solved using finite element software COMSOL Multiphysics for simplified geometry of the glass and polymer microchips. The reaction chambers were specified as water volumes and were assigned heat generation values based on the theoretical absorbed radiation. For the case of the lamp heating in a glass microchip, the glass and water were both assigned heat generation values. For the laser heating in glass and polymer chips, only heat generation in the liquid reaction chambers needed to be specified since the absorption of the 1450 nm laser output by the solid substrates is negligible. The finite element solver was run for a time domain of 60 seconds and temperature values were recorded every 0.01 second at ten equally spaced points along the centerline of the reaction chamber. The values at the ten points were then averaged to obtain the mean temperature for the liquid chamber. A mesh sensitivity test revealed no need for refinement of the auto-generated mesh.

For experimental validation, lamp heating was performed at an intermediate power level of 9.3 W as specified in the models. Laser heating in glass was performed at the

full power of 620 mW. For heating in the polymer device, the power was reduced to 300 mW to prevent instabilities resulting from bubble formation at temperature near boiling.

The lamp was powered with a variable power source and focusing was achieved with an ellipsoidal retroreflector, which provided a roughly circular focal spot with a diameter of about 10 mm. The laser was driven with a low-noise current source (Thorlabs, ITC133) and controlled with a 10 Hz PWM signal output from a National Instruments LabView program. The diverging beam was collimated with an aspheric molded glass lens (Thorlabs, A230TM-C), producing a 5 × 2 mm elliptical spot. The ramping of output intensity of each source was measured with a power meter and rise times were considered negligible compared to the transient heating time scales, justifying the use of a step input for the model.

Temperature was measured using a calibrated T-type thermocouple (Physitemp Instruments, T-240C), a thermocouple-to-analog converter (Omega, TAC80B-T), and an analog amplifier. This measurement system will be discussed in greater detail later in Section 3.2.1. Measurements were recorded with LabView and data collection was synchronized with the power supplies for the lamp and laser using a digital output from data acquisition hardware. The thermocouple, which has a response time of 3–4 ms, was inserted into the reaction chamber through an inlet channel, as pictured in Figure 4. The thermocouple tip was positioned with minimal protrusion into the chamber to avoid direct irradiation. With an insertion length of 500 µm and a diameter of 125 µm, the thermocouple occupied only 0.5% of the total chamber volume and had a negligible influence on the thermal mass.

Preliminary tests for the presence of thermal gradients using finite difference analysis to calculate steady state temperatures are shown in Figure 5, which reveals the temperature profiles for lamp and laser heating in glass over the length, width, and thickness of the whole device. While heating with the blackbody source results in

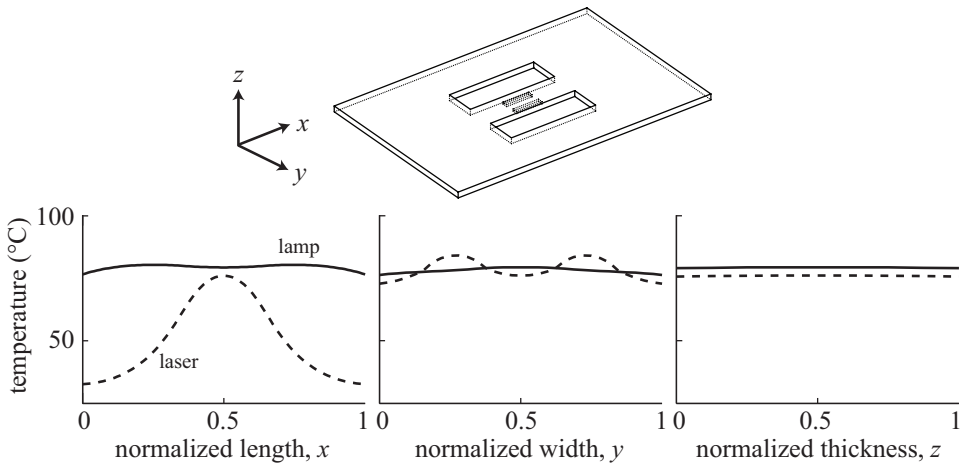

Figure 5: Modeled steady state temperature profiles over normalized dimensions of the water-filled glass microchip for lamp (solid) and laser (dashed) heating. Larger thermal gradients are observed over the length and width for the laser simulation compared to the more uniform profiles for the blackbody lamp heating.

roughly uniform temperatures, the laser heating profiles show more localized heating behavior inconsistent with the prerequisite condition for the effective medium assumption.

The reasons for this behavior are elucidated in Table 2, which summarizes the absorbed radiation values for the lamp and laser heating in the glass microchip. Despite the much greater efficiency of laser heating an aqueous sample, the lamp's higher power output and significant absorption by the glass results in a device of uniform temperature and conductive losses from the reaction chamber are therefore minimized. Conversely, the laser heating is localized in the liquid medium because of the smaller focal spot and the transparency of the microchip substrate to the infrared radiation. This results in greater heat sinking by the substrate, i.e., in-plane conductive heat loss. Despite the categorization of glass as an insulator, its thermal conductivity (1.1 W/m·K) is approximately 5–10× larger than that of a common polymer such as PMMA (0.19 W/m·K) [96].

The optical characteristics for the various heating cases and the results of the uniformity testing suggested the use of finite element methods to capture the localized

Table 2: Percentage of total radiation absorbed by an aqueous sample and glass microchip from a broadband lamp and monochromatic laser source.

Source	**Absorbing medium**	
	Water	*Glass*
Lamp	2%	10%
Laser	70%	1%

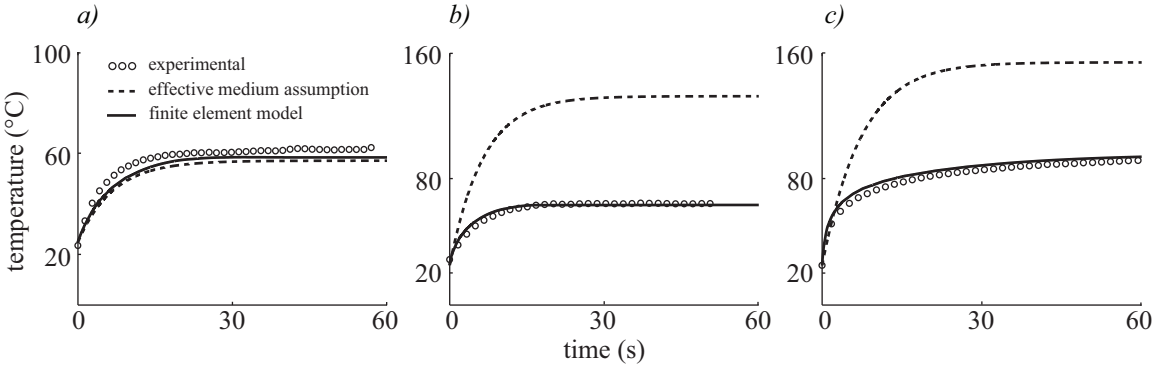

Figure 6: Modeled and experimentally validated transient thermal responses for (a) broadband lamp heating of a glass microchip, (b) infrared laser heating of a glass microchip, and (c) infrared laser heating of a polymer microchip.

heating by our laser. The transient models are compared to experimental data in Figure 6. As a metric for the accuracy of the models when compared to the experimental data, root mean square deviation was calculated as $\sqrt{\frac{1}{n}\sum |T_{exp} - T_{model}|^2}$. For lamp heating of glass, the effective medium model exhibits a deviation of 4.54°C while the finite element model matches slightly better with a deviation of 3.10°C. For laser heating in glass, the effective medium model deviates considerably with a mean difference of 61.17°C, which is to be expected from the temperature uniformity results of Figure 5. The finite element model offers a much better correlation with a deviation of 1.37°C. Similarly, for laser heating in our polymer device, the effective medium model is 59.25°C off while the finite element model deviates by an average of 3.14°C.

With the lamp powered at 9.3 W, which corresponds to the data in Figure 6a, the radiation absorbed by the water is approximately 20 mW while the glass absorbs

110 mW and results in a steady state temperature of 62°C. To compare, the laser operating at its full power of 620 mW imparts 435 mW to the water but the sample only reaches a steady state temperature of 64°C as shown in Figure 6b. Without a heated substrate, the liquid volume suffers from significant conductive losses and the ratio of steady state temperature to power absorbed by the water is much lower than that for lamp heating. The less thermally conductive polymer microchip exhibits reduced conductive heat loss and with the laser power at less than half of that used for glass chip heating, the steady state temperature is a much higher 95°C as shown in Figure 6c.

Small discrepancies between the modeled thermal responses and the experimental data can be attributed to the difficulty in achieving the perfect alignment and spacing inherent in the modeled cases. Additionally, the adjustments made for the theoretical intensity distribution of the sources will be approximations of the actual distributions.

By delineating the radiative contributions of a particular light source to the heating of sample and substrate volumes, the optical modeling provides not only inputs for the heat transfer analysis but also key insights into the efficacy of radiative heating for the variety of microfluidic design permutations. In many ways, heating with a blackbody radiator is viable for a thermally stable substrate because it mimics conventional contact-based heating by directly heating both the sample and substrate while retaining the advantages of the non-contact method. But the limitations of blackbody heating for applications demanding lower substrate cost, higher throughput, and greater spatial control point to the use of a laser with a polymer substrate as the optimal combination.

With a better idea of the type of source and microchip material to be used, the finite element model was implemented for refining the microchip design and addressing concerns regarding optimal chamber geometry and spacing.

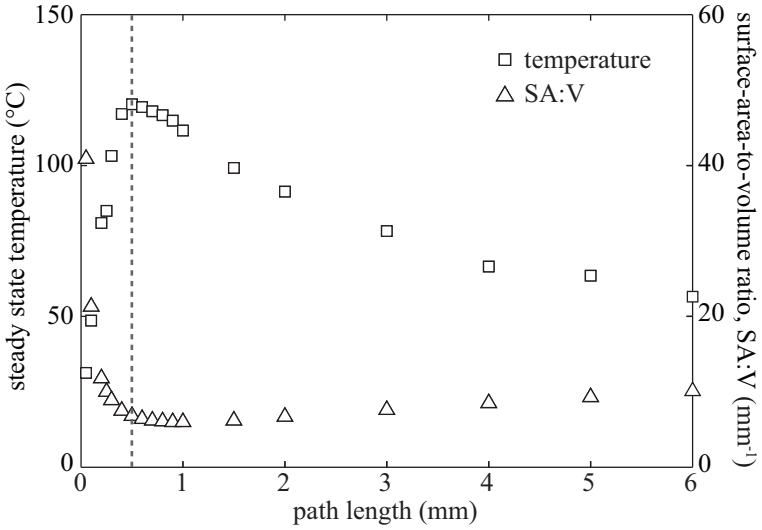

Figure 7: A series of finite element simulations for a variety of reaction chamber geometries correlate steady state temperature with path length (chamber depth) and surface-area-to-volume ratio, indicating the optimal conditions for efficient heating (dashed line).

2.1.2 Reaction chamber geometry

The specific geometry of microfluidic features can play a major role in the performance of the device. For PCR in particular, the geometry can dictate heating efficiency as well as biocompatibility, since the high surface-area-to-volume ratios inherent in miniaturized systems can lead to a form of fouling in which critical biochemical reagents will accumulate on the device surface and adversely affect the reaction. The biocompatibility concerns will be addressed in a later section. Here we will address heating performance as it relates to geometry.

Unlike most traditional microfluidic PCR systems in which the entire microchip is heated and therefore benefit from high SA:V for greater energy transfer from the substrate, our method of localized radiative heating results in different behavior and therefore an unconventional optimal geometry. To determine this geometry, the previously described finite element model was used to simulate radiative heating via an infrared laser for a series of reaction chamber geometries in a polymer microchip. With a fixed reaction chamber volume of 1 µL and a square in-plane cross section,

a set of eighteen path lengths (depth, or z-dimension length, of the chamber) were chosen for a range from 50 µm up to 6 mm. Focal spots for each case were assumed to be perfectly distributed over the particular cross section. For each modeled response, steady state temperature was recorded and plotted against path length, as shown in Figure 7. Additionally, surface-area-to-volume ratio, or SA:V, was calculated for each geometry and plotted alongside the model outputs in Figure 7. The resulting trends indicate a fortunate overlap between optimal geometry for efficient radiative heating, where a maximum steady state temperature was observed at 500 µm path length, and optimal geometry for biocompatibility, where the SA:V is near its minimum and therefore causing minimal reaction inhibition, as explored later.

In addition to finite element modeling, which was the key to understanding the basic behavior of our microchip, we considered factors such as availability of substrate material, limits of fabrication methods, chamber filling behavior, and flexibility of the infrared laser focal spot size to determine a practical geometry. Following the manufacture and testing of several design iterations, a final reaction chamber geometry was selected. A volume of 1 µL was chosen for being sufficiently small for low reagent consumption, while being practical to interface with routine equipment (e.g., pipettes, reagent kits, electrophoretic instrumentation). As depicted in Figures 12b and 17, the chamber was a trapezoidal prism, tapering from a 500 µm × 2.75 mm cross section to a 500 µm × 1.75 mm cross section in the x-y plane, roughly matching the elliptical focal spot shape of our collimated laser. Chamber depth was 750 µm. Fill channels, used for loading the sample and separating the inlet ports from the reaction chamber while minimizing dead volume, were 250 µm wide and 250 µm deep and traced a 3.5 mm U-shaped path from the ports to the chamber. This shape allowed the ports to be in close enough proximity to allow a gasket to surround the ports for pressurization of the microchip, described later in Section 2.3. 700 µm diameter inlet ports allowed for the loading of a sample directly from the tip of a micropipette, obviating

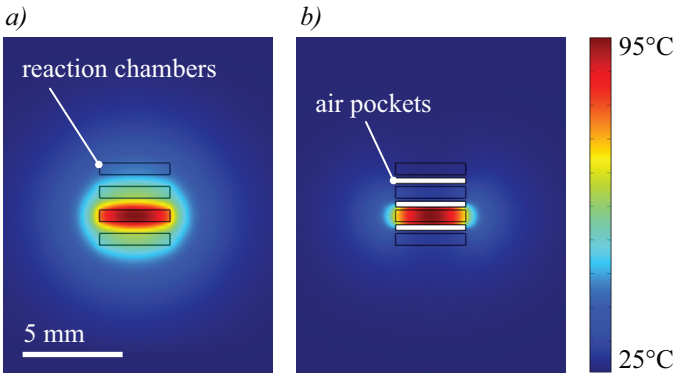

Figure 8: Finite element simulations were used to assess thermal isolation (a) without and (b) with air pockets between the reaction chambers. The sample simulation presented here shows the top view of in-plane (x-y) thermal crosstalk resulting from heating a 1 µL aqueous sample in an array of chambers spaced 1 mm center-to-center. Improved isolation can be observed for the air pocket geometry.

the need for specialized fittings for macro-to-micro, or world-to-chip, interfacing. All microfluidic features were imparted to a 1.5 mm thick substrate.

2.1.3 Reaction chamber spacing

With plans for scaling the throughput of our microfluidic system and with the desire for adjacent reaction chambers to operate at multiple distinct temperatures simultaneously, the limits of thermal isolation needed to be determined. Our finite element model was again applied to study the effect of chamber separation on steady state temperature difference between adjacent chambers. The specific need for thermal isolation relates to the ability to achieve the full range of annealing temperatures, from 48°C to 76°C (28°C range), in adjacent reaction chambers, determined using a primer melting temperature calculator [97]. For a chamber separation of 1 mm, temperature difference between adjacent chambers as a function of the steady state temperature of the heated chamber was modeled and experimentally measured, as plotted in Figure 9a. The model closely matches the experimentally measured thermal behavior and reveals that at the maximum practical annealing temperature of 76°C, the adjacent chamber can only reach temperatures roughly 12°C lower, which

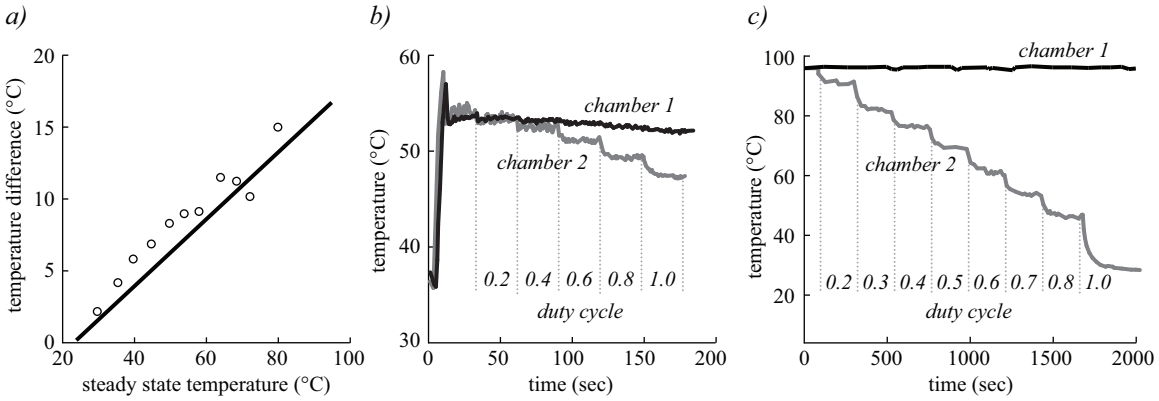

Figure 9: (a) Finite element model (line) and experimental data (circles) showing temperature difference between two 1 µL chambers as a function of the steady state temperature of the heated chamber in a PMMA microchip with 1 mm chamber separation. Temperature of adjacent chambers as shutter duty cycle of one is varied for separations of (b) 1 mm and (c) 40 mm.

would greatly limit the range of possible reactions.

Using our validated model, we computed that a chamber separation of at least 3 mm was required to achieve the full 28°C range of annealing temperatures. A set of two-chamber PMMA microchips were then used to experimentally measure the temperatures in adjacent chambers undergoing infrared laser heating for small (1 mm) and large (40 mm) center-to-center chamber separations (Figure 9b,c). The 1 mm spacing was selected because it represents the practical limit of our fabrication method, since smaller chamber separations do not provide enough surface area for adequate bonding at the dividing barrier between chambers and results in leakage. Additionally, 1 mm spacing allows straightforward delivery of radiation from a single laser source to the two chambers using a collimating lens and custom injection molded lens array with 1 mm interlens spacing [98]. The 40 mm spacing was selected to allow the microchip to span two laser sources, since the lasers and accompanying optics are mounted in side-by-side 30 mm cage systems (Thorlabs). Mechanical shutters were placed in the beam path and controlled with a 10 Hz PWM signal to modulate optical power and generate temperature differences. Radiation to chamber 1 was

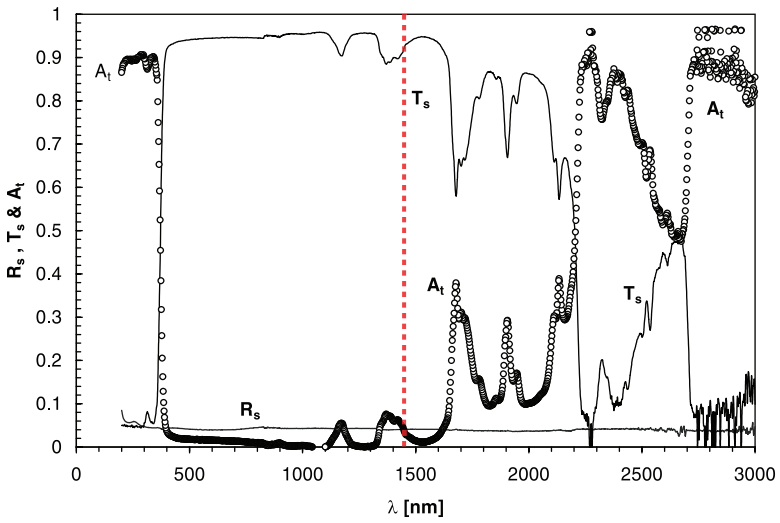

Figure 10: Optical properties of poly (methyl methacrylate) (PMMA) over 200–3000 nm spectral range. At 1450 nm (dashed line), which matches an absorption peak of water and corresponds to the wavelength of the infrared laser used in this work for heating, the polymer is relatively transparent and therefore suitable for use as our microchip substrate. Data reproduced from published work [99].

modulated at a constant duty cycle while the radiation to chamber 2 was modulated in a stepwise pattern. Results indicate that systematic control of chamber temperatures with mechanical shutter modulation is feasible. In addition, 40 mm spacing can be seen to cover the full range of relevant temperatures, as predicted by the model. When implemented experimentally, such large chamber separation is not only beneficial for steady state temperature difference, but also improves transient thermal crosstalk affecting heating and cooling rates.

2.1.4 Material selection

In choosing a substrate material for our microchip, several candidates were considered and tested. One of the most commonly used polymers for microfluidic devices is polydimethylsiloxane (PDMS), an elastomer that is typically used for casting devices from an SU-8 mold made by photolithography. This casting is then bonded to a glass slide for encapsulating the channels and holes are punched for ports into the device. Applications of PDMS devices include microfluidic PCR [100, 101, 102]. While there

are many benefits to such a material, including extensive supporting literature and well-characterized surface chemistry, it did not meet our functional requirements for an affordable, and therefore disposable, device. The relatively high thermal conductivity of the glass base of the device would also prevent adequate heating using out method of direct, localized heating via infrared radiation, as described in the concluding remarks of Section 2.1.1. PDMS device are typically not suitable for use outside of a laboratory, due to the flexibility of the PDMS, the fragility of the glass base, the tendency for PDMS to collect dust and other particles, clouding the otherwise optically clear material. Lastly, the compliance of PDMS would not have been compatible with our use of sample pressurization, a method for the suppression of bubble expansion during heating described in Section 2.3.

We instead focused on rigid polymers compatible with more traditional manufacturing techniques and therefore more affordable and commercially feasible, including polycarbonate (PC), cyclic olefin copolymers (COC), polypropylene (PP), and poly (methyl methacrylate) (PMMA). While any of these options could have yielded a functional device, PMMA was eventually selected for numerous reasons. Its optical properties, shown in Figure 10, indicate high transparency at 1450 nm, which is the wavelength of the infrared laser used in our temperature control system for rapid heating of aqueous samples [99]. This transparency results in a maximum amount of radiation delivered to the sample and avoids heating and subsequent deformation of the substrate surrounding the reaction chamber. Additionally, high transparency to visible light (92%), UV resistance, the quality of milled PMMA features, including minimal burr formation, and the convenience of preparation by laser cutting motivated the selection of this polymer as our microchip substrate [103]. A large sheet of precision cast PMMA (Astra Products, Clarex Precision Thin Sheet, 1.5 mm) could be quickly laser cut into pieces with the microchip's final outer dimensions, ready for micro-milling. Additionally, if desired, labels could be easily laser etched onto the

microchip blanks and was used for identifying particular designs, batches, and dates of fabrication.

2.2 Fabrication

While our finite element modeling provided a guide for designing our microchip with the most suitable material and geometry, the fabrication of this device was a new challenge. A method was needed to provide a microchip compatible with the unique characteristics of infrared laser heating and our requirements for a simple and affordable microfluidic device.

Traditionally, glass and silicon have been the preferred substrates for these microfluidic platforms. Micro-scale features are fabricated using methods borrowed from the semiconductor industry such as wet etching, LIGA, and DRIE, and require expensive, hazardous, and slow processes that severely limit practicality, especially in the early design phases [104]. As a lower cost alternative, polydimethylsiloxane (PDMS) has become a ubiquitous polymer for devices made by soft lithography, as pioneered by Dr. George M. Whitesides [105]. Still, as described in Section 2.1.4, this approach requires tedious mold fabrication and yields devices insufficiently robust for applications outside of a laboratory. As the field of microfluidics matures, shifting towards affordable, disposable, and commercially viable platforms, conventional materials and the accompanying techniques are being replaced [65]. Instead, rigid polymers such as PMMA, polycarbonate, and cyclic olefin copolymers (COC) are preferred and techniques such as thermoforming, injection molding, laser etching, and micro-milling have emerged as effective solutions.

A summary of the fabrication methods explored over the course of this project is presented in Figure 11. Before developing the heat transfer model described in Section 2.1.1, glass microchips with 550 nL reaction chambers (Figure 11a), fabricated by our collaborators at the University of Virginia [39, 106], were used for early tests

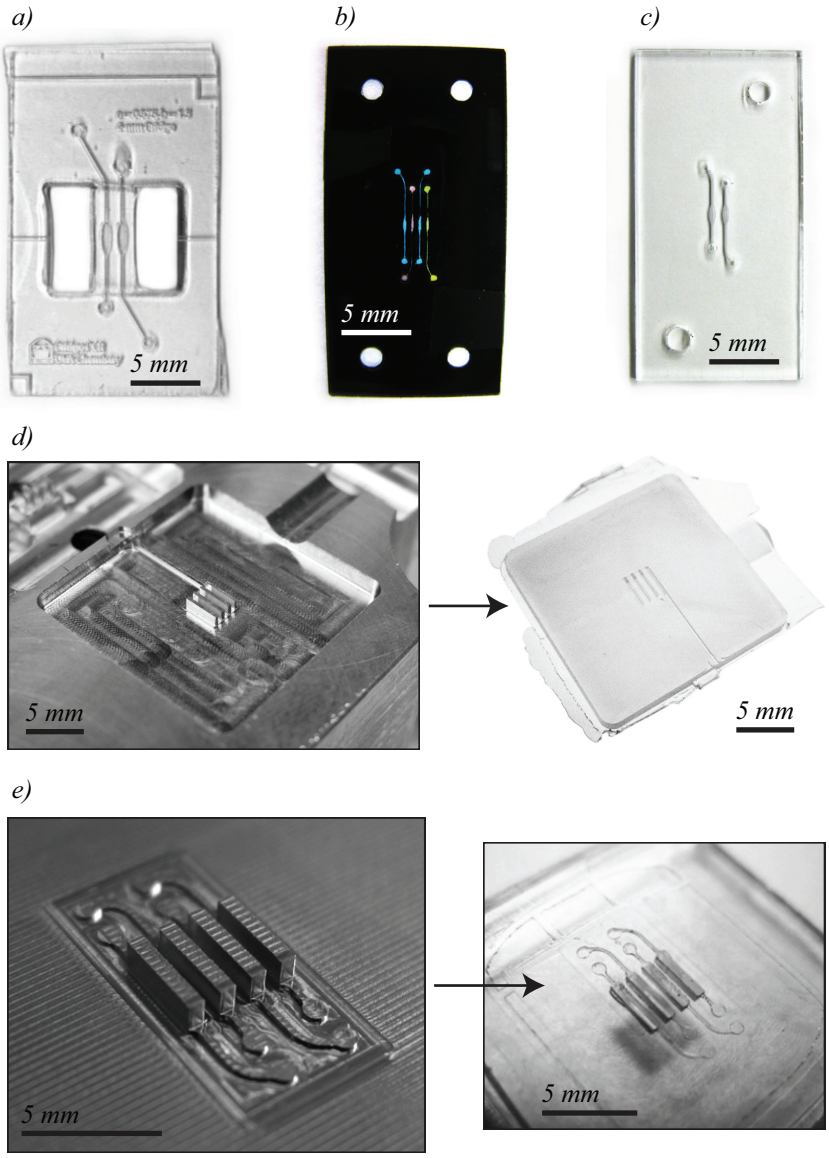

Figure 11: Several techniques were attempted for the fabrication of our PCR microchip. (a) Glass devices were fabricated by collaborators using chemical etching and thermal bonding. (b) "Toner chips" were laminated from PET transparency films printed with a multi-chamber design. (c) PMMA devices were laser etched with side-by-side reaction chambers and bonded in boiling water. (d) An aluminum mold was CNC machined (*left*) and used for injection molding of COC and PP devices (*right*). Flashing and a trimmed portion of the runner can be seen at the perimeter of the injection molded part. (e) Hot embossing was performed using a stainless steel mold (*left*) that was heated above the glass transition temperature of the substrate and pressed into the substrate to produce the microfluidic features (*right*).

of our laser-mediated thermocycler. After discovering the need for a more insulating substrate, a variety of techniques were used to produce a polymer microchip. An early effort made use of polyethylene terephthalate (PET) transparency films with selectively printed toner regions, which defined the microfluidic geometry and provided an adhesion interface. Films were laminated together to form a "toner chip" [107, 108, 109], which can be seen in Figure 11b. Despite their remarkable simplicity, these devices lacked the desired durability, offered limited choices of feature depths and three-dimensional geometries, and presented too many questions regarding biochemical compatibility with PCR. Experiments with laser etching, also known as laser ablation or laser micromachining [110], shown in Figure 11c, proved to be fast and affordable but incompatible with many materials and presented difficulties achieving accurate depths and smooth surface finishes. Fabrication by injection molding [111] is ideal for high-volume production of low-cost devices but suffers from numerous drawbacks. Our experiments with this approach involved CNC machining an aluminum mold insert for the production of a four-chamber design using both cyclic olefin copolymer (COC) and polypropylene resins. The mold and resulting device are pictured in Figure 11d. In addition to challenges of difficult de-molding and excessive warpage, the greatest hurdle was the time and cost investment for fabricating a mold for each design iteration, a process not amenable to the prototyping process. A similar method known as hot embossing [103, 112, 113, 114, 115, 116] was also attempted (Figure 11e). A 303 stainless steel mold was first micro-milled with an inverse of the desired features. The mold and substrate were then loaded onto the lower platen of a hot press and heated to just above the glass transition temperature of the substrate polymer. Once heated, the substrate was positioned over the mold and pressed at roughly 500 psi. Despite testing this method with a variety of materials, including polycarbonate and three grades of cyclic olefin copolymer (Zeon Chemicals), the aspect ratios of the reaction chamber geometry proved too high to achieve

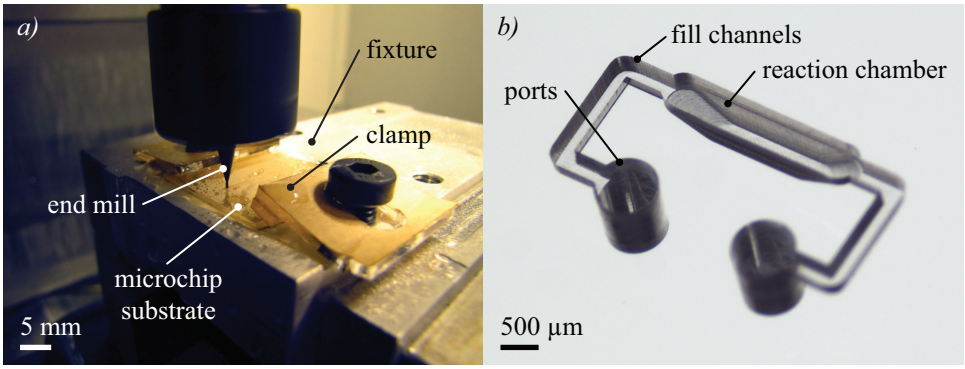

Figure 12: Microfluidic device features are micro-milled on a 3-axis CNC vertical milling center using miniature tooling operating at spindle speeds up to 30,000 rpm. (a) An aluminum fixture positions and retains the microchip substrate during the milling process. (b) A close-up of microfluidic features (ports, fill channels, and 1 µL reaction chamber) milled into 1.5 mm thick PMMA and cleaned with isopropanol, deionized water, and compressed N_2.

adequate filling of the mold. Damage to the mold, specifically plastic deformation of the reaction chamber features, was also observed after repeated trials.

Direct micro-milling of microfluidic features, although uncommon, had been demonstrated for microfluidic applications [117] and was found to be the most viable method for fast turnaround (e.g., 5 min per device), wide-ranging dimensions, consistency, and low cost.

2.2.1 Micro-milling

Fabrication of the microchip by micro-milling began with the conversion of the device design to g-code, which was interpreted by a CNC machine to execute the desired operations. Although this is typically performed with CAD-CAM software, code was manually written for this application for complete control of all tool paths. The code was loaded onto a 3-axis CNC vertical milling center (Haas, OM-1A) capable of accurate positioning within 10 µm, repeatability of 6 µm, spindle speeds up to 30,000 rpm, and a 20-station automatic tool changer.

A custom aluminum fixture (Figure 12a) was CNC milled and used to align and rigidly hold the substrate during fabrication, since small part deflections can easily

damage the fragile tooling. A protrusion was milled into the rear face of the fixture to allow for highly repeatable positioning against the jaws of the precision vise of the milling machine. A corner relief was pocketed into the top of the fixture to allow repeatable positioning of the microchip. These features enabled rapid setup without the need to zero the x and y-axes prior to milling. Although the fixture provided highly repeatable positioning of the substrate, this accuracy was not critical since internal alignment features were included in the microchip design, loosening the tolerance on the outer dimensions of the device and diminishing the importance of careful filtering of the substrate. Clamps were laser cut from 3 mm PMMA and hand-tightened with m6 screws in a third-class lever arrangement, adequately retaining the substrate during milling without marring the surface of the workpiece. Fixtures for milling multiple microchips (e.g., 12 parts/run) were made for quickly generating large batches of devices within single CNC runs. To maximize the density of the substrate arrangement in the fixture, which in turn minimizes error due to deviations in height of mill table and spindle over the fixture area, a clamping alternative was developed. A sheet of 3 mm PMMA was laser cut with pockets featuring integrated flexure springs, which allowed the operator to quickly load and unload blank microchip substrates without fasteners and provided adequate retention during the milling process. After milling, a wooden stir stick was used to gentry pry up the side of the chick, quickly ejecting the devices without damaging the PMMA surfaces. This integrated spring-based alignment and retention method was described in our early work developing the first generation of open-loop, laser-mediated, microfluidic PCR instrumentation [118].

Six different tools were used to produce the microchip features shown in Figures 12b and 17. Three miniature 2-flute carbide square end mills (Harvey Tool) with diameters of 250 µm, 500 µm, and 3.175 mm were used for milling fill channels, reaction chambers, clearance holes for retaining screws, respectively. Two carbide

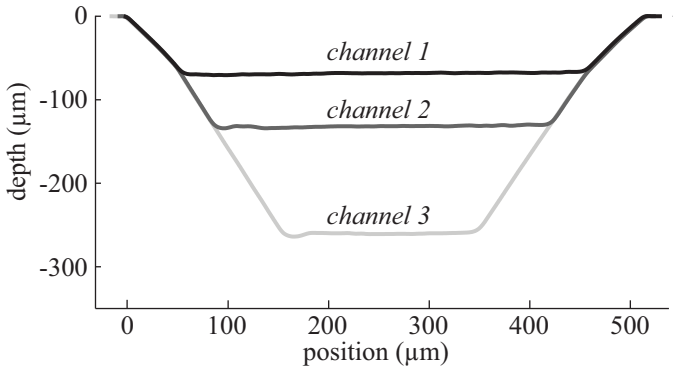

Figure 13: Surface profilometry was used record surface topology of three micro-milled channels of depths 63.5, 127, and 254 µm. Average roughness of 340 nm was measured.

drill bits (Drill Bit City) with diameters of 700 µm and 1.55 mm were used to drill ports and alignment holes, respectively. A 0.0630 inch straight flute reamer was used to bring the alignment holes to their final diameter for sliding over 1/16 inch dowel pins. Prior to milling, each tool was zeroed to the top surface of the substrate. This was accomplished by moving the tool in 0.0001 inch (2.54 µm) increments in the z-axis towards the aluminum fixture and using a multimeter to detect electrical continuity between the tip of the tool, which was rotating at 1,000 rpm, and the base of the fixture [119]. The tool was then offset by the thickness of the substrate, which was precisely measured using a dial probe indicator. Flood coolant was used during the milling process to clear chips and cool the tool-substrate interface to avoid melting. To clean the milled devices and prepare them for bonding, they were sonicated in deionized water for 30 minutes, rinsed with with isopropanol and deionized water, then dried with compressed N_2.

As can be seen in Figure 12b, the micro-milling process leaves behind tool marks, imparting a texture to the inner surface area of the device. In order to quantify this surface finish, which can play a role in trapping unwanted bubbles as examined later in this chapter, a surface profilometer (Taylor Hobson, Talysurf Surface Profilometer) was used to measure surface roughness. Three channels with depths of 0.0025, 0.0050,

and 0.0100 inch (63.5, 127, and 254 µm) were milled into a sample of PMMA using a 250 µm diameter square end mill operating at 30,000 rpm and tilt-corrected profile data was collected along the bottom of the channels (Figure 13). Roughness average values, calculated as the average of the absolute values of the profile height deviations from the mean depth, ranged from 230 to 440 nm, increasing monotonically with channel depth, with an average of 340 nm, which is an order of magnitude lower than reported values for micro-milled devices [65].

Micro-milling provided the ideal means for rapidly prototyping devices with unique geometries well suited for our purposes. Figure 14 shows a variety of microchip designs featuring linear and radial arrays of reaction chambers and three-dimensional geometries, including spherical and rectangular prismatic chambers made possible by different tooling options and milling operations. These multi-chamber designs were useful for early higher-throughput testing of the biochemical compatibility of our microchips with PCR prior to implementing them with out laser-mediated thermocycler.

Still, there are a number of drawbacks to this approach. In addition to the previously mentioned issue of tool marks creating sites for air bubble entrainment, micro-milling is not economical for high volume production. Another downside is that it cannot be easily accomplished with a conventional milling machine due to the need for relatively high spindle speeds required when working with sub-millimeter tooling; the common maximum spindle speed is 3,000 rpm. A spindle speeder, also known as a high-speed spindle attachment, is an option for achieving higher spindle speeds with a conventional milling machine. Still, even with access to a machine with high spindle speeds, the smallest features successfully micro-milled in the course of this research were 125 µm wide channels used by a collaborator for on-chip DNA electrophoresis. Dimensions below 100 µm could be exceedingly challenging due to the limits of spindle speed, machine accuracy, and available tooling.

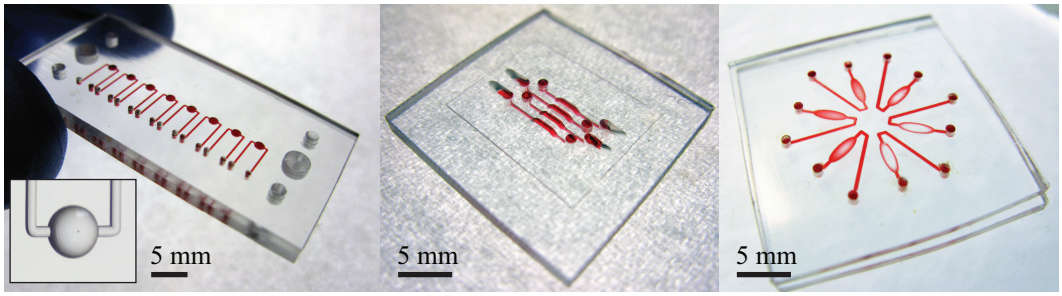

Figure 14: Examples of PMMA micro-milled devices. (a,b) Linear and (c) radial arrays were fabricated with various reaction chamber geometries, including (a) spherical, (b) trapezoidal, and (c) elliptical with traditional uniform depth.

2.2.2 Thermal bonding

The micro-milled features of the microchip must be fully enclosed before the device can be functional. The resulting two-layer microchip must be thermally and mechanically robust enough to withstand temperatures up to 95°C without deformation and endure repeated use without suffering delamination or other damage. An early method for enclosing the channels / chamber made use of adhesive-backed 50 µm thick heat-resistant polypropylene film typically used for sealing 96 well plates (Excel Scientific, ThermalSeal). This was adequate for preliminary testing of the device in a water bath PCR system but the adhesive did not possess the bond strength required for pressurizing the sample. Next, a 200 µm thick PMMA film was thermally bonded as the enclosing layer. As with the adhesive film, the PMMA film aided in efficient heating by providing thermal insulation and efficient cooling by allowing free convection. Despite these advantages and its ability to remain bonded, the PMMA film suffered catastrophic deformation when pressurized at the higher temperature encountered for PCR (Figure 16). The best choice of enclosing layer was the same 1.5 mm thickness PMMA used for the micro-milled substrate.

Early experiments with thermal bonding made use of an aluminum clamping fixture immersed in boiling water [95]. This technique was initially viable but, as with

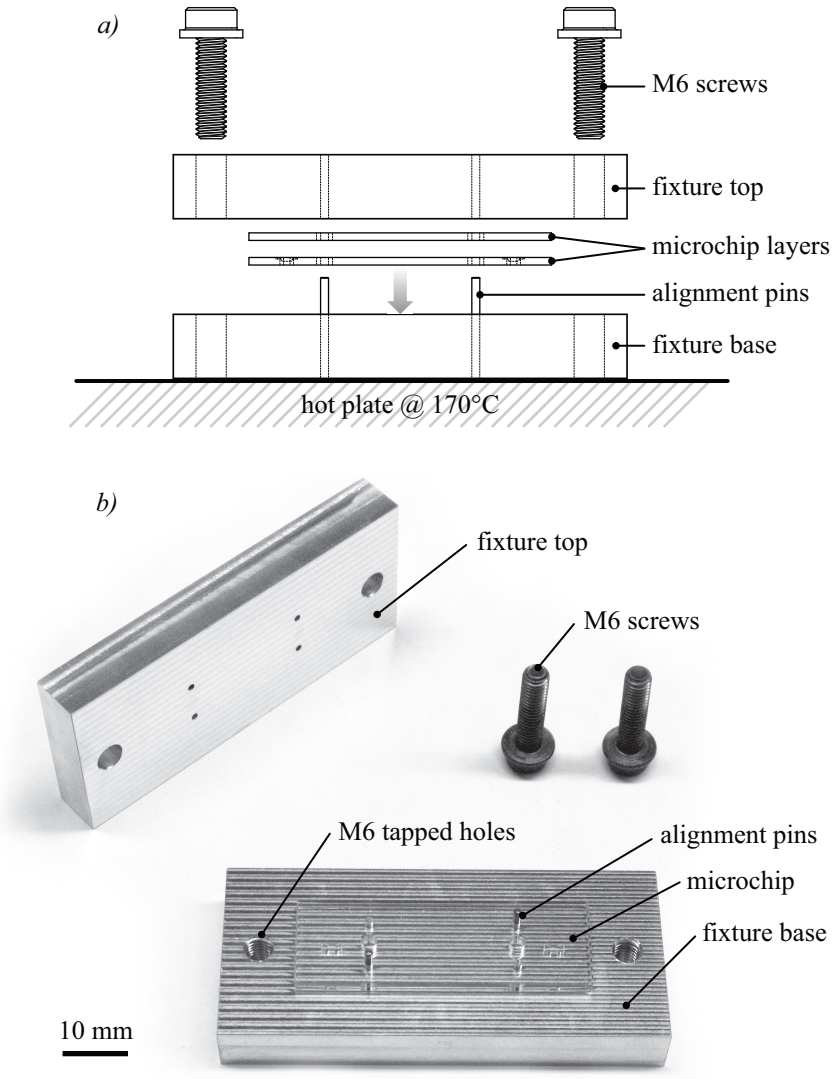

Figure 15: Microchips were thermally bonded using an aluminum bonding fixture featuring alignment holes designed to align the microchip layers using 1/16 inch dowel pins. Pressure is applied via two M6 screws, each precisely tightened with a torque screwdriver for high repeatability, after which the fixture is heated to 170°C for 30 min then cooled to room temperature. (a) Exploded view of how the fixture microchip layers were assembled for bonding. (b) Unbonded microchip layers mounted on the fixture base.

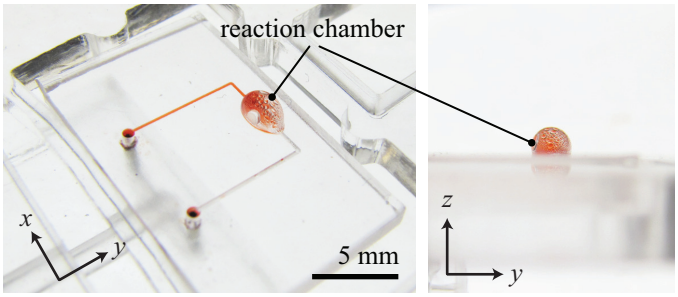

Figure 16: Enclosing the microchip features by thermal bonding of a 200 µm PMMA film was effective until the introduction of sample pressurization, resulting in the expansion and subsequent destruction of the reaction chambers when heated above 90°C. Red food coloring was used for visualizing the aqueous sample.

the adhesive film approach, bond strength was not high enough to withstand pressurization of the sample, a measure necessary for bubble suppression as described later in Section 2.3. An improved thermal bonding method was developed and empirically optimized to provide high bond strength without deforming the microfluidic features. Although a variety of thermal bonding fixtures were fabricated and used with equal success, including one made of tellurium copper and another with glass used at the fixture-microchip interface for maximum optical clarity, the final bonding fixture was machined from 1/2 inch thick 6061 aluminum with special care taken to ensure a smooth surface finish, which was accomplished by CNC milling the inner faces of the fixture and using a face milling routine with a very small step-over distance (e.g., 10% of the end mill diameter), yielding a near mirror finish. The fixture, pictured in Figure 15, features a set of holes reamed to 0.0630 inches in both sides, providing a sliding fit for 1/16 inch diameter dowel pins, which correspond to an identical set of holes that were drilled in both layers of the microchip. These alignment features serve the dual purpose of accurately positioning the microchip layers in the bonding fixture and positioning the bonded microchip on the the infrared laser system. A set of M6 tapped holes in the fixture base and corresponding clearance holes in the fixture top accommodate M6 flanged socket head cap screws for applying bonding pressure.

The bonding process was performed by first loading recently cleaned and dried

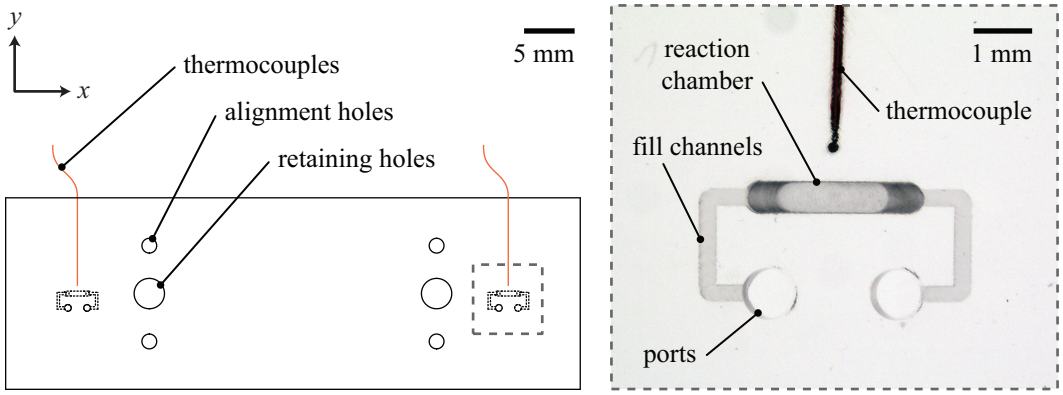

Figure 17: The two-chamber microchip design is comprised of two 20 × 60 ×1.5 mm PMMA layers, one layer featuring a set of micro-milled ports, fill channels, reaction chambers, alignment holes, and retaining holes, and the other layer featuring only the alignment and retaining holes. Two thermocouples are positioned in close proximity to the two 40 mm spaced reaction chambers and embedded during the thermal bonding process to produce a finished device.

microchip layers onto the base of the fixture by sliding them over the alignment pins. If thermocouples were to be embedded in the device, the microchip layers were slightly spaced apart and the thermocouples were carefully positioned using a 10× loupe or magnifier visor to align the tip to approximately 500 µm from the side of the reaction chamber in the y-dimension and centered with the chamber in the x-dimension. This spacing was found to be close enough to the chamber to capture temperature dynamics and far enough to avoid incomplete bonding between the thermocouple tip and chamber, which can cause leakage during pressurization. The top of the fixture was then mounted over the same alignment pins and the M6 screws were tightened to 0.340 ± 0.014 N·m using a vertical torque gauge screwdriver (Seekonk, S0-48) for repeatable bonding pressure. The fixture was placed on a large hot plate, heated to 170°C for 30 min, then allowed to cool by natural convection to room temperature.

Since there were concerns regarding thermal deformation of the microchip features during bonding, such as partial chamber collapse due to thermal expansion and in-plane drift, bonded microchips were examined via microscopy to verify repeatable,

undeformed features. An alignment fixture was mounted to the stage of an inverted microscope and used to image ten consecutively bonded microchips. Adobe Photoshop was used to overlap images, adjust transparency, and note pixel differences. These pixel values were converted to length values based on sensor specifications and averaged. The maximum in-plane position variation of the microchip features was calculated to be 15 µm.

Many microchip versions were fabricated with this micro-milling and thermal bonding process. The final two-chamber design is shown in Figure 17. Each layer began as a laser cut PMMA blank with dimensions of 20 × 60 ×1.5 mm. One layer was micro-milled with two reaction chambers spaced 40 mm center-to-center, each with the accompanying fill channels and ports, along with four 0.0630 inch alignment holes (N.B. only two holes are used in practice for alignment) and 3.175 mm clearance holes for M3 retaining screws. The other layer featured only the alignment and retaining holes. Two thermocouples were embedded in the microchip for monitoring the temperature of each reaction chamber. Thermocouples must be spaced away from the chamber because a thermocouple tip located inside the reaction chamber would adversely affect PCR due to reagents interacting with the metal surface thereby resulting in either reduced efficiency or completely inhibition of the reaction [120]. An additional problem with this configuration would is direct heating of the thermocouple tip by the infrared laser, biasing the measurement and preventing accurate temperature control.

Due to the low cost of materials, short fabrication time, and risks of cross contamination, our microchip was designed for single-use, after which the device is mildly heated, thermocouples are removed for future use, ports are sealed with an adhesive film, and the device is discarded as biohazardous waste. Still, a series of experiments was performed to determine reusability in which a single microchip was used for ten

serial PCR runs, with a cleaning step carried out by thoroughly flushing the reaction chamber with isopropanol and deionized water and drying with compressed N_2 between each run. Although measurements of the temperature profile demonstrated that the thermal performance, including heating and cooling rates, was consistent, end-point detection indicated that PCR yield monotonically decreases between the first and fourth run and fails to produce a detectable amplicon concentration after the fourth trial.

2.3 Bubble suppression

A commonly encountered obstacle in the field of microfluidics is the presence of bubbles in a microfluidic device, typically stemming from the dominance of surface tension at the microscale. Bubbles are often introduced at the world-to-chip interface or are the result of air trapped by surface imperfections [121, 122]. When performing PCR, even small air pockets can expand during the heating process, as governed by Charles' Law describing the isobaric expansion of gasses, $V_f = V_i \frac{T_f}{T_i}$ where V_i and V_f are initial and finial bubble volumes, respectively, and T_i and T_f are initial and final temperatures. For example, heating from 25°C to 95°C results in roughly 23% expansion of bubble volume. When this occurs over multiple small air pockets, they expand and coalesce to create large bubbles that can displace or completely purge the sample from the microchip.

Even with the seemingly low surface roughness values measured for our micro-milled features, bubble formation was a persistent issue during early testing of the microchip. Published methods include physical bubble traps integrated into the device [122, 123], ultrasonic micro-degassing [124], and selectively permeable membranes [125]. Degassing of the reaction chambers of a filled microchip was attempted using a vacuum chamber to remove bubbles but surface tension in the microenvironment prevented the extraction of the problematic air pockets. The addition of surfactants

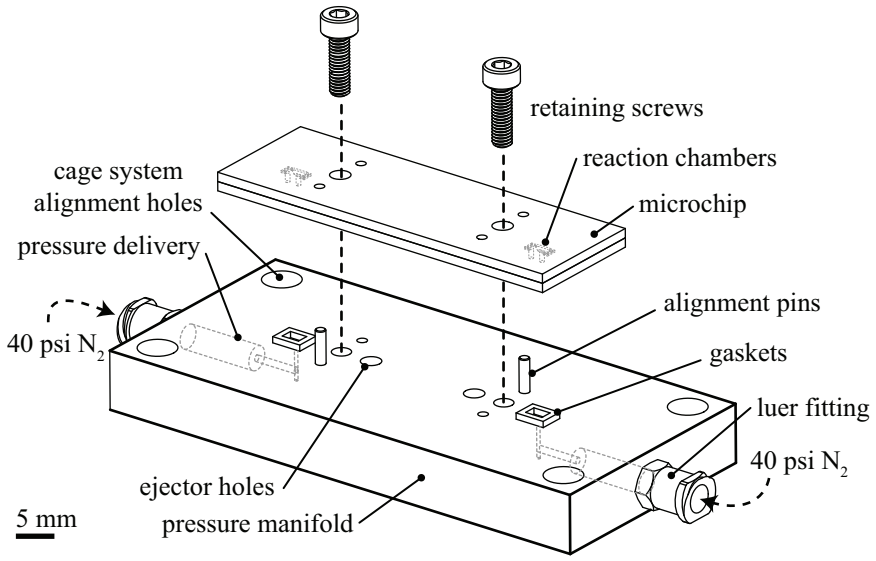

Figure 18: An acrylic pressure manifold was fabricated for delivering 40 psi to the ports of the microchip, pressurizing the aqueous samples and in turn suppressing the expansion of problematic air bubbles.

(e.g., Tween 20, PEG derivatives) for lowering the surface tension at the sample-air interface during loading was also tested but did not prevent the formation of air pockets. Several efforts were made to modify the surface of the reaction chamber prior to bonding the device including parylene coating, flame polishing using a custom nozzle on a butane torch, chemical polishing by masking the bonding interface and exposing the micro-milled features to heated dichloromethane vapors, and polishing using a defocused CO_2 laser. Despite promising results from these efforts based on visual inspection, none of them were successful in preventing bubble formation and expansion.

Instead of preventing the initial entrainment of air bubbles, we shifted focus and decided to simply prevent them from ever expanding. This was accomplished by applying external pressure to the sample volume. Initial pressurization tests were conducted using an inverted microscope (Nikon, TE2000) equipped with a $4\times/0.2$ NA objective (Nikon) and a custom microchip adapter allowing us to observe and image bubble activity in the reaction chamber while heating from above the device

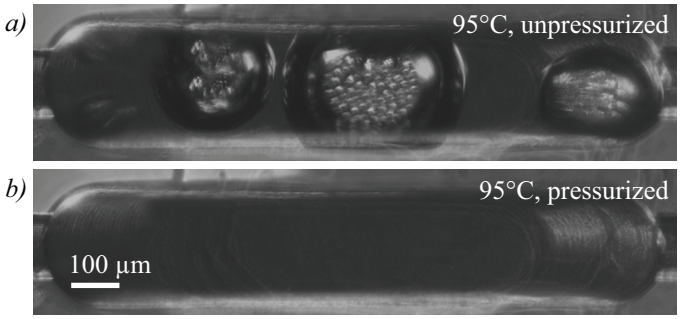

Figure 19: Bubble suppression in our 1 µL reaction chambers was observed on an inverted microscope by heating to 95°C and imaging the microchip (a) before and (b) after introducing 40 psi N_2 to the ports of the microchip.

and delivering pressure to the microchip. After the sample was heated above 80°C, the threshold at which bubbles began to become apparent, a pressure regulator was used to slowly increase pressurization until the bubbles were no longer visible, as shown in Figure 19. This complete suppression was observed at a minimum pressure of 40 psi. As reported in previous work [87], delivering 40 psi to the ports of the device completely suppressed bubble expansion, allowing thermocycling to progress unhindered. For use with the two-chamber microchip presented here, a pressure manifold was machined from 0.375 inch acrylic featuring L-shaped internal pathways that delivered 40 psi pure N_2 from a 49 L storage tank to threaded luer fittings at each end of the manifold to the ports of the microchip. A 1 mm thick, rectangular, laser cut silicon gasket provided an airtight seal between the microchip and pressure manifold (Figure 18). A set of 1/16 inch dowel pins align the microchip to the manifold, which features four 6 mm holes to align the manifold-microchip assembly to the 30 mm cage system housing the infrared laser components. Two M3 retaining screws secure the microchip to the manifold and allow proper compression of the silicon gaskets. A pair of 0.126 inch holes serve as ejector holes, allowing the manifold to be pressed onto an aluminum block with 1/8 inch dowel pins which separates the microchip from the pressure manifold for easy removal.

2.4 Surface chemistry

One of the most vexing problems encountered when performing PCR at low reaction volumes is surface chemistry-related inhibition. The higher surface-area-to-volume ratio (SA:V), which is the surface area surrounding the reaction divided by the its volume and is expressed here with units of mm^{-1}, that results from the miniaturization process magnifies the problem of reaction inhibition due to increased probability of adverse interactions between reagents and inner surfaces of the microfluidic architecture. This problem was acknowledged in early efforts at miniaturization of PCR [56, 126] and has been explored in the search for the most suitable substrates and effective passivation methods [63, 127, 128, 129, 130, 68, 131, 132, 133, 134]. It has been shown that the most deleterious factor is adsorption of the polymerase enzyme to the surfaces in contact with the reaction mixture [132, 127], as well as adsorption of intercalating dyes, such as Sybr Green, in the case of real-time PCR applications [135]. Although some substrates appear to be more inert for PCR purposes, the effects of adsorption appear to occur for most substrates and becomes more pronounced with increasing SA:V. A commonly used reaction volume of 50 µL in a standard polypropylene PCR tube exhibits a SA:V of about 1.3 while microfluidic devices are reported with SA:V more than an order of magnitude higher [54]. Despite the recognition of SA:V as a concern for the viability of microfluidic PCR systems, its effects had not been modeled or quantified systematically.

Adsorption of the polymerase enzyme to microscale surfaces has been reported qualitatively [128] to be a contributing factor in yield reduction at small volumes, and this problem is compounded by the inherent increase in SA:V in microfluidic devices. The specific adsorption of polymerase is commonly explained as a result of hydrophobic interaction between the enzyme and substrate, where hydrophobic substrates will be more likely to adsorb more enzyme [136, 129]. Recent studies by

Sweryda-Krawiec et al. (2004) and Prakash et al. (2008) have demonstrated adsorption by both hydrophobic and hydrophilic substrates, discounting wettability as a standalone mechanism. There is a multitude of possible interactions, including hydrophobicity/hydrophilicity [137, 138, 139], surface free-energy [140], electrostatic attraction/repulsion [141, 142, 143], thermodynamics [144, 145], unique interfacial tension between the protein and adsorbing surface [146], and relationship between protein penetration and steric hindrance from the structure of the protein and adsorbing substrate [147, 148, 149]. It is worth noting that many authors have suggested that the adsorption mechanisms themselves may not be fully understood [144, 147, 131].

Several methods have been used to counteract the inhibition of PCR by adsorption, which is depicted in Figure 20. Dynamic passivation agents (additives to the PCR mixture) such as bovine serum albumen (BSA), polyethylene glycol (PEG), and polyvinylpyrrolidone (PVP) compete with the PCR reagents for adsorption sites on the surfaces of the reaction chamber [63, 127, 129, 130, 68, 131, 132, 133, 134]. Further, there is an emerging trend toward droplet microfluidics, in which discrete aqueous volumes (e.g., 100 pL) are encapsulated in oil [150, 70, 151] with excellent amplification results. These droplet systems require pneumatic droplet generators and flow cytometers. Ideally, effects and advantages of passivation techniques such as BSA and oil encapsulation could be quantified and/or combined with the simplicity of practical, hand-pipetted volumes (e.g., 1–10 µL) in a disposable polymer chip.

In an effort to further the understanding of this problem and identify a solution applicable to our microfluidic device, we experimentally characterized and theoretically modeled the adverse effects of high SA:V on PCR yield and the efficacy of common methods of passivation to counteract surface-related inhibition. These results were applied to the development of a protocol capable of performing PCR at a 1 µL reaction volume with diagnostically relevant sensitivity and specificity, comparable to conventional PCR in a tube. For this proof-of-concept for our microchip, we used

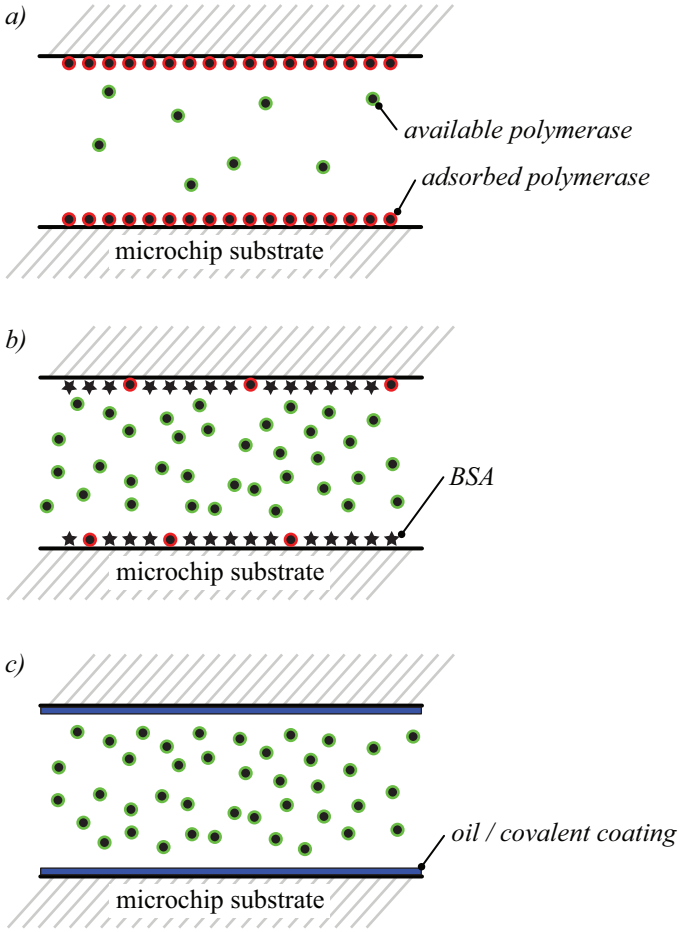

Figure 20: Adsorption of polymerase to the surfaces of microfluidic devices in contact with a PCR sample is a known contributor to reaction inhibition. The extent of inhibition depends on the properties of the substrate material. (a) An untreated hydrophobic surface will readily adsorb polar molecules such as DNA and especially polymerase, leaving a limited quantity of available polymerase. (b) Dynamic passivation makes use of molecules such as BSA, PEG, and PVP to coat the surfaces of the device, outcompeting the important reagents and minimizing inhibition. (c) Static passivation methods make use of techniques such as covalent surface modification or oil encapsulation to isolate the sample from the substrate and contain the sample within a less inhibitory environment.

consensus degenerate primers for pan herpes virus PCR and the Epstein-Barr virus (EBV) as a template. EBV is a double stranded DNA virus belonging to the family *Herpesviridae*. Nearly every human is infected with EBV before adulthood. Infection early in childhood is usually asymptomatic, while delayed primary infection is typically manifest by the signs and symptoms of mononucleosis [152]. After infection, the viral genome is retained for life at low concentration, and presents as illness in higher concentration when the immune system is compromised [153, 154]. Therefore, a threshold concentration between low and high viral loads is necessary for diagnostic purposes. There is no consistently published threshold, but one study [155] observed a median high viral load of 32,250 (range: 10,150–47,450) copies/mL and a low viral load of 7,400 copies/mL. Thus, we set a threshold for this work of 3×10^5 copies/mL.

Any viable microfluidic PCR approach must achieve sensitivity and specificity comparable to conventional PCR tubes. As discussed for the EBV virus, sensitivity to a threshold viral load must be defined. Ideal specificity would involve only amplification of the target region for which that particular PCR assay was intended, without amplifying non-specific products. Here, discernment of the viral target fragments in an electropherogram in the presence of a noisy human DNA background served as a qualitative specificity assessment and comparison to conventional techniques.

2.4.1 Characterization of PCR inhibition

Low volumes (e.g., < 5 µL) can be problematic even with conventional, injection-molded, polypropylene PCR tubes [49]. The lower limits of volume were examined using conventional tubes by testing volumes of 5, 3, 2, and 1 µL (SA:V=3.1, 3.8, 4.5, and 5.7, respectively) with serial dilutions of EBV template. One set followed a conventional recipe (Figure 21a) and the other used 0.2 µg/µL BSA for dynamic passivation (Figure 21b). Success rate decreased with decreasing volume and benefited from the addition of BSA. None of the 1 µL reactions were successfully amplified.

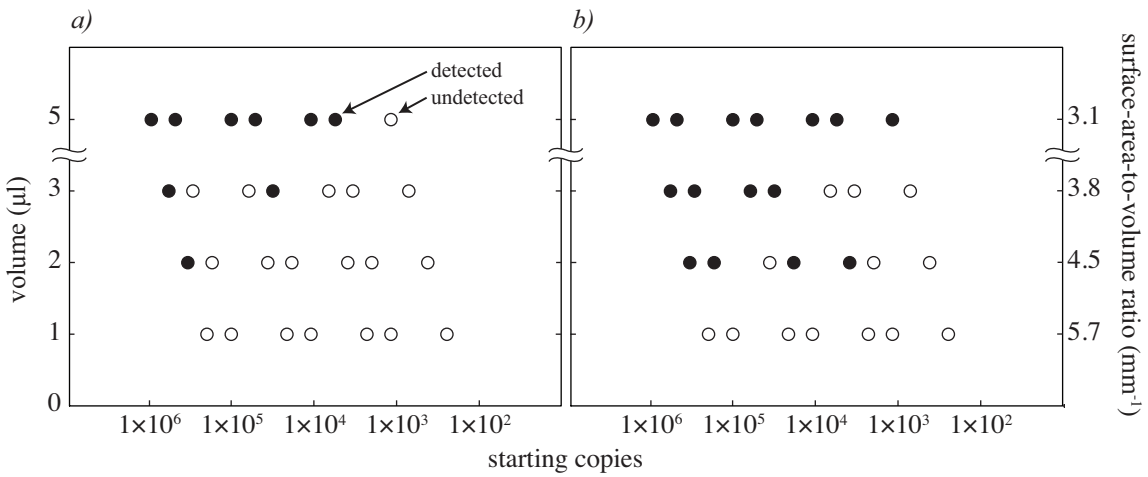

Figure 21: Epstein Barr virus detection results in conventional PCR tubes (a) without BSA and (b) with BSA for a range of starting copies. Reaction parameters: conventional PCR tubes, EBV template, BSA concentration 0.2 µg/µL, 40 cycles.

In addition to the challenges of preventing evaporation and recovering the sample presented by the use of low volumes in conventional tubes, we suspected surface-related inhibition might also play a greater role with decreasing volume. Results for the BSA passivated samples substantiate this claim, with improved success rate, notably for starting copies of 10^4–10^6 at volumes of 2–3 µL (SA:V=3.8–4.5). BSA also improves success with constant SA:V at limiting starting copies: we measured a limit of detection of approximately 5,000 starting copies without BSA, but 1,000 starting copies with BSA. With starting copies ranging from 5×10^2–5×10^5, none of the 1 µL reactions led to successful amplification, underscoring the importance of microfluidic devices for amplification of these volumes.

With confirmation of the limits of conventional tube PCR at low volumes, we performed a systematic study of the effects of material and geometry, specifically SA:V, using a set of reactions in volumes of 50 µL in conventional PCR tubes. Standard control reactions were compared to a set of reactions in which higher SA:V environments were created by adding segments of polymer capillaries (Paradigm Optics) to the tube as shown on the left in Figure 22. The high SA:V environments

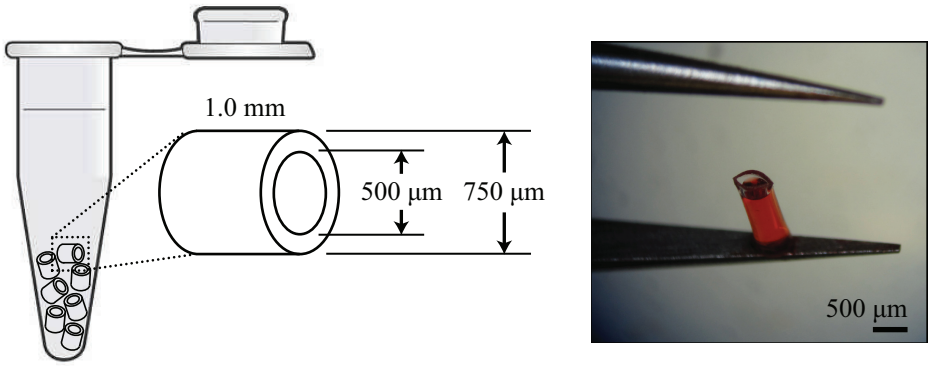

Figure 22: Within conventional PCR tubes, segments of polymer capillaries were submerged in 50 µL PCR reaction volumes (*left*) to quantify the effect of SA:V and passivation on PCR yield (capillaries in tube not shown to scale). Filling of the capillary segments upon submersion was confirmed using food coloring (*right*).

created by the addition of the polymer capillaries serve as a easily controlled analog of the microenvironments of microlfuidic devices. Three different polymers, poly (methyl methacrylate) (PMMA), polycarbonate (PC), and cyclic olefin copolymer (COC) (Zeon Chemicals, Zeonor 1020R), were selected for their known use in the field of polymer microfluidics and their compatibility with our microchip manufacturing techniques. These capillaries, which measured outer diameter, OD=750 µm and inner diameter, ID=500 µm, were diced into 1 mm long segments.

Capillaries were diced manually using a custom-built assembly of razor blades spaced with a 1 mm pitch. Segments were first visually inspected to ensure the capillary was open and then submerged in food coloring to confirm filling of the segments (Figure 22). Small deformation at the ends of the capillary, which was due to pinching of the segments during the dicing process, was tolerated. Once diced, the capillaries were counted and grouped into various batches to achieve a range of SA:V values and loaded into PCR tubes. They were then cleaned by first adding 50 µL of DNase AWAY (Molecular BioProducts), centrifuging and sonicating for 1 hour, drying, and repeating the rinse process twice with nuclease-free water. PCR mixtures were pipetted over the capillaries and spun down, ready for thermocycling.

Capillary dimensions were used for calculations of surface area to determine the number, N, of capillary segments to add to the reactions for a useful range of SA:V values, where $SA = N \times [\pi(ID + OD)L] + [0.5\pi(OD - ID)^2]$. To determine the SA:V of a PCR tube, we added a hemispherical base of radius, R_1 ($SA = 2\pi R_1^2$) to a frustum, the portion of the conical PCR tube that lies between the hemisphere and fill height, h, with radius, R_2 ($SA = \pi(R_1 + R_2)\sqrt{(R_1 - R_2)^2 + h^2}$). For our PCR tubes (Eppendorf, 951010006 Polypropylene PCR Tube, 0.2 mL), R_1=0.92 mm, R_2=1.92 mm, h=6.72 mm. For volumes less than 5 µL, the fill height falls below the top of the hemispherical base and meniscus shape becomes particularly important. For this SA:V calculation, tubes were filled with the low volume, taking care to center it at the base, and the profile was captured using a microscope. The image was imported into CAD software (SolidWorks) where the volume profile was traced and revolved to produce a 3-dimensional representation. Small scaling adjustments were made to ensure the correct total volume and the SA:V values were calculated using the software's measurement features. Although a 50 µL reaction without added capillary segments has a SA:V of 1.3, representing the polypropylene surface contacting the reaction, this was disregarded in our SA:V calculations, since this contribution is roughly constant for each sample, increasing less than 5% of the total SA:V, due to increased height of the liquid in the tube from displacement by the added capillaries, with the maximum added capillaries. Therefore, effective SA:V values were used to represent the contributions of only the substrates of interest, beginning with 0 for the control reaction, 2.2 for 20 segments, 3.2 for 35 segments, and 5.7 for 63 segments.

Using this method of experimentally studying PCR yield as a function of SA:V, we took the opportunity to examine the effects of dynamic passivation. In addition to a baseline set of untreated PCR reactions, two additional conditions were tested: 1) BSA added to the reaction mix immediately prior to thermocycling and 2) BSA incubated with the tubes and capillary segments overnight (∼12 hours) prior to the

addition of the reaction mix and subsequent thermocycling.

For the initial study of the lower limits of reaction volume in convention tubes (Figure 21), we used a consensus degenerate PCR reaction designed by the Centers for Disease Control and Prevention (CDC) for the *Herpesviridae* family with a 605 bp amplicon. The template DNA was a 4,495 bp plasmid containing an Epstein Barr virus (EBV) genomic fragment and flanking regions of a 3,957 bp vector (Invitrogen, pCR®4-TOPO®). Reaction preparation is described in Appendix A. Primers were provided by the CDC and sequences are provided in Appendix B. The standard 45 µL master mix was divided into 4.5, 2.5, 1.5, and 0.5 µL aliquots, respectively, and 0.5 µL of DNA was added to each to yield 5, 3, 2, and 1 µL volumes. 10 µL of mineral oil was added on top of the reaction mixture prior thermocycling to prevent evaporation, keeping the reaction volume confined to the base of the tube.

For characterizing PCR inhibition as a function of material and SA:V, λ-phage amplification with a 500 bp amplicon was used with a 50 µL volume. For this, both BSA and non-BSA containing reactions were prepared. For the non-BSA reactions, a variation of the preparation described in Appendix A was performed to allow for smaller volumes of template DNA where 48 µL of water was added to the premix tube along with 1 µL of forward and reverse primers (Operon) (see Appendix B for sequences). Purified λ DNA (Affymetrix) was diluted to 45.8 ng/µL and 1 µL was added to the master mix. For the BSA containing reactions, 38 µL of water and 10 µL of 1 µg/µL BSA (Affymetrix) was used. For BSA incubated samples, tubes were filled with a 30 µL BSA mixture, which was subtracted from the water volume for the recipe described above, allowing the remaining PCR mixture to be simply added to the incubated capillaries.

Thermocycling was performed in a conventional 48-well thermocycler (Bio-Rad, Bio-Rad MJ Mini). As described in Appendix A, thermocycling parameters were as follows: initial denature at 94°C for 2 minutes, denature at 94°C for 30 seconds,

anneal at 68°C for 30 seconds, extension at 72°C for 30 seconds, and final extension at 72°C for 2 minutes with a total of 30 cycles.

Electrophoretic detection of PCR products was performed with an Agilent 2100 Bioanalyzer, which has a quantitative detection range of 0.1–50 ng/µL. The reactions were considered "successful" if the signal-to-noise ratio of the electrophoretic peak at the target length was greater than three. For successful reactions, the final concentration of amplicon, or PCR yield (ng/µL), was determined from the electropherogram with known standard markers. Although real-time detection would have been preferable to provide quantitative PCR results, our methods required end-point detection. We acknowledge that the use of end-point detection to quantify yield is, at best, semi-quantitative and therefore was one of the primary limitations to the reliability of our surface chemistry characterization efforts. Quantitative PCR (qPCR) provides a more reliable measurement [156] and has been implemented for related studies [126, 135, 134] but was not possible with our thermocycling methods. Additionally, the known adsorption of dyes, such as Sybr Green [135], used for real-time fluorescence monitoring would confound the results. The use of electrophoresis for end-point detection has been used by others to present the effects of material inhibition by reporting the ranges of yield [129]. While we caution that our PCR yield measurements are best for relative trends, the Agilent Bioanalyzers results were consistent and we report ranges of PCR yields for all characterization experiments.

2.4.2 Adsorption model

A theoretical model of adsorption-driven PCR inhibition was developed to complement the experimental characterization of the adverse effects on PCR yield resulting from high SA:V for a variety of substrate materials. We assume that irreversible adsorption of the polymerase enzyme is the cause of inhibition, as supported by previous studies [132, 127]. To construct a model expressing PCR yield as a function of SA:V,

we began with a conservation equation for polymerase availability, noting that

$$C_F V = C_0 V - AS \tag{8}$$

where C_F is the free, or available, concentration of polymerase in solution (molecules/µL), C_0 is the initial polymerase concentration (molecules/µL), A is the surface concentration of adsorbed polymerase (molecules/mm^2), V is volume (µL), and S is surface area (mm^2). The surface adsorption of polymerase has been described by others [136, 68] as

$$A \propto \eta C_F \sqrt{Dt} \tag{9}$$

where η is the adsorption efficiency (%), or the likelihood of an irreversible interaction at the liquid-surface interface, for a particular microchip substrate, D is the diffusivity (m^2/s), and t (sec) is the duration that the reaction is in contact with the substrate surfaces. The $\sqrt{Dt}$ term represents the diffusion distance, d, of a particular particle for a time t. For polymerase, we used an estimated D value of $1{\times}10^{-10}$ m^2/s as reported in literature for an average protein [136, 157]. Substituting Equation 9 into Equation 8 and rearranging, the free concentration of polymerase is given by

$$C_F = \frac{C_0}{1 + \eta \left(\frac{S}{V}\right) \sqrt{Dt}} \tag{10}$$

where S/V is identically SA:V. At high SA:V, free polymerase concentration limits PCR yield, such that $C_F \propto Y$. Therefore, PCR yield is expressed by

$$Y = \frac{Y_0}{1 + \eta \left(\frac{S}{V}\right) \sqrt{Dt}} \tag{11}$$

where Y_0 is PCR yield when SA:V=0, which corresponds to the yield for the control reaction. Because of the many factors contributing to the likelihood of irreversible interaction between a protein and polymer surface, there is no deterministic method for finding adsorption efficiency, η, from material properties. Instead, η values were calculated using a least squares fit to our experimental data sets for each substrate

of interest. Therefore, η serves as a collective empirical term for the probability of an irreversible interaction between the polymerase enzyme and polymer surface as commonly occurring in microfluidic PCR devices. This term provides a valuable basis for comparing materials and predicting geometry effects but has several limitations, including the assumptions of fully diffusive transport, that polymerase is the only adsorbed reagent, and that adsorption is irreversible and completely inhibitory to enzyme function. In addition, the model does not account for surface roughness, the effect of temperature fluctuations on diffusivity, or the effects of passivation. The model could benefit from a larger sample number and greater range of SA:V, since the experiments presented here were limited to range of ∼1-6 while some microfluidic devices approach higher values (e.g., SA:V=22 [158]. These high SA:V devices, in all reported experiments, require passivation techniques to obtain reasonable yields.

This adsorption model was also used to compute the critical length, d, derived from the diffusion length calculation, at which wall interactions become dominant. Using our values for diffusivity of polymerase (1×10^{-10} m^2/s) and a time of 2 hours (7200 s), we note the critical length, d=800 µm. For devices with reaction chamber dimensions below this critical length, we predict enzyme depletion due to wall interaction will significantly affect yield unless counteracted with passivation measures.

Results from the capillary segment experiments are shown in Figure 23. By varying the SA:V from 0 to 5.7, we showed a decaying PCR yield with increasing SA:V in the absence of passivation. The capillary segments used have dimensions less than the diffusion distance, d, thus we observed strong dependency of yield on SA:V. Using a least squares fit to this data, we determined adsorption efficiency, η, for PMMA, PC, and COC to be 0.91, 0.38, and 0.31, respectively. PC and COC give similar results ($p>0.05$), and PMMA is the worst option amongst these three material candidates since it fails at SA:V=5.7, while COC and PC can work at this high SA:V. This conclusion is in agreement with the assessments found in literature [129]. In this work

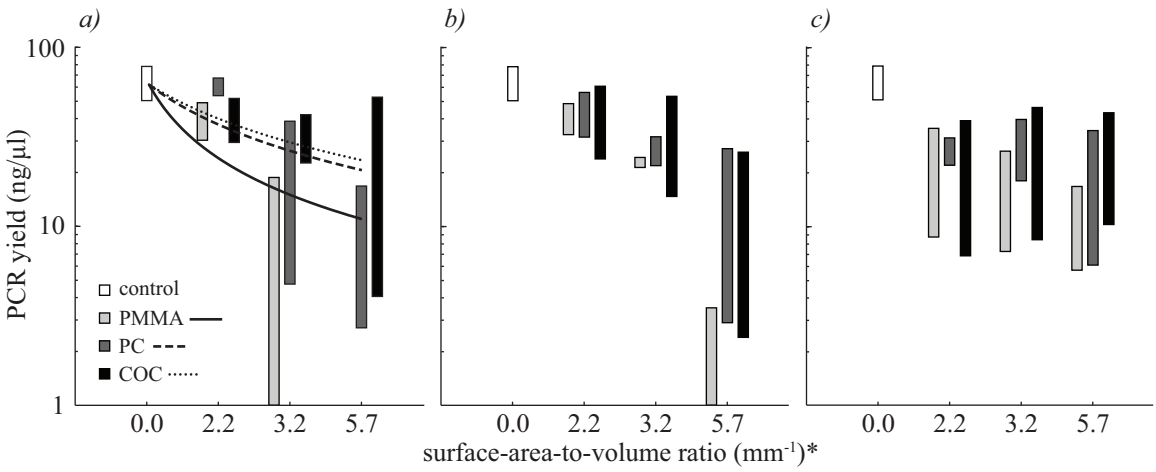

Figure 23: Experimental PCR yield ranges (bars) in the presence of PMMA, PC, and COC capillary segments versus SA:V for (a) untreated PCR solution as well as for dynamic passivation using BSA added to the PCR solution (b) immediately prior and (c) 12 hours prior (overnight incubation) to thermocycling. Modeled yields (lines) are shown for the untreated case in part (a). Reaction parameters: conventional PCR tubes with capillary segments, 45.8 ng of λ template, 30 cycles, 50 µL total volume, control has no segments, BSA concentration 0.2 µg/µL (when applicable), n=2. *Surface area of polypropylene PCR tube neglected

we have not tested nor determined η values for other microfluidic materials, such as PDMS, polyester, glass, or silicon.

The yield at high SA:V (e.g., >3) is improved and stabilized by the addition of BSA, especially so when the sample is incubated with BSA before loading the reaction. This stabilization of yield makes PCR viable at SA:V as high as 5.7 for all substrates tested in this work.

The adsorption model (Equation 11), shown superimposed over experimental data in Figure 23a, predicted η values for PMMA, PC, and COC to be 0.91, 0.38, and 0.31, respectively. Overall, the adverse effect of increasing SA:V is apparent in the decreasing yield for each substrate. COC appears to be the most compatible polymer, with PC displaying slightly lower but not significantly different ($p>0.05$ at each SA:V) final concentrations. PMMA was the weakest performer.

It must be noted that this theoretical model takes into consideration a only a

limited number of variables. As it stands, the model can serve as a tool for characterization purposes, using SA:V, substrate-dependent adsorption efficiency, initial concentration of polymerase, diffusivity of polymerase, and duration of reaction/chamber interaction to determine the suitability of a particular material for use as a microfluidic substrate. By fitting this diffusion model, using the method of least squares, to our empirical observations of PCR yield for reactions performed in three polymer environments (PMMA, PC, and COC), we have been able to calculate corresponding adsorption efficiencies, η, a metric we created to represent the tendency for molecules to irreversibly adsorb to a particular material. Additional efforts towards developing the model into a deterministic tool are discussed later in Section 5.2.1.

2.4.3 Microchip passivation

Although our study of reaction inhibition as a function of the three most common rigid polymers used for microfluidic substrates revealed that PMMA was the least suitable for PCR, we proceeded to test our PMMA microchips (SA:V=7.0) with both dynamic passivation via BSA and two static passivation methods: 1) using a sample loading technique we developed involving mineral oil and 2) using covalent surface modification of PMMA via silanization. These passivation strategies were first tested using our λ-phage amplification and compared to control reactions to determine whether our choice of PMMA as a microchip substrate was viable and, if so, proceed to apply the optimal protocol to test for sensitivity and specificity with a more challenging reaction.

Microchip reactions were thermocycled using a custom-built, automated water bath system (Figure 24). Three 1 L beakers of water were maintained at the denaturing, annealing, and extension temperatures using hot plates with temperature probes for feedback control (Corning, 6795-420D). Microchips were transferred between the water baths in an aluminum microchip holder, which was shuttled on a 2-axis gantry

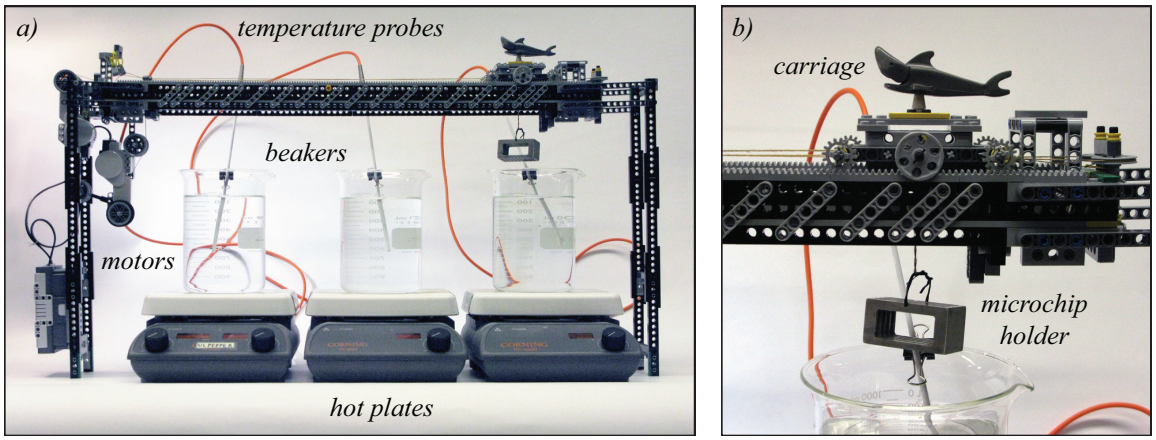

Figure 24: An automated water bath thermocycler was built for testing our microchips with different passivation methods and PCR reaction to confirm compatibility and assess performance such as limit of detection. (a) A 2-axis gantry system was positioned over three 1 L beakers, each maintained at one of the three PCR temperature setpoints for denaturation, annealing, and extension. (b) The carriage shuttled a microchip holder between beakers, pausing at each beaker to allow submersion of the microchips for specified hold times.

system built using LEGO Mindstorms NXT as well as added materials such as kevlar thread for a pulley system used to raise and lower the microchip holder into and out of the water baths. A LabVIEW program served as the user interface, allowing control o. Hold times were extended to ensure thermal equilibrium as follows. For the crucial transitions to annealing (94°C to 68°C) and extension (68°C to 72°C) temperatures, 1.5 minutes of ramping time was determined as more than adequate using a microthermocouple (Physitemp Instruments, T-240C) inserted into the reaction chamber. For the less critical denaturing transition (72°C to 94°C), 30 seconds of ramping time was used to quickly reach denaturing without risk of enzyme degradation, bubble formation, or material softening.

Following thermocycling, we inspected all microchips for air bubble entrainment in the reaction chambers. We discarded roughly 48% (19 out of 40) of the microchips when air bubbles were visible by naked eye, since preliminary studies showed that PCR was 100% (15 out of 15) inhibited by their presence, most likely due to the disruption of the oil passivation layer by the bubble, allowing direct contact between

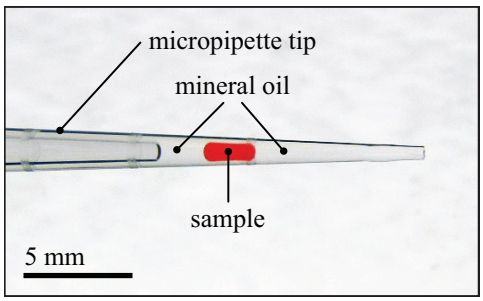

Figure 25: A technique for loading PCR samples into our polymer microchips (shown in Figure 17) was developed in which a standard pipette tip is loaded with 1 µL PCR sample flanked by 2 µL volumes of mineral oil.

the reaction and inhibiting polymer surface.

2.4.3.1 Mineral oil loading

A new approach for loading aqueous samples into static reaction chambers was developed in which the sample is loaded as a plug between two volumes of mineral oil, filling the ports and fill channels and thereby eliminating dead volume. This technique was performed by first loading 2 µL of mineral oil into a pipette tip using an adjustable micropipette. The pipettor volume was increased to 3 µL and, after carefully bringing the oil interface to the end of the pipette tip, 1 µL of PCR solution was loaded. The pipettor volume was then increased to 5 µL and the remaining 2 µL section of the pipette tip was filled with a second flanking plug of mineral oil, as pictured in Figure 25. This 5 µL volume was loaded into the microchip, aligning the PCR solution to the reaction chamber. Excess mineral oil overflow was wiped away with a lint-free wipe. Upon visual observation at 20× magnification, the oil appeared to form a smooth boundary between the sample and chamber walls, suggesting encapsulation of the sample.

Confocal imaging was used to examine the extent of sample encapsulation achieved by the mineral oil loading technique. Fluorescent mineral oil was made using acetylated low density lipoprotein, labeled with 1,1'-dioctadecyl–3,3,3',3'-tetramethyl-indocarbocyanine perchlorate (Biomedical Technologies Inc., DiI-Ac-LDL). 5 mL of mineral oil was

added to 200 µg of fluorophore and vortexed, yielding a 40 µg/mL solution. A microchip was specially made for this experiment. It featured three reaction chambers and, instead of the typical 1.5 mm thick layer thermally bonded to the enclose the reaction chambers, a 200 µm PMMA layer was used to allow for imaging of the reaction chambers to accommodate the limited working distance of the microscope objective. The microchip was filled using the same loading process previously described using the fluorescent mineral oil and 1 µL of PCR buffer solution to serve as the sample. It was then positioned on the stage of a confocal microscope (Zeiss, LSM 510). Each chamber was imaged with a tile scan of z-stacks to capture the three-dimensional distribution of mineral oil. Acquisition settings were configured for the DiI fluorescent probe, including laser excitation at 555 nm, and z-stacks were set for 120 slices over the full chamber depth, yielding a z-stack interval of roughly 6.4 µm. Resulting confocal images of three identically filled chambers are shown in isometric view in Figure 26. The three-dimensional reconstructions of the mineral oil distribution indicate partial passivation, separating the sample from the microchip substrate in some areas but leaving some regions exposed to the polymer. Another possibility is that although complete sample encapsulation occurred, the layer of mineral oil surrounding the sample was too thin in certain regions for enough fluorescent molecules to produce a detectable signal.

2.4.3.2 Hydrophilic and hydrophobic coating

In addition to the oil loading technique, covalent surface modification via silanization was implemented as another countermeasure to geometry and material-dependent PCR inhibition [159, 160, 161, 162]. Specifically, two hydrophilic coatings, (3-aminopropyl) triethoxysilane (Sigma-Aldrich, 440140) and mPEG-triethoxysilane (Laysan Bio, MPEG-SIL-1000-1g), and two hydrophobic coatings, n-propyl-triethoxysilane (Sigma-Aldrich, 539317) and isobutyltriethoxysilane (Sigma, 699713), were selected for testing. It

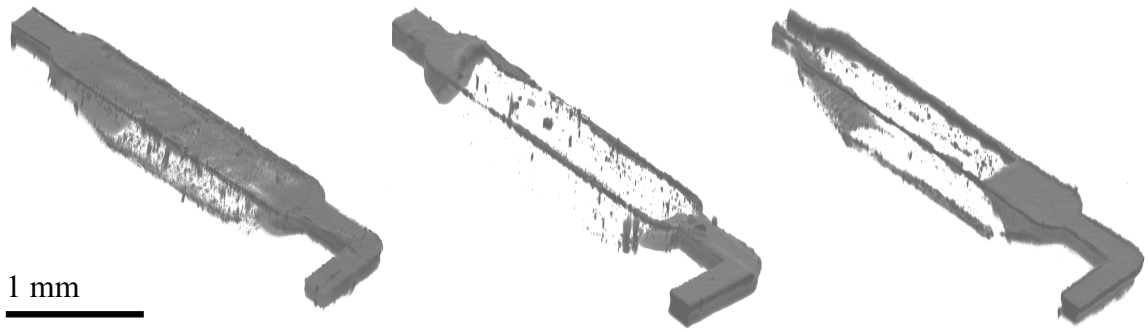

Figure 26: Confocal imaging was used to determine the nature of the passivation provided by our oil loading technique. Mineral oil was treated with a fluorescent probe solution and used to load 1 µL water samples into our microchip. Three-dimensional reconstructions of image stacks collected for three separate reaction chambers loaded with the identical technique indicate only partial passivation by the mineral oil and reveal trial-to-trial variation in oil distribution.

was hypothesized that hydrophilic coatings, when paired with the direct loading of samples into the microchip, would minimize the occurrence of surface energy-related adsorption of PCR reagents and in turn enhance PCR yield. Hydrophobic coatings would be paired with the oil loading method to ensure complete encapsulation of the aqueous sample in mineral oil, preventing and surface chemistry-related inhibition.

All of the silane solutions were purchased in liquid form, ready to use, with the exception of the 1,000 Da mPEG-silane, which was stored in powder form. 100 µL aliquots were prepared by first combining 95 µL with 5 µL deionized water to make the PEGylation buffer. Then 5 mg of mPEG-silane was added to the buffer and the solution was vortexed until all powder was dissolved.

The coating process was performed prior to thermal bonding. After cleaning the microchip layers with ethanol, deionized water, and compressed N_2, each side was masked using general-purpose labeling tape to expose only the regions where the micro-milled features were located, coating only the surfaces that will later contact the sample and leaving the rest of the interfacial area uncoated to ensure proper bonding. Functionalization was performed as shown in Figure 27, in which the masked

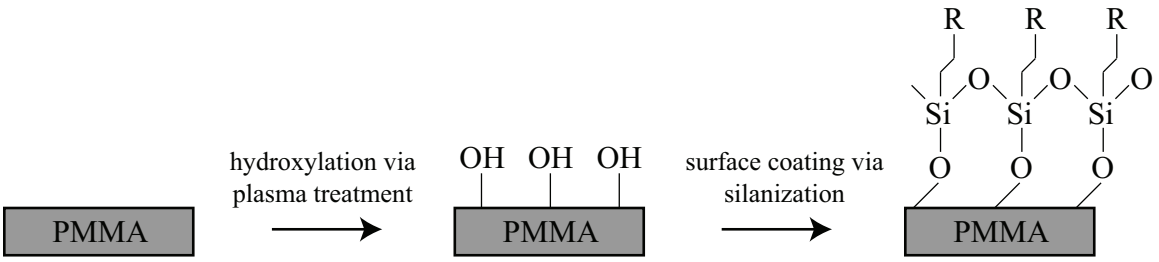

Figure 27: Surface modification of our PMMA microchip was performed by first plasma treating the surface to expose hydroxyl groups then incubating with silane solution to coat the device, changing surface properties and potentially improving biocompatibility with PCR. Diagram adapted from [161].

layers were plasma treated (Harrick Plasma, PDC-32G) for 2 minutes to expose hydroxyl groups then immediately treated with the silane solutions by pipetting roughly 10 µL onto the exposed regions. The microchip layers were then incubated at 70°C for 2 hours. The tape used for the mask was removed and the microchip was bonded according to the standard method described in Section 2.2.2. Early experiments with the coatings revealed that the amine-modified surface via (3-aminopropyl) triethoxysilane was opaque upon drying and therefore unsuitable for use with our microchips since the coating would both impede infrared heating and prevent optical access required for applications involving real-time fluorescence monitoring. We proceeded with the remaining three formulations.

To determine whether the silane coatings would survive the thermal bonding process, coated microchip layers were loaded onto the unassembled sides of the bonding fixture, placed on the hot plate, and subjected to the same temperatures experienced during the bonding process but without the assembly and clamping of the fixture, keeping the coatings exposed. Following this heating process, the microchip layers were allowed to cool and 5 µL water droplets were deposited onto the coated regions. Comparison of contact angles from before and after heating indicated that the silane coatings withstood the bonding temperatures, validating the coating method for use with our microchips.

A set of five 8-chamber microchips were used for testing our microchip passivation methods. For each microchip, four of the reaction chambers were used without BSA and four without BSA. Two of the microchips were uncoated, one loaded with PCR solution only and other other loaded with the mineral oil loading method. The remaining three microchips were coated using the silane treatments: mPEG-triethoxysilane (hydrophilic), n-propyl-triethoxysilane (hydrophobic) and isobutyltriethoxysilane (hydrophobic). The hydrophilic microchip was loaded with PCR solution only and the hydrophobic microchips were loaded using the mineral oil loading method. It was discovered during the loading process that the hydrophobic coatings prevented injection of the aqueous samples due to the non-wettable surfaces; therefore, the only covalently modified microchip tested was the PEGylated device, leaving three out of the initial five microchips for testing.

For a reliable test of the efficacy of these passivation methods, λ-phage amplification was used. For the non-BSA preparation, see Appendix A. For the BSA containing reactions, the same protocol was used except the volume of water added was reduced to 29 µL and 15 µL of 1 µg/µL BSA was added to the premix prior to vortexing. The 5 µL aliquots were then used for loading into the microchip. In the case of the mineral oil loading approach, only 1 µL was needed. With the mineral oil, roughly 3 µL were required for filling not only the reaction chamber but also the fill channels and ports. Our custom water bath thermocycler was used with hold times of 1, 2, and 2 minutes for denature, anneal, and extension, respectively, for 30 cycles.

The PCR yields for λ-phage amplification in our three tested microchips are shown in Figure 28 compared to 50 µL control reactions in conventional PCR tubes with and without BSA. As before, PMMA at high SA:V (in the microchip) without passivation consistently fails and has a low but consistently detectable yield with BSA. The favorable effect of the mineral oil loading method on PCR yield compared to the untreated microchip without oil was significantly different ($p<0.05$). Despite the

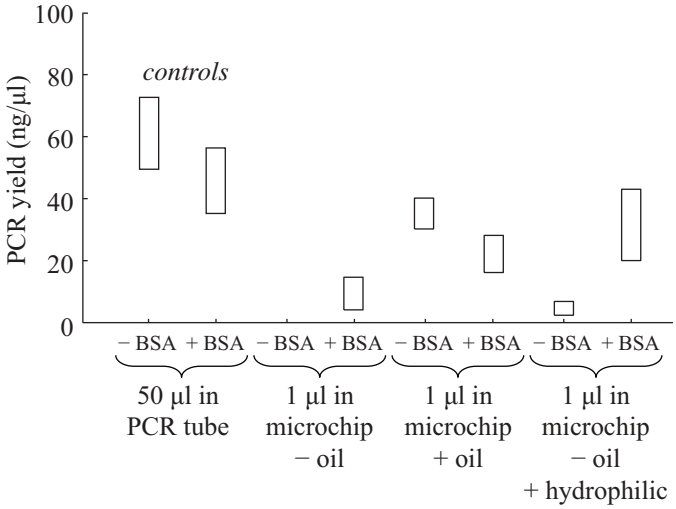

Figure 28: PCR yield for various passivation methods in PMMA microchips relative to control reactions in PCR tubes with and without BSA. Three microchips were run in a custom water bath thermocycler to test the efficacy of an oil loading technique as well as a PEG-silane hydrophilic coating compared to an untreated microchip. Reaction parameters: control in conventional PCR tubes, microchips in PMMA with SA:V=7.0, λ template (45.8 ng in controls, 25 ng in microchips), 30 cycles, BSA concentration 0.3 µg/µL, n=4.

benefits of BSA as a dynamic passivation agent observed from experiments in conventional tubes with either low volumes or high SA:V environments (Figures 21 and 23), the exclusion of BSA improved yields for both mineral oil loaded samples and the 50 µL control. This seems to agree with what others have posited [126], that BSA effects can be deleterious. As the effects of BSA on the reaction chemistry and wall interaction are complex [163, 164, 133], we are reluctant to extend the model to account for it. Suffice to say that the η term and Y_0 terms would at least be affected.

Since oil encapsulation performed the passivation function, BSA addition is therefore not recommended. Although comparable performance was observed for the hydrophilic microchip when used with a BSA containing PCR solution, greater variability in PCR yield indicated a less reliable passivation method. Thus, the combined benefits of relatively high PCR yields and zero dead volume motivated our selection of mineral oil loading without BSA as the optimal passivation strategy for our PMMA microchips.

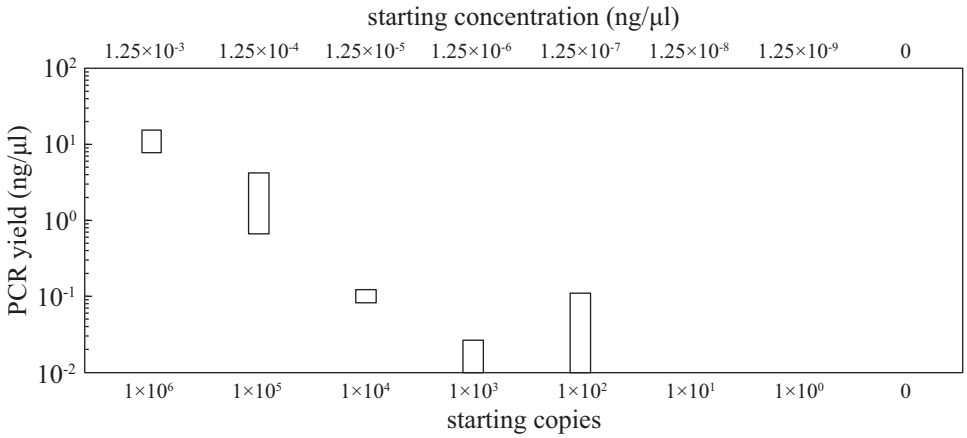

Figure 29: To assess sensitivity, PCR yield versus starting copies of Epstein Barr virus using 1 µL PMMA microchips. Limit of detection is 140 starting copies, equivalently 1.25×10^{-7} ng/µL or 3×10^{5} copies/mL. Reaction parameters: EBV template, 30 cycles, n=3.

Having established the basic viability of our microchip when paired with an effective passivation method, we proceeded to test the limits of performance when faced with a more challenging amplification reaction. Consensus degenerate PCR was selected for these purposes and the previously described EBV reaction was run in our microchips. Refer to Appendix A for a detailed protocol for reaction preparation. The virus template DNA was added from a set of serial dilutions, which was prepared with concentrations ranging from 1.25×10^{-3} ng/µL (1.4×10^{6} copies/reaction) to extinction in 10× dilution increments, to assess sensitivity.

As detailed in Appendix A, conventional thermocycling parameters for EBV amplification were as follows: initial denature at 94°C for 2 minutes, denature at 94°C for 15 seconds, annealing at 48°C for 30 seconds, extension at 72°C for 30 seconds, and final extension at 72°C for 7 minutes with a total of 40 cycles. For the microchip reactions, the water bath system previously described was used with hold times were 1, 3, and 2 minutes for 30 cycles.

Using the PMMA microchip (volume=1 µL, SA:V=7.0) with optimal passivation of oil without BSA, we performed amplifications of an EBV genomic fragment using

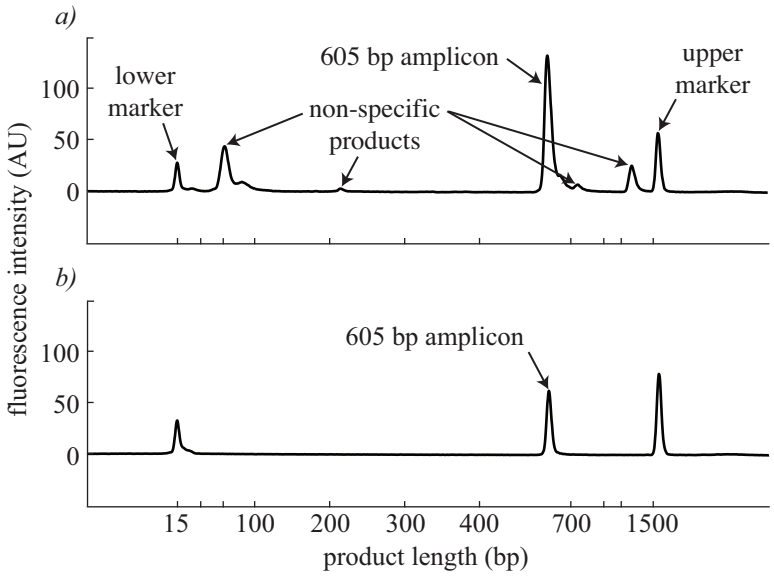

Figure 30: To assess specificity, electropherograms of PCR products and sizing markers for amplifications of 10^6 copies, or 1.25 ng, of Epstein Barr virus with 2.5 ng of background human DNA for (a) 5 µL reaction volumes in a conventional PCR tube and (b) 1 µL microchip. The target amplicon of 605 bp is detected in both, but the specificity (indicated by the presence of non-specific products) is superior for the microchip. One of two identical results is shown. Reaction parameters: EBV template, 30 cycles.

pan herpes virus consensus degenerate PCR with a serial dilution of template from 0 to 10^6 starting copies to determine the sensitivity of this optimized microfluidic device. The results with corresponding starting concentration and yield are shown in Figure 29. The samples were successfully amplified down to the threshold of ∼100 starting copies, near the limit of detection of conventional thermocycling.

In order to assess specificity, 5 ng/µL human DNA was introduced to the reaction mixtures to represent host, or background, DNA. A comparison of a 5 µL conventional reaction in a tube and a 1 µL reaction in our microchip was performed, each containing 2.5 ng of host DNA and 1.25 ng of EBV template.

To assess specificity of the 1 µL PMMA microchips, we amplified 10^6 starting copies, or 1.25 ng, of EBV template in the presence of 2.5 ng of host human DNA. For comparison, we amplified the same quantity of template and host in a 5 µL conventional PCR tube. The resulting electropherograms of the PCR products are

shown in Figure 30. Non-specific products and primer dimers were easily observable in the 5 µL sample run in a conventional PCR tube. The sample run on the microchip, on the other hand, yielded a much cleaner electropherogram, free of undesirable peaks. Qualitatively, the microchip exhibits improved specificity.

In order for the molecular biology community to embrace new technologies such as microfluidic PCR, the sensitivity and specificity capabilities for the most challenging and relevant reactions must compare or exceed those of conventional techniques while offering an easy-to-use, low-cost system. We have demonstrated a microfluidic PCR approach informed by modeling and experimental characterization of the common problem of inhibition by surface adsorption and factors that affect it: substrate material, duration, diffusivity, surface area-to-volume ratio, and passivation technique. From this, we have implemented optimal passivation for a 1 µL reaction volume in a polymer microchip that we fabricated, providing a 50× volume reduction compared to conventional methods with comparable or improved sensitivity and specificity. Unlike the many microfluidic PCR devices that require higher concentrations of polymerase, which is the most expensive PCR reagent, we maintain the conventional polymerase concentration of 0.025 U/µL to provide true cost reduction. The application of our microchip to the detection of Epstein Barr virus using pan herpes virus consensus degenerate primers, as routinely used by the CDC Pathogen Discovery Program, Division of Viral Disease, and our demonstrated ability to operate at the same limit of detection and specificity as conventional methods makes the case for the viability of our microchip, taking a step closer to massive reductions in the cost and labor involved in pathogen screening and countless other PCR applications.

2.5 Conclusions

This chapter described the design, fabrication, and testing of a low-cost microfluidic device for rapid PCR applications such as viral screening. Towards the design of our

device, a finite element model was developed and validated, allowing for the iterative simulation of various geometries and materials to arrive at a 1 µL reaction chamber design suitable for efficient radiative heating, as required for performing thermocycling with minimal power consumption and maximal scaling potential.

With an established design, numerous fabrication methods were tested, including hot embossing, injection molding, and laser ablation. Ultimately, a direct micro-milling approach was developed that made use of a CNC machine equipped with a spindle capable of high enough speeds to operate sub-millimeter tooling. This technique was amenable to our three-dimensional reaction chamber geometry and allowed for fast prototyping of new designs, unlike most micro-fabrication methods that either involve numerous steps with expensive and sometimes hazardous chemicals or require the separate fabrication of a mold.

For the optimal performance of our device, problems of bubble formation and surface chemistry-related inhibition needed to be addressed. A system for pressurizing our samples during instrument operation suppressed the expansion of small pockets of trapped air observed at the near-boiling temperatures required for PCR thermocycling. Next, the commonly encountered issue of adsorption of molecules to the inner surfaces of the microfluidic features, which can partially or fully inhibit the relevant biochemical reaction, was addressed by first conducting a systematic characterization of the effects of various surface-area-to-volume ratios and various polymeric materials on PCR yield. A theoretical model based on diffusive transport was developed in parallel with the experimental work, laying the groundwork for a deterministic approach for predicting inhibition effects as a function of geometry and material properties.

We then implemented a number of methods designed to counteract the adsorption-driven inhibition, including dynamic BSA passivation, covalent surface modification via silane conjugation, and loading of samples using mineral oil encapsulation. The mineral oil loading technique proved to be most effective and offered the added benefit

of eliminating dead volume. This approach enabled the first microfluidic consensus degenerate PCR with the amplification of EBV by pan herpes virus PCR as a proof of concept. Our limit of detection was shown to be comparable to conventional tubes, with 140 starting copies or 3×10^5 copies/ml regarded as the accepted sensitivity threshold for diagnostic purposes [155] These discoveries relating to the modeling, fabrication, and optimization of our microchip yielded the core enabling feature of a rapid, low-cost, microfluidic PCR platform.

CHAPTER III

LASER-MEDIATED THERMOCYCLER

The polymerase chain reaction is a temperature-driven process. Therefore, fast and reliable temperature control is an essential component of any high performance PCR system. This chapter describes the development of an infrared laser-mediated method of controlling the temperature of a microfluidic sample while providing fast ramping and independent temperature control of multiple reaction chambers to achieve thermal multiplexing, a novel concept introduced earlier in Section 1.5. We first discuss the methods for delivering radiation to our microfluidic reaction chambers, including the distribution, alignment, and modulation of our laser output. Next, the temperature measurement system used for feedback-driven control and the associated calibration process is described. Finally, both open-loop and closed-loop configurations are implemented for applications in gene expression measurement and multiplexed virus detection. The core of our two-channel thermocycler is shown in the simplified diagram of our system depicted in Figure 31.

3.1 Optical system

The evolution of radiative heating for microfluidic PCR from its origins, in which an incoherent, broadband source was used to generate large focal spots on glass microfluidic devices, to a more precise and scalable approach using a coherent, monochromatic source was driven by the design and construction of an optical system capable of efficient and controlled delivery of radiation to our microchip.

Two basic optical system configurations were developed, each shown in Figure 32. With a two-chamber approach selected as the proof-of-concept for our technology, we needed a way to deliver radiation equally to two samples simultaneously. Initial

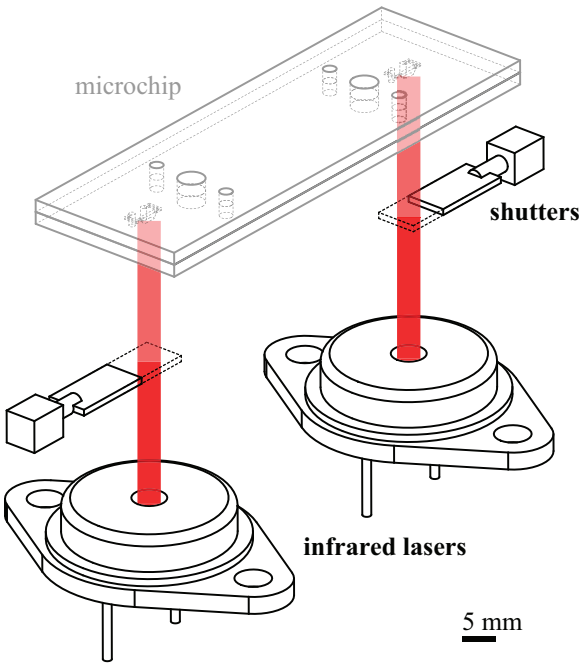

Figure 31: A simplified diagram of our two-channel temperature control system. Laser diodes served as the source of infrared radiation and solenoid shutters modulated the radiation to provide independent temperature control of each reaction chamber. (Optics, pressurization, and temperature sensors excluded for clarity.)

design efforts considered optical elements such as beam splitters and micro mirror arrays to distribute the infrared radiation but high component costs and excessive attenuation eliminated these options. Instead, a simple approach was adopted in which the beam was first collimated, and in the case of a single source, divided using a lens array, then modulated using miniature solenoids acting as optical shutters. The single laser configuration was first developed, as shown in Figure 32a, in which a collimating lens and lens array are used to generate two equally sized focal spots spaced 1 mm center-to-center (Figure 32b) and aligned to adjacent reaction chambers with the same spacing. After determining the relationship between chamber spacing and maximum temperature difference, relevant for operating at different annealing temperatures simultaneously as required for thermal multiplexing, a second configuration was developed in which two laser sources were used, shown in Figure 32c. As explained in the discussion of chamber spacing covered in Section 2.1.3, the use

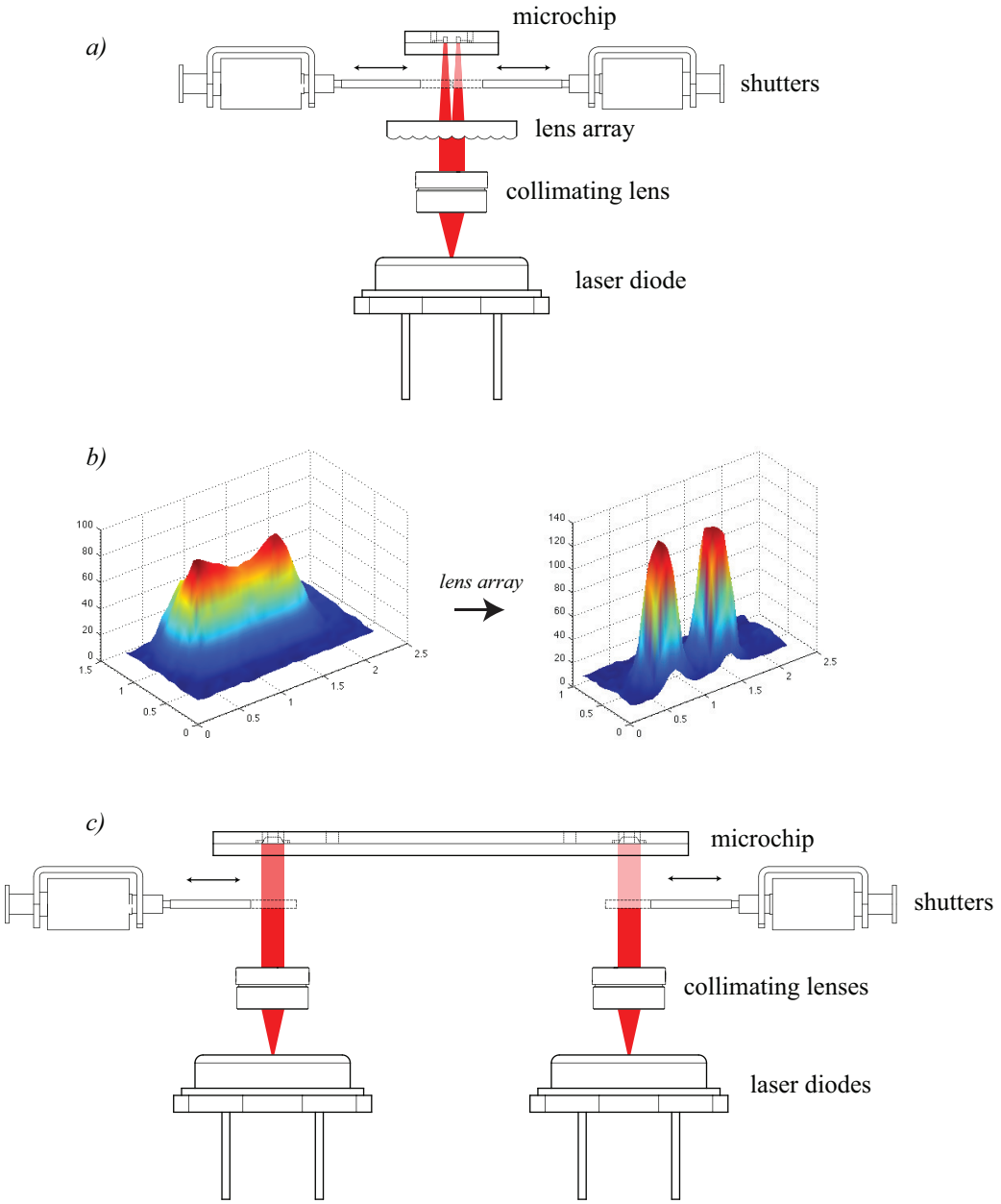

Figure 32: The basic optical systems for two-chamber, laser-mediated thermocycling used collimation and modulation optics for manipulating our infrared sources. (a) For closely-spaced reaction chambers, a single source can be collimated and evenly divided into distinct focal spots using a lens array. (b) The transformation of the beam profile from its passage through the lens array. (c) For widely-spaced reaction chambers, as required for sufficient thermal isolation, two laser sources were implemented with mirrored optical elements.

of side-by-side 30 mm cage systems to mount and align the optics required for each channel dictated the 40 mm center-to-center spacing of the reaction chambers.

3.1.1 Laser source

With the goal of efficient, localized radiative heating of aqueous samples, an infrared laser was selected as an ideal source. This offers numerous advantages, including the ability to finely focus and manipulate the beam and the ability to more easily control the level of interaction between the radiation and the instrument components due to the specificity of the laser's narrow spectral bandwidth. As mentioned in Section 2.1.4, a wavelength of 1450 nm was selected for both its commercial availability and affordability and, more importantly, it corresponds to an absorption peak of water while absorption by our microchip substrate, PMMA, is negligible, allowing efficient delivery of radiation without heating and damaging the microchip.

The modeling presented in Section 2.1.1 assisted in not only the design our microchip but also the selection of our laser source. Based on our combined calculations of optical power absorption and finite element heat transfer simulations, we chose a 600 mW 1450 nm laser diode (Hi-Tech Optoelectronics, LMD-1450-600-33) as the best suited source for adequate power and affordability (e.g., $100 per laser diode). The laser features a rugged TO-3 packaging with a flange featuring two holes, which were used to rigidly mount the laser to a heat sink with thermal paste applied at the interface. The diode is wiring in an anode grounded configuration and powered using a constant current laser diode driver (Wavelength Electronics, PLD5K-CH), which can supply up to 5 A and achieves drive current stability of <100 ppm, which is equivalent to <0.3 µA variation when operating at our maximum current draw of 3 A. This complied with the maximum tolerable transient reverse current of 25 µA for our laser diode. Power consumption amounted to roughly 3.25–6.5 W, an order of magnitude less than typical Peltier-based thermocyclers.

Initial testing for our laser with an early polymer microchip design provided a benchmark for temperature ramping rate of 60°/sec, as plotted in Figure 33. This is more than an order of magnitude greater than the maximum ramping rates of conventional thermocyclers (e.g., 3°/sec), an improvement that can be attributed to the direct nature of energy transfer via radiative heating and the smaller thermal mass of our sample compared to the thermal block that must be heated/cooled for the indirect temperature control of larger sample volumes encountered with the conventional Peltier-based systems. While the faster ramping achieved using our infrared laser system does result in shorter overall runtimes, the benefit from ramping alone is not significant due to the relatively greater time commitment for temperature holds compared to the transition periods over the course of 30 to 40 cycles. There is potential for greater time reduction by reducing the hold times recommended for conventional instrumentation, since the smaller thermal mass of our 1 µL sample reaches its setpoint faster than the larger volumes used with conventional systems, especially since they measure the temperature of the thermal block and most likely allot extra time during the holds for the sample to come into equilibrium with the block. Still, we see the enhanced speed of our system as only a minor advantage, whereas the efficiency and controllability of our laser-mediated thermocycler are the key features enabling our innovations in the field of PCR instrumentation and more broadly in applications of microfluidic temperature control.

Each laser diode, which exhibited beam divergence of approximately 45° × 11° full width at half maximum (FWHM), was focused using an aspheric lens (Thorlabs, A230TM-C) with a focal length of 4.51 mm, numerical aperture (NA) of 0.54, and an antireflective (AR) coating designed for the 1050–1620 nm wavelength range. These collimating lenses were adjusted to positions outside of the plane of collimation to achieve slight focusing of the beam in order to approximately match the focal spot to the 500 µm × 2.75 mm dimensions of the reaction chamber.

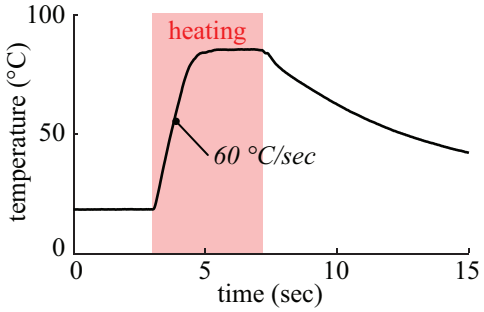

Figure 33: The fastest recorded ramping rate achieved with our infrared laser heating system was 60°C/sec when heating a 200 nL sample volume in an early PET microchip design.

For the two-chamber, single laser system, an injection molded lens array with 1 mm interlens spacing was used as well[98]. This served the purpose of efficiently distributing the single beam to both chambers. The beam profile before and after the lens array can be seen in Figure 32b.

3.1.2 Alignment

As discussed later in Section 3.3, there are two versions of our instrument, one for open-loop operation and the other for closed-loop operation. The core optical system for mounting, aligning, and focusing our infrared lasers is shared by both systems but the proceeding discussion pertains to the closed-loop configuration due to its greater complexity and relevance to the overall goals of this research.

Basic alignment of the optical system was achieved through the use of a commercial 30 mm cage system (Thorlabs). Anodized aluminum cage plates, which feature holes or threads specific to the optical element mounted to it as well as a set of precisely reamed holes spaced 30 mm center-to-center for aligning the plate to a set of 6 mm diameter construction rods with a sliding fit. Set screws fix the plates in their positions along the optical axis. At the base of the optical system were cage plates specifically designed for TO-3 packaging geometry (Thorlabs, CP04), which were used to mount the laser diodes.

Collimating lenses (Thorlabs, A230TM-C) were then installed in the optical system using cage plates featuring x-y translating lens mounts (Thorlabs, CXY1). These plates were positioned against the top of the laser diodes and a spanner wrench was then used to screw the threaded collimating lens to the appropriate depth for the desired focal spot. A VIS/IR viewing card (Thorlabs, VRC2) positioned at the midplane of the microchip was used to visualize the focal spot during these adjustments. Following the collimating lenses, the next component encountered in the beam path was the shutters, which were installed in the optical system on custom brackets made by modifying blank cage plates (Thorlabs, CP01) to accommodate the miniature solenoids, including slots for sliding the solenoid into the optimal position before tightening them in place using 1-72 machine screws. Finally, the pressure manifold, which was discussed in Section 2.3 and shown in Figure 18, is aligned to the optical system on the outermost four construction rods, which are longer than the inner rods for this purpose. Precision fabrication via CNC machining and the use of a 6.03 mm reamer (Guhring, 6.03 mm HSS-E Chucking Reamer) for the alignment holes interfacing with the optical system's 6 mm construction rods ensured a precise sliding fit. Since the microchip is precisely mounted to the pressure manifold using press-fit 1/16 inch dowel pins, the mounting of the manifold aligns the microchip to the optical system. Once the optimal spacing for these components was determined, spacers were milled from modified blank cage plates to slide on the construction rods, allowing for the repeatable removal and reinstalling of the optical shutter mounts and pressure manifold / microchip assembly. The optical system can be seen in Figure 49.

The x-y translation mounts housing the collimating lenses provided fine adjustment (0.25 mm per rotation of positioner knob, ± 1 mm travel) to the laser beam position, allowing us to align each focal spot to the reaction chamber. This alignment was performed by taping burn paper, which was made using PET transparencies printed with two layers of black toner, to the microchip. Briefly powering the laser

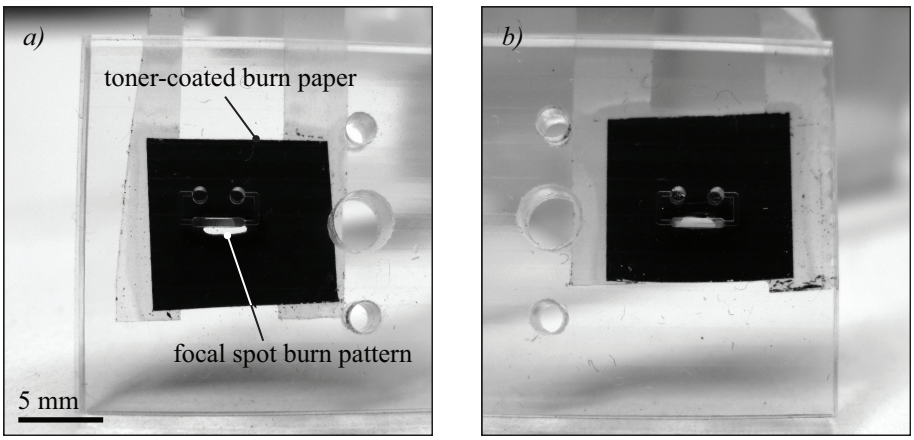

Figure 34: In order to align our lasers to the 1 µL reaction chambers of our PMMA microchips, a toner-coated sheet of PET was used as burn paper, allowing for the visualization of the focal spot after briefly powering the lasers. (a) Misaligned and (b) aligned focal spots can be seen with respect to the reaction chambers.

generated a burn pattern, allowing us to visualize of the focal spot and determine the degree of alignment. Figure 34 shows this process with examples of misaligned and aligned focal spots.

In addition to aligning the laser focal spots to the reaction chambers, the two-chamber instrument required identical laser alignment for each reaction chamber to match heating rates and allow the temperatures in each chamber to closely track each other. For this, care was taken to match the focal spot sizes by replicating the collimating lenses positions in the optical axis. A power meter was used to confirm equal optical power output from each laser. For final alignment, a microchip with embedded thermocouples was loaded with PCR buffer in each chamber, installed on the laser thermocycler, and heated. Fine adjustments to the x-y positions of the collimating lenses were then made to match steady state temperatures in each chamber.

To measure the z-axis repeatability of our method of aligning our microchip to our optical system, our instrument was mounted to a microscope stage. We focused on both a stationary chip and a successively removed and replaced chip. From the

stationary chip, we ascertained from five measurements that the standard deviation of the focusing error was 9.9 µm. From five measurements with the replaced chip, which includes this focusing error, the standard deviation of the position measured was σ_z =16.4 µm. To determine if this error was problematic, we measured the temperature variation corresponding to z-axis translation between the laser and chip. For a 1,000 µm displacement, which exceeds the 750 µm chamber height, a temperature variation of only 0.5°C was measured, so the σ_z measured was deemed acceptable.

To measure the combined repeatability of the chip placement, laser z-axis translation to allow chip placement, laser power output, and thermocouple placement for calibration, we successively removed, replaced, and heated a water-filled chip and its thermocouple. Five consecutive temperature measurements showed a standard deviation of 0.1°C, well within tolerances for PCR from conventional instruments. We note that a contributing cause of the difference in temperatures between the trials is the result of variations in manual thermocouple placement, which was improved as we gained experience positioning the thermocouple tip.

3.1.3 Modulation

Controlling sample temperature during thermocycling required a method for modulating the infrared radiation. For a single sample or multiple samples all undergoing the same temperature profile, direct modulation of the laser output via an analog control voltage supplied to the laser driver is the most obvious choice and proved to be an effective method during early testing of our optical system. However, in order to achieve thermal multiplexing, one would either need a dedicated laser driver for each channel of the instrument, which would be extremely costly, or some method of independently modulating the beams incident on each reaction chamber.

For this modulation functionality, we considered several approaches to inserting

a component between the collimating optics and our microchip. The use of opto-electronics, specifically a liquid crystal-based optical shutter, offered the most elegant solution but high cost and issues of polarization-related baseline attenuation eliminated this option (further discussion of this concept can be found in Section 5.2.3). Instead, several mechanical solutions were considered. One early concept for enabling thermal multiplexing was the use of graduated neutral density filters, each with a dedicated positioner allowing for variable attenuation of the laser radiation during the annealing phase of thermocycling. The complexity of this method gave way to a simpler approach in which sufficiently fast-responding actuators could operate under PWM control to act as optical shutters. Early experiments made use of a solenoid array extracted from a dot matrix printer but eventually we implemented off-the-shelf miniature push type solenoids (Electro-Mechanisms, SP-25), with 8.9 mm stroke, as our optical shutters. Each solenoid was driven independently from a 12V power supply using MOSFETs triggered by 10 Hz pulse width modulated signals generated using LabVIEW and the digital outputs from our dat acquisition module. Power consumption of the two-channel modulation circuit was roughly 2 W. Modulation via shutter was compared to modulation via analog control voltages and revealed negligible difference in performance.

An important criteria for our modulation strategy was minimal temperature fluctuations during each step of the PCR reaction in order to operate within the tolerable envelope of temperatures for denature, annealing, and extension. As shown later in Figure 37, the biochemical processes involved in PCR can be forgiving to temperature accuracy, with some setpoints demanding higher accuracy than others. This observation has been made by other researchers, notably Carl Wittwer, one of the pioneers of rapid PCR thermocycling [165, 56].

We examined the frequency response of our system at a steady state temperature

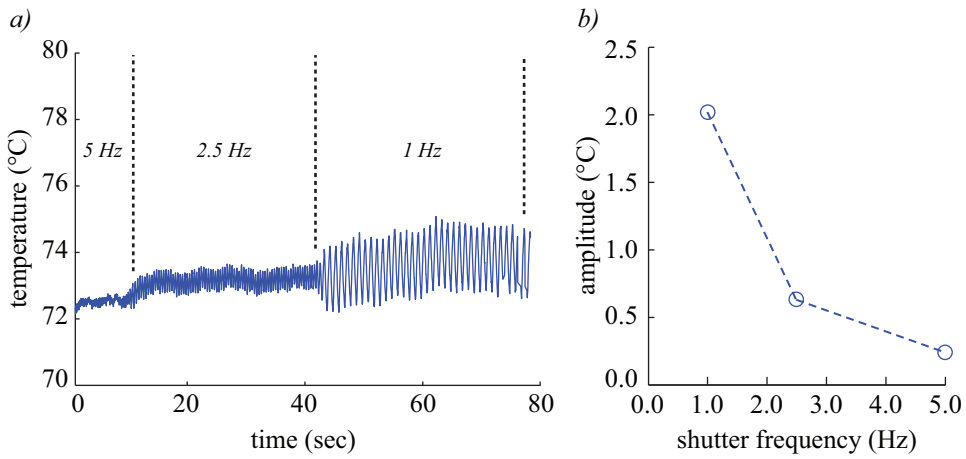

Figure 35: Frequency response of shutter modulation for a steady state temperature hold of around 73°C. The changing peak-to-peak fluctuation for shutter control frequencies of 5, 2.5, and 1 Hz can be seen from (a) the raw temperature signal and (b) a Bode plot of amplitude versus shutter frequency.

of around 73°C over a range of shutter control frequencies (5, 2.5, and 1 Hz) to determine a minimum modulation frequency for our mechanical shutters. The recorded temperature fluctuations, along with a linear Bode magnitude plot for mean peak-to-peak fluctuations, are shown in Figure 35. With a desired minimum fluctuation of less than 0.5°C, a frequency of 5 Hz proved sufficiently fast but we eventually chose to use 10 Hz, since we would achieve even less fluctuation and the required PWM signal was still of low enough frequency to be easily be reproduced with both hardware-timed and software-timed control systems.

As discussed in Section 2.1.3, we characterized the effect of shutter attenuation as a function of duty cycle on reaction chamber temperature by measuring chamber temperatures in our two-chamber microchip (with 40 mm chamber separation) while varying duty cycle through its full effective range (0.2–1.0) in 0.1 increments, shown here in Figure 36. This demonstration confirmed our ability to achieve any temperature potentially needed for a particular PCR protocol.

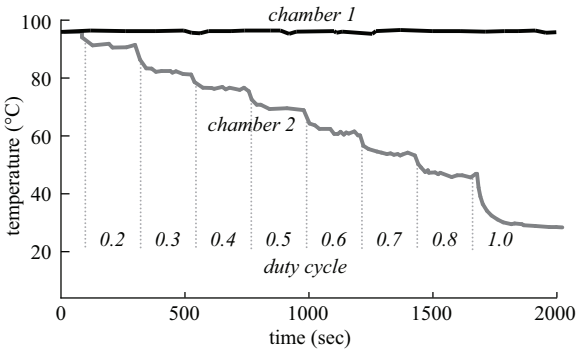

Figure 36: Effect of optical shutter attenuation was characterized during radiative heating of both reaction chambers of our microchip with 40 mm chamber separation. The shutter under chamber 2 was operated over its range of duty cycles in 0.1 increments. (Plot reproduced from Figure 9c.)

3.2 Temperature measurement

A critical requirement for controlling the temperature of our samples was the ability to accurately measure temperature. This was essential for both characterizing the system for open-loop operation and for feedback control when operating closed-loop. Although the localized nature of our heating method is one of the key features enabling thermal multiplexing, it presented a significant challenge to measuring the temperature of our 1 µL samples. Since most PCR thermocyclers operate by heating samples indirectly by first heating the surrounding environment (e.g., thermal block, air, thermally conductive microchip), simply measuring the heated environment can be used to drive the temperature control system without ever needing to directly probe the sample temperature. We did not have this convenience with our system.

Early attempts at temperature measurement made use of small diameter thermocouples inserted directly into the reaction chambers. This approach can give an estimation of the thermal behavior of the system but is confounded by absorption of laser radiation by the thermocouple tip. In addition, the metals that make up the thermocouple interfere with the PCR chemistry and inhibit the reaction [120]. An alternative

approach is non-contact temperature measurement, either with a microbolometer array (thermal camera) or fluorescence-based temperature measurement. The use of a thermal camera, which is discussed later in Section 3.2.2, could be a viable option but proved unreliable with our system in its current configuration. The use of hydrophilic temperature sensitive fluorescence dyes have been reported as effective for systems requiring a non-contact method of temperature measurement but accuracy is limited ($> 1°C$) and the system would require fluorescence monitoring [166, 77, 84]. Instead, the use of an embedded thermocouple proved to be the most reliable choice for temperature measurement, which will be described in detail in the next section.

Before fully developing our temperature measurement scheme, we performed a study of temperature tolerances for each setpoint to determine the demands of accuracy of PCR thermocycling. For this, we ran a series of herpesvirus reactions to detect Epstein-Barr virus (EBV) template DNA at 5 pg/µL (1.0×10^6 copies/µL) with varying temperature offsets. First, a set of nine reactions were run with temperature offsets of -3°C, +3°C, and +6°C applied individually to the three setpoints of denaturing, annealing, and extension. Then two reactions were run with offsets of +3°C, and +6°C applied to all setpoints. The results, shown in Figure 37, indicated the need for particularly accurate denaturing temperature holds and demonstrated the relatively greater flexibility of the annealing and extension temperatures. Hold times are similarly forgiving over a particular range, where the only quantitative input to determining durations applies to the extension times, since polymerase molecules exhibit known incorporation rates. Thus, while the task of assigning thermocycling parameters does not have a clearly optimal solution, studies such as this guided the heuristics we developed during the calibration and debugging of our temperature control system.

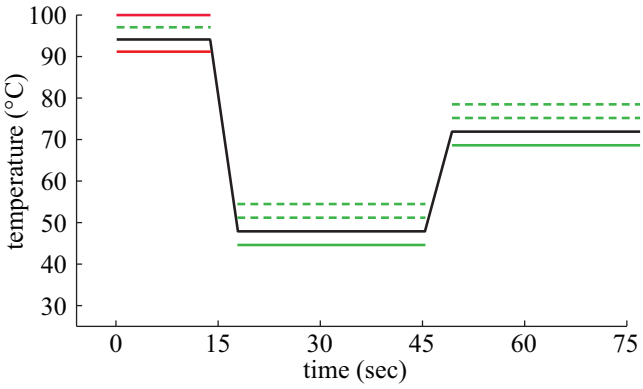

Figure 37: Experimental study of temperature tolerances for each PCR setpoint for EBV amplification. Green lines indicate successful amplification, red lines indicate failure, and the dashed lines indicate partially successful cases in which changing that setpoint alone was successful by the constant offset of that magnitude resulted in failure.

There were some notable limitations of this study. Temperature offsets were somewhat arbitrary and designed to only capture extremes of potential inaccuracies. Additionally, the use of purified viral DNA as the template prevented the observation of specificity-related issues, which would be notable in the presence of host DNA when operating at excessively low annealing temperatures. Still, this study confirmed the observation made in previous work that a "kinetic" paradigm for thermocycling, where biochemical activity occurs over ranges of temperatures, is more appropriate than the commonly excepted "equilibrium" paradigm, which assumes that the processes involved in PCR only at the precise temperature holds [167].

3.2.1 Thermocouple

Temperature feedback was provided by a custom T-type thermocouple (Physitemp Instruments, T-240C) with a diameter of 125 µm, wired to a linearizing circuit (Omega, TAC80B-T) that generated 1 mV/°C, and an instrument amplifier configured for a gain of approximately 10 to operate over the full range of the analog voltage input of our data acquisition module. Before being used with our instrument, each thermocouple was calibrated using a hot plate, 500 mL beaker of water, and multimeter

(Fluke, 179 True RMS Digital Multimeter) with a K-type thermocouple to provide the reference temperature. The water was heated through the range of temperatures required for PCR (40–100°C) while thermocouple voltages were recorded every 5°C, which was plotted against reference temperature to derive a calibration equation to be inserted into the LabVIEW control program for every experiment conducted with that particular thermocouple. Next, as described earlier in Section 2.2, the thermocouples were embedded within the microchip during the thermal bonding process, aligning the tip repeatably to the side of our reaction chambers, leaving a gap of approximately 500 µm. After removing the bonded microchip from the bonding fixture, a spot of hot-melt glue was applied at the point where the thermocouple exits the side of the microchip for the purpose of strain relief since thermocouple of such a small diameter are fragile and prone to fatigue if deformed repeatedly.

Since thermocouple tips were located near the reaction chambers and therefore did not directly measure reaction temperature, calibration was necessary to correlate the measured temperature with the reaction temperature. For this, a calibration microchip was fabricated with thermocouples bonded directly inside the reaction chambers in contact with the top wall of the chamber, furthest away from the laser source, as pictured in Figure 38a. At this location the measured temperature is close to the true reaction temperature, since theoretically <1% of the incident radiation reached the thermocouple to directly heat it. This fraction was determined from the Beer-Lambert Law where the transmitted power, P_T, was calulcated as $P_T(\lambda) = P_0(\lambda)(10^{-\alpha(\lambda)l})$, where $\alpha(\lambda)$ is the absorption coefficient of water at 1450 nm (30 cm^{-1}), l is the path length (750 µm), P_T is the transmitted power, and P_0 is the incident power.

In order to use the calibration microchip, the reaction chambers were filled with PCR buffer solution and the microchip was installed in the thermocycler. Starting with the laser turn-on voltage of 0.7 V, the steady state temperature in each chamber

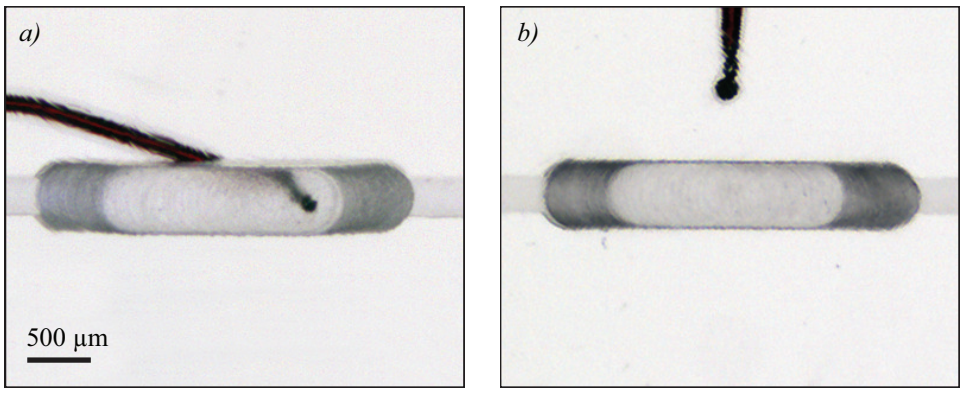

Figure 38: Calibration for our temperature measurement system required the fabrication of a special microchip with an embedded thermocouple in which the tip is positioned at the top of the chamber, opposite the side of the chamber where radiation is incident. Measurements from the in-chamber thermocouple, shown in (a), was used to establish a baseline relationship between reaction chamber temperature and the near-chamber temperature measured with our standard microchip, shown in (b).

was recorded as the voltage was increased to 1.4 V, where the temperature approaches the maximum required temperature of 94°C for denaturing. This was performed four times to obtain an average steady state chamber temperature as a function of laser driving voltage. Next, this process was repeated using the actual microchip used for PCR, with thermocouples bonded near the reaction chambers, pictured in Figure 38b. A calibration curve relating the estimated in-chamber temperature to near-chamber temperature between these microchips was then calculated. Since this calibration suffers from errors stemming from in-chamber temperature inaccuracies due to irradiation influence and alignment imperfections, it serves only as a baseline for further refinement. An array of calibration curves are generated by shifting the slope of the baseline fit and pivoting around the room temperature measurements, as shown in Figure 39. Each of these calibration relationships are then iteratively tested with a λ-phage amplification until PCR yield reached expected levels. Initial shifts to the slope are coarse changes of 5% but once a peak is detected, more refined iterations of 1% slope shifts around the successful amplification were used to further

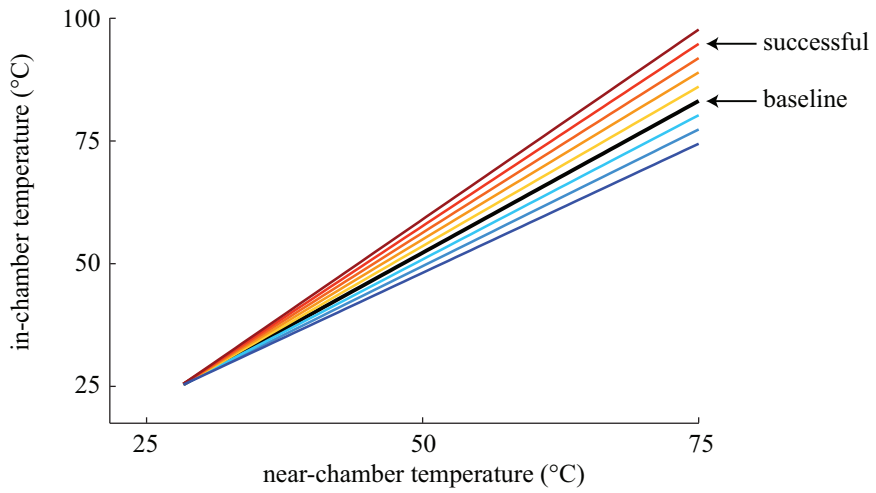

Figure 39: The calibration process for temperature feedback using a thermocouple embedded near the reaction chamber involved pivoting a baseline calibration (black) of in-chamber versus near-chamber temperature measurements around the common room temperature origin. Pivoting was performed by changing the slope to generate the shifted calibration curves (colored). Implementing each of these iteratively with a test reaction allowed us to empirically locate an accurate calibration curve.

refine the calibration. Temperature difference between the in-chamber and near-chamber measurement changed linearly over the calibrated range. Typical values for ΔT, defined as $T_{in-chamber}$-$T_{near-chamber}$, varied from around 10°C at a low in-chamber sample temperature of 50°C up to 25°C at a high sample temperature of 95°C. In addition to the need for calibration, there was concern regarding the inherent response lag resulting from the fact that the heated sample and sensor were not co-located, but this proved to be inconsequential for the time scales involved in our application.

During the course of testing our temperature measurement system, it was discovered that reaction chamber orientation affected temperature uniformity in the z-axis (i.e., across the thickness of the chamber). A microchip was fabricated with two embedded thermocouples, with the tips positioned at opposite ends of the reaction chamber along its depth (z-axis) and both to the side, out of the center of the laser focal spot to minimize temperature bias due to direct irradiation of the thermocouples. Next, the microchip was heated with a series of increasing laser power levels to

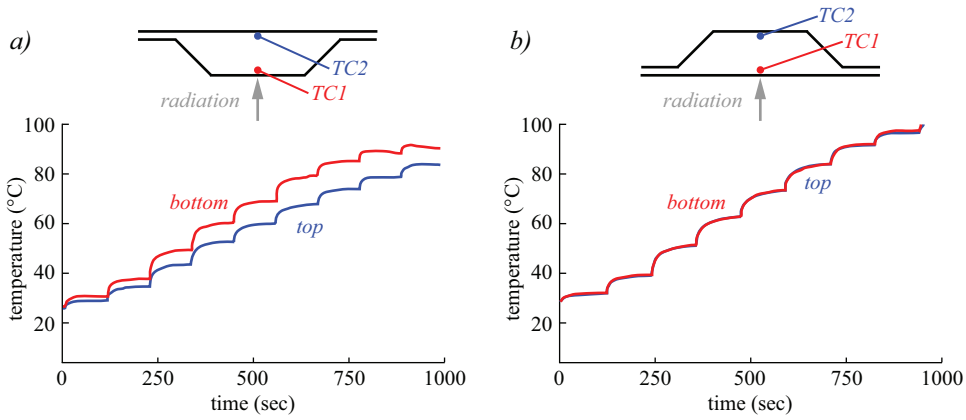

Figure 40: The influence of chamber orientation on temperature uniformity through the depth of the chamber was examined by inserting two thermocouples at each end of the chamber and performing laser-mediated heating in one orientation, then flipping the chip and repeating, over a series of steady state temperatures though the full operating range of our system. When heating from (a) the shorter side of the chamber, a gradient across the depth is observed while heating from (b) the longer side of the chamber results in no significant gradient.

show the relative thermocouple responses over the range of possible temperatures.

As shown in Figure 40, when radiation was incident on the side of the chamber with the shorter length, a significant temperature gradient was observed. When radiation was incident on the side of the chamber with the longer length, negligible gradient was observed. All proceeding experiments were conducted in the latter orientation (Figure 40b) for optimal temperature uniformity. Although the exact cause of this difference is unknown, it is suspected that internal reflections at the interface of the substrate and sample are a factor for the case in Figure 40a due to the non-normal incidence on the tapered regions.

3.2.2 Thermal camera

As an alternative to embedded thermocouples, a non-contact temperature feedback method was explored. Such an approach would allow for more straightforward scaling and simplify microchip fabrication without the need to manually embed sensors.

Towards this goal, we prototyped a single channel version of our laser-mediated thermocycler by adapting our optical system to accommodate a thermal camera (FLIR, A315), which was mounted above the microchip at an angle to prevent stray radiation from reaching the optics of the camera. The prototype, pictured in Figure 41, was built from the same core optical system used for our other configurations, including a 1450nm laser diode, a collimating lens mounted in a x-y translating cage plate, a solenoid shutter positioned to the side, and a pressure manifold to align the microchip to the optical cage system while delivering 40 psi to the reaction chamber. The thermal camera was rigidly mounted to an assembly of optomechanical components, including a rotation mount, post clamp, 1.5 in optical post, and translation stages (Thorlabs, RP01, C1501, P250/M, MT1/M), which allowed for precise and repeatable positioning of the camera above the microchip.

Analogous to the indirect temperature measurement scheme developed for our thermocouple system, the thermal camera was used to record the temperature over the region of interest just above the reaction chamber. These pixel values were averaged and then converted to sample temperature via the same calibration process used for the near-chamber thermocouple method. Specifically, a special calibration microchip with a thermocouple embedded in the top of the reaction chamber was used to first determine an approximate correlation between laser driving voltage and sample temperature. Then the same voltage values were used to heat the sample in a regular, sensor-less microchip while the temperature at the top surface of the microchip above the reaction chamber was recorded using the thermal camera. Iterative thermocycling runs with a series of calibration curves of different slope were finally used to identify the true relationship between the thermal camera measurement and the samples temperature.

Despite some promising results in which λ-phage DNA was occasionally successfully amplified (representative electropherogram shown in Figure 41), the thermal

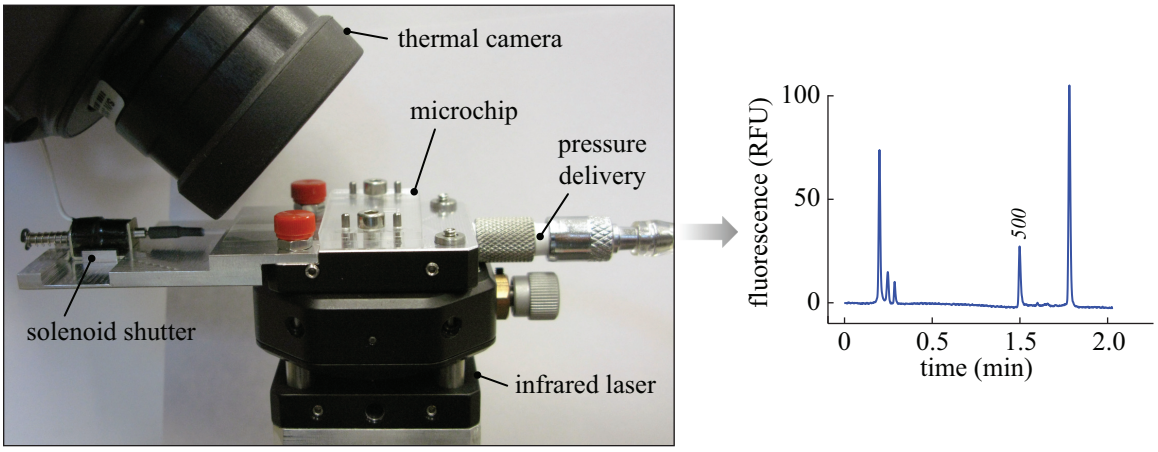

Figure 41: A thermal camera was implemented for non-contact temperature measurement to drive our laser-mediated thermocycling. The camera was mounted over a single-chamber, thermocouple-free microchip with the same core optical system underneath (*left*). Although unreliable in its current configuration, this system did prove to be potentially viable by successfully performing λ-phage amplification as shown in the electropherogram (*right*).

camera system ultimately proved to be unreliable. The system only worked intermittently, with the same calibration yielding positive results one day and negative results the following day. It is suspected that inconsistencies in the temperature at the top of the microchip due to the greater distance between the sample and the point of measurement as well as the influence of convective heat transfer explain the greater reliability of the thermocouple measurement system compared the the thermal camera.

3.3 Control system

The challenges of temperature measurement motivated the development of two control approaches: open-loop and closed-loop. Despite requiring rigorous characterization and specialized components for stabilizing the thermal environment of our system, open-loop control simplified operation of our instrument by obviating the need for sensors, providing a more plug-and-play experience. But for a more precise and flexible control scheme capable of dealing with system disturbances and more amenable to

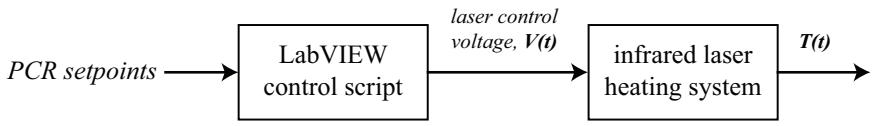

Figure 42: Block diagram for our open-loop system. Based on the setpoints required for a particular PCR reaction, a series of laser control voltages is generated and parsed via LabVIEW to drive our infrared laser and perform open-loop thermocycling.

scaling, closed-loop control was implemented for our two-channel system to demonstrate thermal multiplexing.

3.3.1 Open-loop

While the localized temperature control enabled by direct heating via infrared radiation provided efficient, distributable, controllable, and scalable delivery of energy to our 1 µL reaction volume, it presented the significant challenge of measuring the temperature of the sample volume, as described in Section 3.2. Therefore, in parallel with the development of a method for real-time temperature feedback, an open-loop system was devised to obviate the need for sensors and provide a simple, easy-to-use PCR platform. The basic operating principles involved using LabVIEW to parse a series of laser control voltage values to the laser controller, as shown in Figure 42. Through exhaustive system characterization and calibration, the laser control voltages generated the desired temperature profile for a particular PCR reaction.

Our open-loop instrument was built on the back of an initial effort towards developing an open-loop, microfluidic PCR system that we referred to as a "plug-and-play" instrument capable of amplifying λ-phage DNA in our 1 µL PMMA microchips in less than 10 minutes [118]. This first generation of our open-loop system was simple and easy-to-use, with a protocol similar to that of a conventional PCR instrument in that the user prepared the PCR reagents with standard protocols and simply loaded the sample into the microchip, installed the microchip in the instrument, ran the control program, and removed it following amplification, in contrast to virtually all

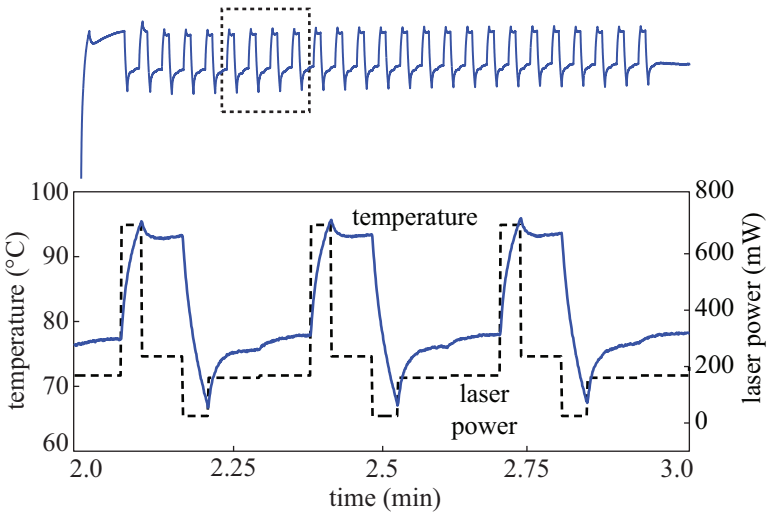

Figure 43: Early implementation of open-loop thermocycling for a single-chamber, 1µL microchip using a simple approach of fixed laser driving voltages for each PCR stage. Despite the non-optimal features of the resulting temperature profile, amplification of λ-phage was possible using 25 cycles in less than 10 minutes.

other reported microfluidic PCR instruments that require complicating features such as valves, pumps, and temperature sensors [168]. The PCR mixture utilized common reagent concentrations, including the relatively costly polymerase enzyme (0.02–0.025 U/µL), unlike most reported microfluidic PCR that require 2–20× more [68, 38, 69], an advantage we attribute to the effectiveness of our mineral oil loading passivation method [169].

Despite the speed and simplicity of our initial implementation of open-loop thermocycling, temperature accuracy and stability was not sufficient for amplifying more challenging and clinically-relevant genetic targets beyond our λ-phage test reaction. This was attributed to the rudimentary control voltage profile used for controlling laser power output and in turn sample temperature. This voltage profile consisted of three fixed voltages for each of the three PCR setpoints. Since this profile did not account for temperature dynamics during transitions and holds, the resulting temperature profile did not yield stable holds and exhibits undesirable features such as overshoot. A sample of this "plug-and-play" open-loop cycling is shown in Figure 43.

In order to improve upon the first generation open-loop instrument, we studied its shortcoming to identify sources of inconsistency (e.g., cycle-to-cycle temperature drift) and evolved the design to achieve the accuracy and reproducibility of amplification that is paramount for more challenging assays. More specifically, the redesign was aimed at performing quantitative, reverse transcription PCR to expand capabilities to include applications such as gene expression studies. Towards this end, the system was coupled to a microscope and substantial improvements were made to the thermal and mechanical stability.

The open-loop system, shown in Figure 44, consisted of an infrared laser system mounted on top of an environmental control fixture, which aligned and pressurized a single-chamber microchip and provided mechanical and thermal stability. This assembly was mounted on top of an inverted microscope (Nikon, TE2000) for applications requiring fluorescence detection. A xenon arc lamp (Sutter) filtered to 480/20 nm band-pass was used for the excitation. Emission was filtered (520/20 nm) and imaged with a CCD camera (Roper Scientific) after magnification with a 4×/0.2 NA objective (Nikon). To prevent stray infrared radiation from damaging the microscope optics, a disc-shaped water capsule was fabricated from three layers of 3 mm thick PMMA that was laser cut and bonded with marine adhesive, providing a 3 mm thick layer of water directly above the microscope objective and in-line with the optical path. This functioned like a hot mirror and absorbed any 1450 nm infrared radiation escaping past the microchip. Before every run of qPCR or qRT-PCR, the water bath, CCD camera, laser driver, and xenon arc lamp were powered on and allowed to warm up for 30 minutes.

The laser system was built using a 30 mm cage system with a 1450 nm, 600 mW infrared laser diode (Hi-Tech Optoelectronics, LMD-1450-600-33) powered using a constant current laser driver (Wavelength Electronics, WLD3343-3L). Modulation of laser output was accomplished using the analog voltage control feature of the driver.

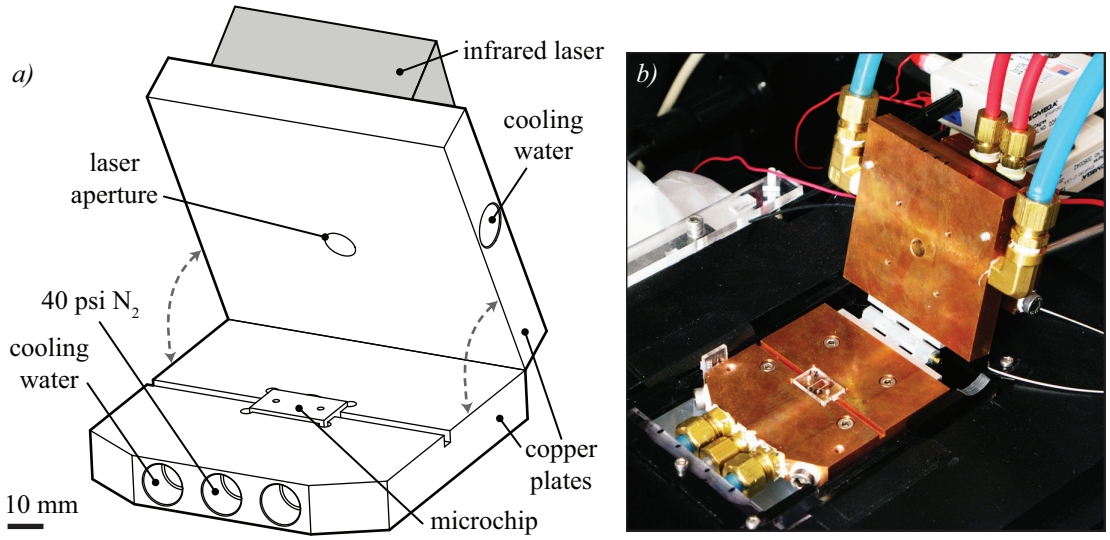

Figure 44: (a) Schematic and (b) photograph of our open-loop microfluidic PCR system used for qRT-PCR. The hinged environmental control fixture provided mechanical and thermal repeatability for the microchip and allowed simultaneous interfacing with an inverted microscope located below the fixture and an infrared laser heating system mounted on top of the fixture.

The laser was mounted in a cage plate designed to accommodate the geometry of the TO-3 packaging of the laser diode. Attached to this cage plate, opposite the diode, was a custom water-cooled tellurium copper heat sink for constant optical power output. Thermal compound (Arctic Silver) was used at the cage plate-heat sink interface for minimizing thermal resistance. An x-y translational cage plate (Thorlabs, CXY1) was used to position an aspheric lens (Thorlabs, A230TM-C) in the optical path to collimate the laser diode output.

The environmental control fixture was made up of two hinged 12.7 mm thick tellurium copper plates that were each machined square with dimensions of 80 mm $\times$ 80 mm. The base plate, into which the microchip is installed, featured a transverse water-cooling passage for controlling the microchip surface temperature and an air passage for providing 40 psi N_2 to the microchip ports to prevent the expansion of entrained air bubbles during PCR. For more details, refer to Section 2.3. In the bottom plate, pressurization ports designed to mate with the microchip fill ports were machined

with annular slots for miniature rubber O-rings to seal. A pocket in the center of the bottom plate designed for a close fit with the microchip ensured a completely enveloping thermal environment. Alignment pins press fit into the bottom plate enabled accurate and repeatable placement of the microchips in the fixture. To allow the microchip reaction chamber to be imaged for fluorescence detection, an 8 mm hole was drilled through the center of the bottom plate aligned with the center of the reaction chamber. The top plate, to which the laser system was attached with a 30 mm cage assembly, similarly featured a transverse water-cooling passage. To allow the microchip chamber to be heated by the laser system, another 8 mm hole was drilled, this time through the center of the top plate aligned with the center of the reaction chamber. Two thumbscrews located opposite the hinge were used to close the fixture, bringing the laser system into alignment with the microchip and preloading the microchip against the O-rings for proper pressurization.

The hinge used for the fixture (pictured in Figure 44b), which was a custom made butt-style five-knuckle hinge machined from aluminum and assembled with a steel pin and e-clips, exhibited a small amount of play due to the necessary gap between the knuckles of the hinge. This potential source of error was mitigated by designing the hinge to align the top and bottom plates when the top plate was pushed to the left during the closing of the fixture. Therefore, this routine was carried out for every experiment to ensure alignment. The water passages were pumped from a recirculating, temperature-controllable water bath set to 42.8°C, which imposed a microchip chamber temperature of 42°C, which was selected for maintaining an elevated microchip temperature to reduce the required laser power and, in cases of amplifying RNA, allowed for reverse transcription without the need for laser heating.

To assess the mechanical repeatability of the environmental control fixture, specifically the repeatability of microchip position, an empty microchip was installed in the fixture on the alignment pins, the fixture was closed and tightened, and the microchip

reaction chamber was imaged using the inverted microscope. A reference line was superimposed over the image and the distance between the chamber sidewall and the reference line was recorded. This measurement was repeated for ten microchips, each from a different fabrication batch, to determine the error of the positioning of the microchip chamber along the critical axis of the chamber width, which is most sensitive to misalignment due to the narrow laser beam focal spot. Results indicated that the combined processes of milling, bonding, and installing the microchip produced variation of 15 µm, corresponding to 3% of the microchip chamber width, in the critical axis of the chamber width.

To assess the repeatability of the hinge for positioning the laser over the microchip, the same toner-based burn paper method, described earlier and illustrated in Figure 34, was used for ten trials. Alignment between the focal spot and chamber was then evaluated qualitatively. To assess thermal stability, a water-filled microchip was placed in the fixture with the laser diode off or on as stated.

The environmental control fixture provided exceptional thermal stability. For the reverse transcription step with a setpoint of 42°C, with the laser diode off, we measured chamber temperature accuracy of 0.29°C (average difference from the setpoint), with precision (represented by the standard deviation) of 0.09°C.

We next evaluated the accuracy and precision of the system over the course of 20 consecutive cycles for both PCR and RT-PCR, representing one thermocycling run. Accuracy was computed as the difference between the setpoint and the measured average temperature and was calculated for each of the three setpoints (denaturing, annealing, and extension). For this calculation, the measured average temperature was defined as the average temperature during twenty 10 second intervals, consecutively, one per cycle. We then computed the precision, similarly, as the average of the measured temperature variation at each of the three setpoints. We define the measured temperature variation as the standard deviation of the temperature over

twenty 10 second intervals, consecutively, one per cycle. For PCR, the accuracy was 0.12°C, 0.82°C, 0.53°C and precision was 0.16°C, 0.18°C, 0.15°C for the denaturing, annealing, and extension steps, respectively. For RT-PCR, the accuracy was 0.59°C, 0.12°C, 0.02°C and precision was 0.21°C, 0.41°C, 0.25°C for the denaturing, annealing, and extension steps, respectively. This temperature stability is comparable to those reported by other conventional and microfluidic PCR systems. Conventional thermoelectric instruments (e.g., Bio-Rad MJ Mini) achieve temperature uniformity, or precision, of around 0.4°C. The Roche Light-Cycler reports temperature uniformity up to 0.15°C [170]. A microfluidic PCR system developed by Angione et al. reported temperature variations for the reverse transcription, annealing, and extension steps of 0.8°C, 0.1°C, and 1.3°C, respectively [68].

Lastly, we evaluated the run-to-run variability as a measure of repeatability. After computing the measured average temperature at each of the three setpoints for two separate runs, we took the pairwise difference between them and averaged these three differences (one per setpoint). The run-to-run variability for PCR was 0.12°C; for RT-PCR was 0.31°C.

In order to implement open-loop control, a calibration relationship between laser driving voltage and steady state aqueous solution temperature was necessary. A calibration microchip was fabricated with a 125 µm diameter thermocouple (Physitemp Instruments, T-240C) bonded into the reaction chamber with the tip positioned furthest from the laser, as shown in Figure 38a. The microchip chamber was filled with loaded with a 1 µL water sample and temperature was recorded during heating as the laser voltage was incrementally adjusted through its full range from laser turn-on to maximum power output. A simple linear regression was fit to the temperature measurements to generate an approximate temperature versus laser control voltage calibration curve. As described earlier for thermocouple feedback control, the in-chamber temperature measurement had to be bias corrected, which was carried

out empirically by adjusting the slope of the calibration curve and attempting our λ-phage reaction until successfully detecting a peak. Fine adjustment to the slope of the curve was performed until locating a relative maximum PCR yield, further refining the accuracy of the calibration.

Open-loop control of chamber temperature was accomplished by driving the laser with a discrete set of voltages without feedback. This voltage input is comprised of a series of segments determined uniquely for each temperature transition and subsequent temperature hold: ambient to denaturing, denaturing to annealing, annealing to extension, extension to denaturing, or more generally T_n to T_{n+1}. To determine each segment, we used the known calibration relationship between laser driving voltage, V, and steady state chamber temperature, T, in the following procedure. The laser was driven at V_n corresponding to T_n for 2 minutes to reach steady state using the calibration microchip in the instrument. V_n was step changed to V_{n+1} corresponding to T_{n+1} for 2 minutes, again to reach steady state. The temperature $T(t)$ was recorded from the time of the step change for the 2 minute duration.

The measured temperature, $T(t)$, was converted to voltages, $V(t)$, using the calibration relationship. For $V_2 > V_1$ (heating), we computed $V_r(t) = 2V_{max} - V(t)$, where V_{max} is the maximum value of $V(t)$, to reflect $V(t)$ about V_{max}. For $V_r(t) > V_{high}$, where V_{high} is the highest voltage that can be safely used for the laser, we set $V_r(t) = V_{high}$. Similarly, for $V_2 < V_1$ (cooling), we computed $V_r(t) = 2V_{min} - V(t)$, where V_{min} is the minimum value of $V(t)$, to reflect $V(t)$ about V_{min}. For $V_r(t) < V_{low}$, where V_{low} is the laser turn-on voltage, we set $V_r(t) = V_{low}$. $V_r(t)$ therefore consists of a constant phase of duration t_c followed by a quasi-exponential phase corresponding to the heating and cooling dynamics of the microchip, approximately a first-order dynamic thermal system. $V_r(t)$ has a 2 minute domain. Next $V_r(t)$ is truncated to the duration of $t_c + t_h$, where t_h is the desired hold time for the PCR reaction step. Lastly, the segments are concatenated for the initial denaturing phase and desired number

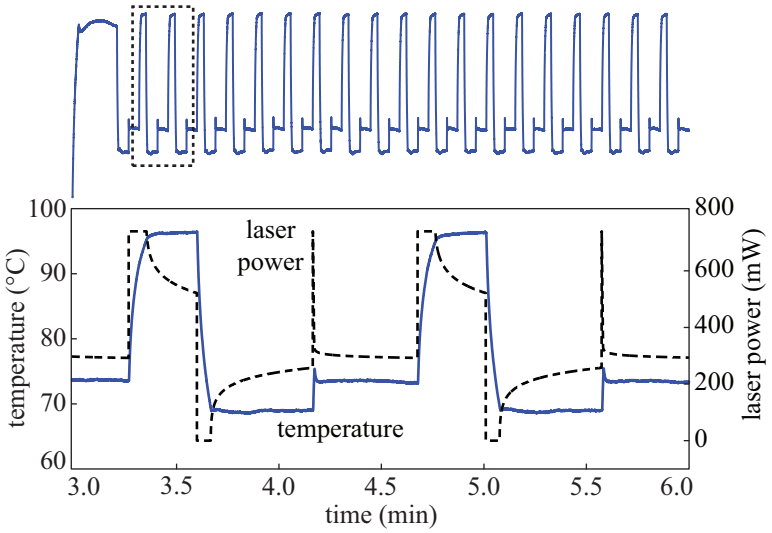

Figure 45: Open-loop thermocycling was accomplished using a laser power profile (dashed) to generate the desired profile of reaction chamber temperatures (solid). The temperature profile was determined from a calibration between laser driving voltage, laser output power, and chamber temperature, along with characterization of temperature dynamics during temperature transitions and holds. This thermocycling was used to perform qPCR for a 500 bp amplicon of λ-phage DNA for 30 cycles, with a 1 minute initial denaturation for the first cycle and all subsequent cycles consisting of 93°C for 10 seconds, 68°C for 20 seconds, and 72°C for 20 seconds.

of cycles as required for PCR. This methodology results in a piecewise continuous function, or open-loop laser power profile, consisting of (1) exponentially rising or decaying voltages for temperature holds and (2) maximally on or off voltages for heating or cooling transitions, respectively. The resulting voltage and temperature profiles are shown in Figure 45. The chamber temperature rapidly and repeatably reaches each stable hold phase with minimal overshoot.

Efficiency, sensitivity, specificity, accuracy and reproducibility are all important factors when comparing a novel PCR assay to traditional laboratory equipment [171]. To evaluate the system, real-time amplifications of both DNA and RNA were performed as shown in Figure 46.

For demonstrating real-time DNA amplification (qPCR), a 500 bp amplicon of λ-phage DNA (Affymetrix) was targeted with the primer set listed in Appendix B. An intercalating dye (Lonza, SYBR Green I) was used for real-time detection. Reactions were prepared from a commercial PCR master mix according to the protocol listed in Appendix A to produce 5 µL reaction mix aliquots from which 1 µL samples were loaded into our microchips using the mineral oil technique described in Section 2.4.3.1. The system was tested with a range of λ-phage DNA template (10^5–10^7 starting copies). (Note: BSA was also included for dynamic passivation since these experiments were performed before discovering the minor detrimental effects of BSA when paired with our mineral oil loading technique.) Loaded microchips were installed in the open-loop fixture and a total of 30 cycles were then performed with a 1 minute initial denaturation for the first cycle and all subsequent cycles consisted of 93°C for 10 seconds, 68°C for 20 seconds, and 72°C for 20 seconds.

For real-time amplification of RNA (qRT-PCR), a 100 base segment of the RNA transcript from the mouse glyceraldehyde 3-phosphate dehydrogenase (GAPDH) housekeeping gene was chosen as the target using the primer set listed in Appendix B. GAPDH was chosen for its consistent expression during stem cell differentiation as a

control for thermocycler validation. 5.45 ng of total RNA was extracted from mouse embryonic stem cell culture lysate, as quantified using a spectrophotometer (Thermo Scientific, NanoDrop 2000). The protocol provided in Appendix A allowed for the preparation of reaction mixes capable of "single tube" reverse transcription and PCR. The same SYBR Green I dye used for the λ-phage qPCR was used for this experiment.

The oil loading technique was used to load 1 µL sample volumes into our microchips. The microchips were then installed in the fixture at 42°C for 30 minutes with the laser off to allow the reverse transcription to occur prior to thermocycling. A total of 30 cycles were performed, with a 1 minute denaturation for the first cycle to inactivate the reverse transcriptase and denature the cDNA and all subsequent cycles consisted of 93°C for 10 seconds, 56°C for 20 seconds, and 72°C for 20 seconds.

For both qPCR and qRT-PCR detection, fluorescence images were collected during the extension phase of every cycle using NIS Elements BR software and post-processed via MATLAB. To avoid photobleaching of the SYBR Green dye, exposure time was limited to 2 seconds and images were taken 17 seconds into each extension hold time. The image processing algorithm computed a normalized series of average intensities over a constant region of interest on the microchip, indexed by cycle number. All values below the initial intensity level were set to zero. For qRT-PCR detection, a median filter was applied to smooth fluorescence intensity traces.

For qPCR of λ-phage DNA, three template concentrations ranging from 10^5-10^7 starting copies (n=3) were amplified to evaluate repeatability and efficiency with known starting template concentrations, providing a standard curve (Figure 46a). The cycle number threshold, C_T, was set as the cycle number at which the measured fluorescence crosses a threshold of 30σ, where σ is the standard deviation of the fluorescence intensity for the first six PCR cycles. The logarithms of the λ-phage DNA starting copy numbers were plotted against cycle threshold values, and a linear regression fit was performed. The coefficient of determination, R^2, from this regression

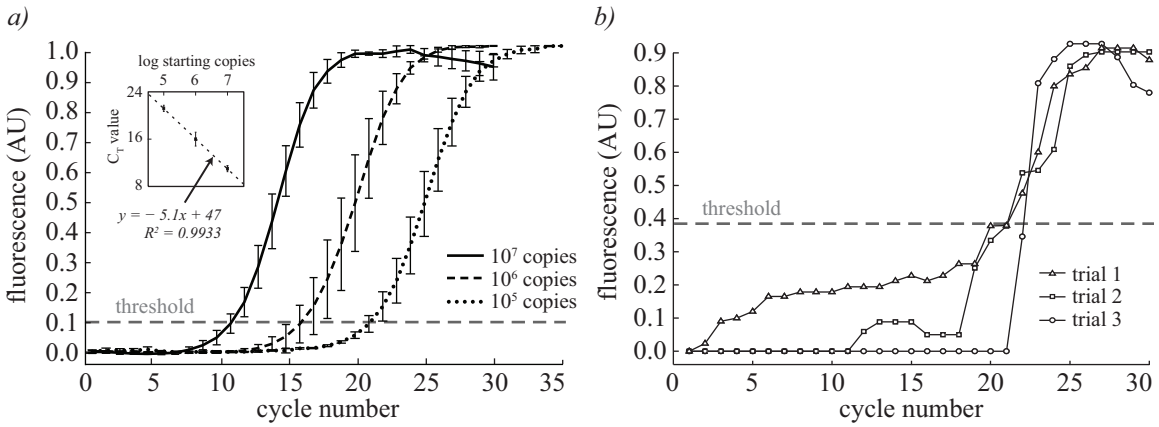

Figure 46: Fluorescence intensity vs. cycle number for qPCR and qRT-PCR. (a) PCR of λ-phage DNA with varying starting copies showing accurate exponential amplification of serial dilutions. The inset shows C_T vs. log starting copy number, used to determine amplification efficiency. Each data point represents the average of three replicates, with error bars corresponding to one standard deviation. (b) RT-PCR of GAPDH RNA transcript for three trials showing repeatable cycle number threshold for amplification. PCR λ-phage DNA required 35 minutes for 30 cycles; RT-PCR of GAPDH required 65 minutes when accounting for the initial 30 minutes for reverse transcription.

analysis was 0.9933. The standard deviations of these cycle threshold values were computed as 0.5, 1.2, and 0.5 cycles for 10^5, 10^6, and 10^7 starting copies, respectively, indicating good repeatability. Total runtime was 35 minutes for 30 cycles.

The efficiency, E, of the system was calculated from the slope of the standard curve ($k = -5.1$) and found to be $E = 100(10 - 1/k - 1) = 57\%$. Conventional PCR systems typically achieve 65–90% [172, 173], and microfluidic PCR systems typically report lower efficiencies [174, 54]. This is due primarily to high surface-area-to-volume-ratio and the resulting adverse surface interactions, as was explored in Section 2.4. Our efficiency is somewhat lower than conventional systems, perhaps due to non-optimal reagent concentrations, cycle hold times, or temperatures, but amplification was obtained consistently for both DNA and RNA.

For qRT-PCR of GAPDH RNA transcripts, the amplification process was repeated three times to evaluate repeatability (Figure 46b). The cycle number threshold, C_T, was set to 10σ. The repeatability of the qRT-PCR was measured by calculating

the standard deviation of the C_T values and found to be 1.0 cycle. Total runtime, including the initial 30 minutes allotted for reverse transription and 30 cycles of thermocycling, was 65 minutes.

The average heating and cooling rates of the system were 3.3°C/sec and 3.86°C/sec, respectively. Conventional thermoelectric thermocyclers (e.g., Bio-Rad MJ Mini) operate with heating and cooling rates of 3.3°C/sec and 2.0°C/sec while the Roche Light-Cycler qPCR instrument reports heating and cooling rates of 3.3°C/sec and 3.0°C/sec [170]. One recent microfluidic qPCR system, by Angione et al., reported heating and cooling rates of 1.6°C/sec and 1.8°C/sec [68]. A more rapid microfluidic qPCR capable system [175], reports achieving 30 cycles in 26 minutes (rates were not reported) as compared to our 30 cycles in 35 minutes, and Kim et al. achieve 40 cycles in 6 minutes [84].

Comparatively, of the thermocyclers capable of qPCR, our system is faster than conventional real-time thermocyclers and most microfluidic counterparts. The speed is comparable to the Roche Light-cycler, but with smaller volumes (1 µL vs. 10–50 µL) and potential for integration of multiple pre- and post-PCR steps as others have done [39, 176]. Compared to faster microfluidic qPCR systems [84, 175], our system is capable of qRT-PCR in addition to qPCR, uses disposable polymer microchips, and is easy to use. Although we have previously used a version of this system to perform faster PCR (e.g., 10 minutes/analysis), this design exhibits slower cooling rates due to the environmental control fixture and therefore longer analysis time.

Control reactions were performed with 5 µL samples volumes, each covered with 15 µL of mineral oil to prevent in-tube evaporation, using a conventional, Peltier-based thermocycler (Bio-Rad, MJ Mini). The λ-phage DNA amplification underwent 40 cycles of thermocycling with a 5 minute, 95°C initial denaturation step at the beginning of cycling and each subsequent cycle consisted of 95°C for 30 seconds, 68°C for 60 seconds, and 72°C for 60 seconds. The last cycle included a 2 minute,

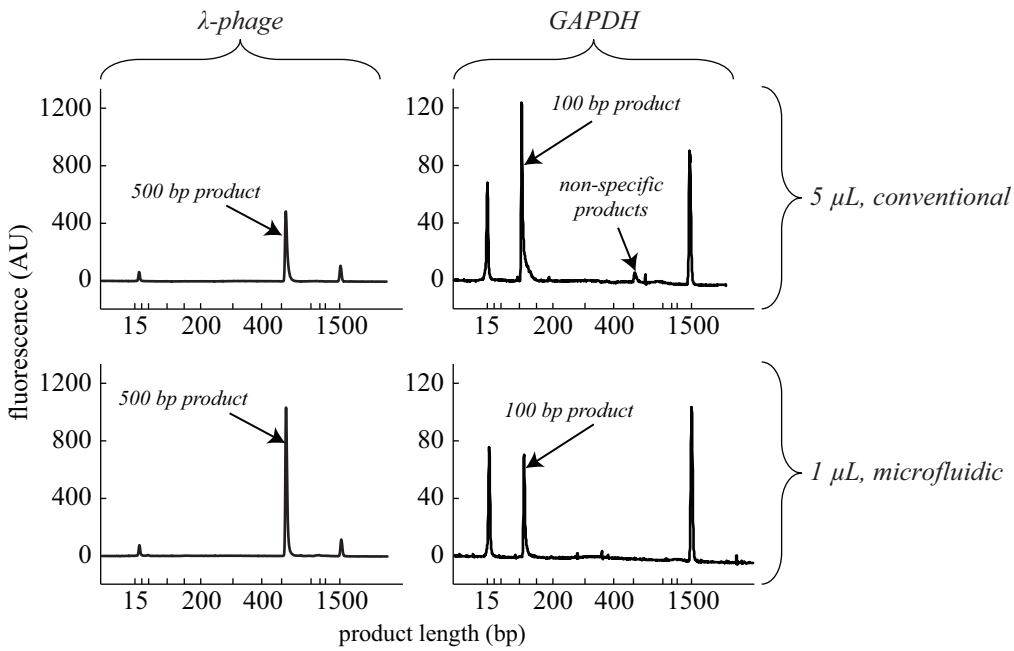

Figure 47: Representative electropherograms of PCR of λ-phage DNA (left column) and RT-PCR of GAPDH RNA transcript (right column) amplification products using both a conventional thermocycler with 5 µL volume (top row) and open-loop laser-mediated thermocycler with 1 µL volume (bottom row). The microfluidic PCR system shows comparable yield and improved specificity. Outer peaks correspond to sizing and quantification markers (15 bp, 1500 bp).

72°C final extension. The control amplification of the GAPDH RNA transcript began with a temperature hold at 42°C for 60 minutes for the reverse transcription process followed by 40 cycles of thermocycling with a 5 minute, 94°C initial denaturation step then subsequent cycles of 94°C for 10 seconds, 56°C for 30 seconds, and 72°C for 30 seconds.

End-point detection was used to confirm amplifications for every reaction run on the open-loop system. Additionally, the PCR and RT-PCR yields and specificity achieved by the laser thermocycler and conventional thermocycler were compared. Eletrophoretic detection was performed using the Agilent 2100 Bioanalyzer. The resulting electropherograms for each case are shown in Figure 47, which include sizing and quantification markers at 15 bp and 1500 bp. Yields from PCR were not statistically different ($p>0.1$), nor were yields from RT-PCR ($p>0.1$).

Regarding specificity, the electropherogram in Figure 47 indicate that the formation of non-specific PCR products was reduced with the open-loop laser thermocycler. In contrast to other reports suggesting the presence of non-specific products during microfluidic qPCR [175], we did not observe this. The laser thermocycler yields slightly improved performance of qRT-PCR as compared to a conventional thermocycler.

The combination of our disposable microchip and environmental control fixture yielded a real-time (RT-)PCR platform with the time and cost-saving benefits of microfluidics without the complex fabrication and operation involved with most microfluidic devices. This easy-to-use platform could be a valuable tool for real-time monitoring and control for applications in emerging fields such as stem cell biomanufacturing [177], where gene expression is tracked over time cell populations and expression levels change from environmental stimuli in minutes to hours [32, 46], or during differentiation from hours to days. Still, this open-loop instrument is not capable of analyzing multiple targets simultaneously nor can is operate with the volume handling and sensitivity required for applications such as single cell gene expression measurement. For scaling to larger numbers of targets and improving speed and reaction performance, the precision of closed-loop must be harnessed.

3.3.2 Closed-loop

Despite the ease-of-use and compatibility with real-time fluorescence monitoring offered by the open-loop system, the need to perform PCR on multiple unique genetic targets, as commonly required in molecular biology laboratories, demanded a more scalable and precise method of temperature control. The limits of empirical thermal characterization and the slow ramping resulting from the use of the environmental control fixture, especially during the cooling transitions, prevented the implementation of open-loop control for a platform accommodating multiple samples with

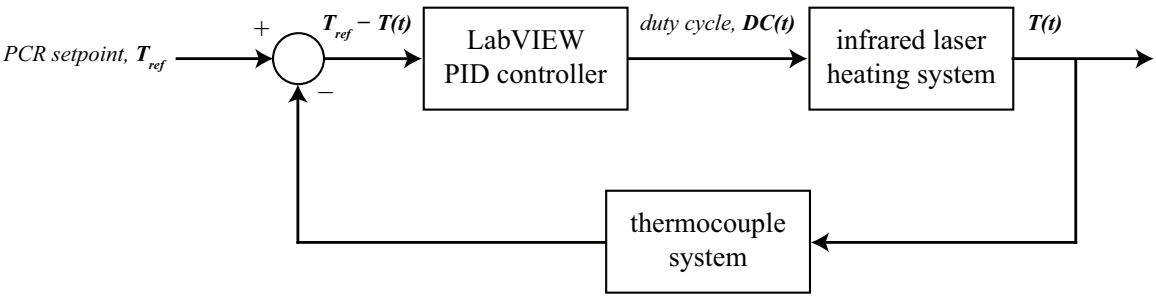

Figure 48: Block diagram for our closed-loop system. Temperature feedback from our thermocouple system provides inputs to a PID control in LabVIEW for determining the duty cycle for our shutter modulation system to achieve closed-loop thermocycling.

independently-controlled temperatures. In addition, we sought to increase throughput by not only focusing on a greater number of samples but also a greater number of target with a new mode of operation we developed called "thermal multiplexing" in which multiple reactions, each with its own unique annealing temperature, are run in parallel by modulating radiation via mechanical solenoids. This concept was introduced in Section 1.5 and depicted in Figure 1. Implementing this more complex heating mode with an open-loop system would require characterization of both steady state and transient behavior of the system for a variety of desired temperature profiles, a prohibitively tedious process.

In order to operate with more precise and multiplexed temperature control, closed-loop control was required. We implemented this scheme for scaling from a single-chamber to a two-chamber design. As described in Section 3.2.1, an embedded thermocouple located near our reaction chamber for indirect probing of sample temperature was selected as the preferred method for feedback. A basic scheme was devised in which, for each step in the thermocycling program, measured temperature, $T(t)$, was compared to the PCR setpoint, T_{ref}, and the error, $|T_{ref} - T(t)|$, was passed to a PID controller, which output corresponding duty cycle values, $DC(t)$, to optical shutters to modulate the radiation delivered from the infrared lasers (operating at a fixed optical power output) to the reaction chambers. This basic scheme is shown in

block diagram form in Figure 48.

We implemented this closed-loop control scheme with thermal multiplexing using infrared laser radiation as the heat source for n=2 chambers per microchip and using mechanical solenoids as attenuators, as shown in Figure 49. Many of the same components used for the open-loop system were used for the closed-loop system. Specifically, infrared radiation was supplied by a pair of 1450 nm, 600 mW laser diodes (Hi-Tech Optoelectronics, LMD-1450-600-33) wired in series and powered by a single constant current laser driver (Wavelength Electronics, PLD5K-CH) for common control and uniform optical power output. Miniature solenoids, described in Section 3.1.3, were used as optical shutters and were driven independently using 10 Hz pulse width modulated signals generating using digital outputs from a 16-bit data acquisition module (National Instruments, USB-6221 BNC). The laser diodes were mounted on aluminum heat sinks with axial cooling fans to prevent overheating and to maintain constant optical power output. As detailed in Section 3.1.2, all components were assembled and aligned with a 30 mm cage system. Collimating lenses were installed in x-y translational mounts to provide fine adjustment of the focus and position of the infrared beam. The two-chamber microchip was installed in the optical system by first mounting it to the pressure manifold (Section 2.3), which featured alignment pins for repeatable positioning, 1 mm thick, laser cut silicon gaskets for sealing, and luer connections for delivering 40 psi N_2 from a supply tank to the microchip fill ports to prevent the expansion of entrained air bubbles during the near-boiling temperatures used for PCR. This pressure manifold/microchip assembly was then aligned to the laser system using the construction rods of the cage system.

Temperature was measured using two 125 µm diameter thermocouples (Physitemp Instruments, T-240C), which are embedded in the microchip and calibrated for indirect measurement of reaction chamber temperature, as detailed in Section 3.2.1.

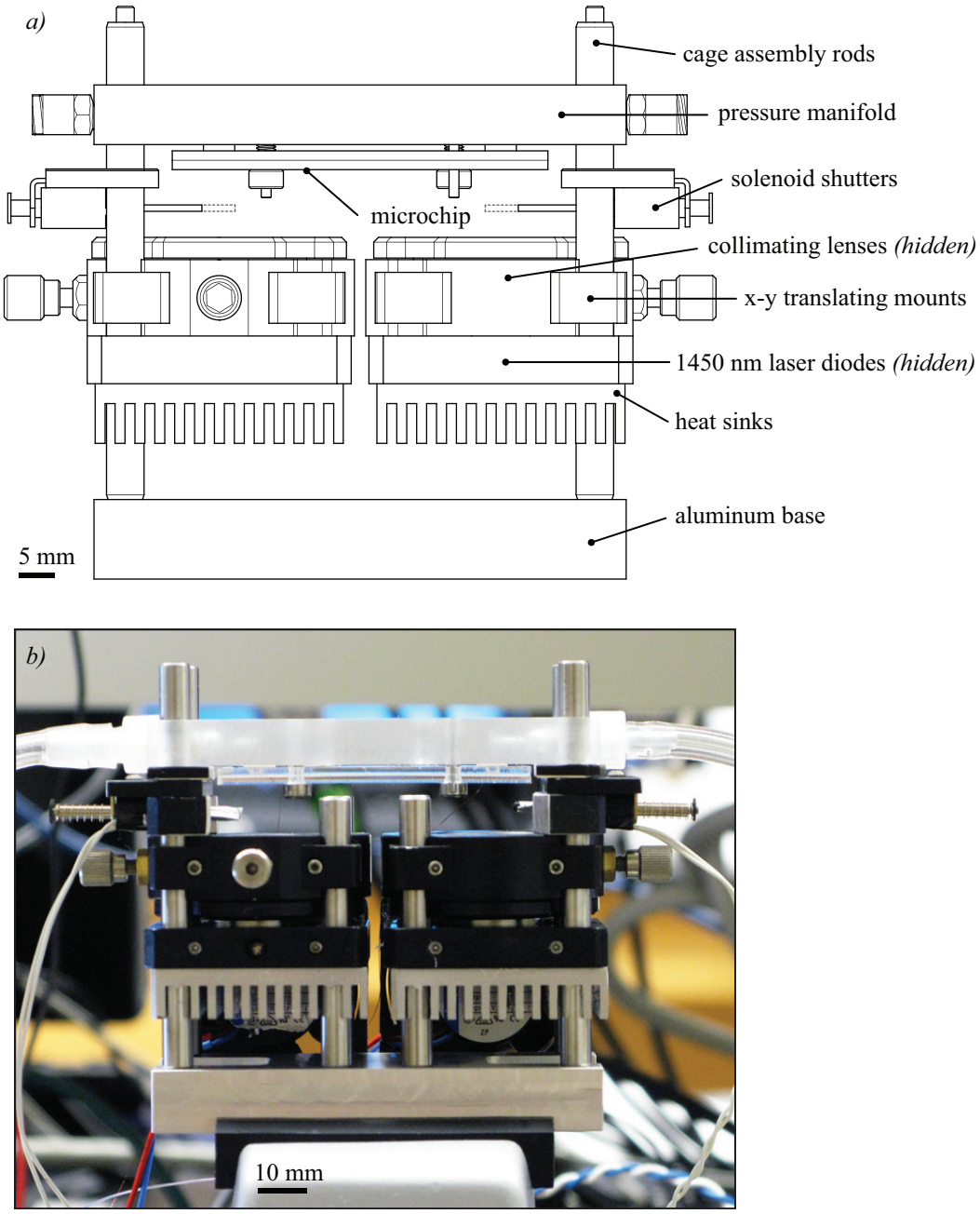

Figure 49: (a) Schematic and (b) photograph of our closed-loop infrared laser thermocycler consisted of two infrared laser sources controlled via a common power supply, two solenoid shutters, and a PMMA microchip featuring two 1 µL reaction chambers, each with a pair of 700 µm diameter fill ports for sample loading and pressurization at 40 psi via a pressure manifold. Two thermocouples (not shown) are bonded between the layers of the microchip with the tips located within 1 mm of the reaction chambers and calibrated for closed-loop temperature control.

Accompanying electronics linearized and amplified the thermocouple voltage for measurement using analog inputs of our data acquisition module. This was the most crucial component in achieving successful closed-loop control. With proper thermocouple positioning and calibration, we achieved reliable feedback control.

A LabVIEW program was developed to control our closed-loop system. The block diagrams for the main program and the subroutine controlling the progression of each cycle are shown in Figure 50. The user interface allowed the input of the desired temperature setpoints and hold times for each stage of PCR (initial denaturing, denaturing, annealing, extension, and final extension) for each of the two reactions as well as the total number of cycles. Additionally, the interface featured an input field for setting a filename to which the time, temperature, and shutter duty cycle data was stored. The main program, shown in Figure 50a, is a 3-pane sequence in which the first pane collected and passed input data to the second pane, which powered on the lasers and executed the cycling subroutine while storing time, temperature, and duty cycle data in real time. Finally, the arrays of data are passed to the third pane where they are stored to a text file.

The core of the programming is the cycling subroutine, which reflected the control scheme shown in Figure 48. The basic flow of this subroutine, shown in Figure 50b, can be summarized as follows: 1) The current stage of PCR (initial denaturing, denaturing, annealing, extension, or final extension) was determined based on binary values representing each of the five stages; 2) Temperature measurements of each chamber were compared to the relevant setpoints for that stage to determine the current error, $|T_{ref} - T(t)|$; 2) Depending on the error, the shutter duty cycle was determined, with 0.0 for heating, 1.0 for cooling, and a value generated by a PID controller for holding the reaction chamber temperatures at the commanded setpoints; 3) An array for each chamber containing three values (T_{ref}, error, and duty cycle) was sent via global variable to an external program that commanded the shutter to

a)

b)

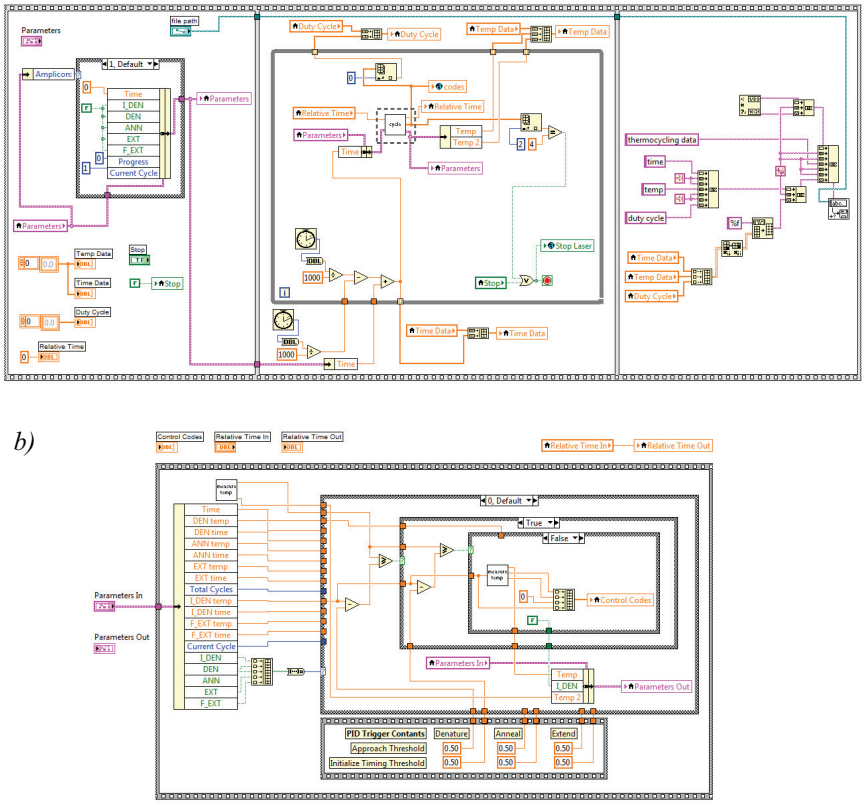

Figure 50: LabVIEW was used to implement our PID control system. (a) The main program passes inputs for thermocycling conditions, including temperature setpoints, hold times, and total cycle number, to the (b) cycling loop that measures temperature, uses the PID controller to determine appropriate duty cycles for the shutter control signal, and keeps track of thermocycling progress through its repeated stages.

open for heating, close for cooling, or oscillate via 10 Hz PWM signal. At the end of each temperature hold, the binary values for the PCR stages were updated and the program proceeded to the next stage, with cycle number being updated after each extension step until all cycles had been executed, at which point the lasers were powered off, data was stored, and the program was terminated.

As a proof of concept for thermal multiplexing, we used two unique PCR reactions with relatively high and low annealing temperatures. The high temperature reaction targets a 500 bp amplicon from λ-phage DNA with a 68°C annealing temperature, while the low temperature reaction targets a 600 bp amplicon from Epstein-Barr virus (EBV) DNA with a 48°C annealing temperature [15].

λ-phage and EBV reaction mixes were prepared according to the protocols described in Appendix A, dividing the mixes into 5 µL aliquots. Using our mineral oil loading technique, described in Section 2.4.3.1, 1 µL samples of each target were loaded into our two-chamber microchips.

To demonstrate the importance of annealing temperature on final product concentration, the reactions were thermocycled with four sets of conditions: low annealing temperature (48°C), high annealing temperature (68°C), average annealing temperature (58°C), and ideal annealing temperatures by thermal multiplexing (λ-phage at 68°C and EBV at 48°C). A total of 40 cycles were performed, with a 1 minute initial denaturation for the first cycle and all subsequent cycles consisted of denaturing at 94°C for 10 seconds, annealing for 20 seconds, and extension at 72°C for 20 seconds, as well as a final extension step of 3 minutes. Electrophoretic detection of the PCR products was performed on an Agilent Bioanalyzer, using the DNA 1000 kit that includes sizing and quantification markers at 15 bp and 1500 bp.

In order to simultaneously perform the λ-phage and EBV amplifications, two distinct thermocycling profiles were generated, as shown in Figure 51. Total runtime was roughly 110 minutes to complete 40 cycles. The average cycle duration was 155

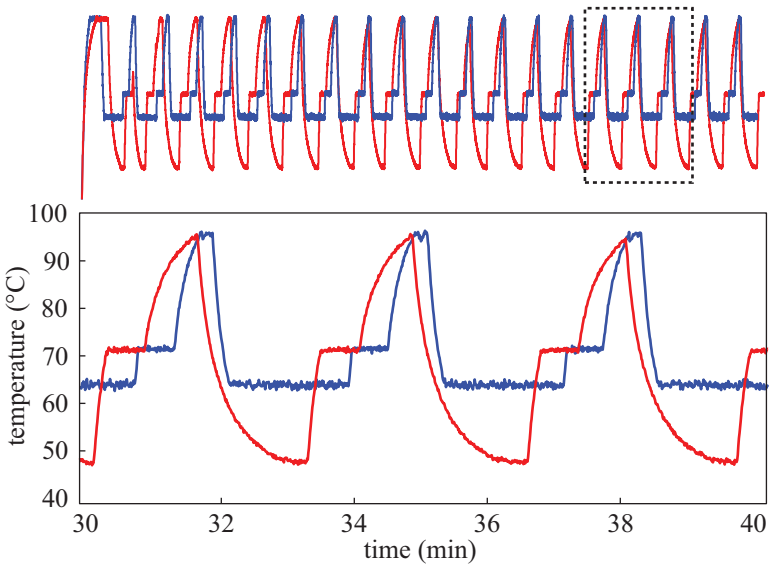

Figure 51: Independent temperature profiles for λ-phage and EBV amplifications were generated simultaneously with distinct annealing temperatures of 48°C and 68°C. This system utilized closed-loop control via thermocouples feedback and shutter-based optical modulation of infrared laser radiation in 1 µL reaction chambers on a polymer microchip.

sec with average heating rates of 2.54°C/sec and cooling rates of 2.53°C/sec (n=5). Although this is not a significant improvement over conventional thermocycler speeds, the system was run with conservative hold times and without extensive optimization. Additionally, this demonstration represents an extreme case of reactions with different annealing temperatures and therefore required longer transitions than would be expected for more common sets of reactions with a narrower range of temperatures. Regarding thermal accuracy and repeatability, we measured temperate accuracy as compared to the setpoint within 0.64°C (average absolute difference over three consecutive cycles) and standard deviation around the setpoint of 0.46°C, both insensitive within the tested range of 48-94°C.

A representative set of electropherograms for the microchip-based λ-phage and EBV amplifications can be seen in Figure 52. When both reactions were run with the low annealing temperature of 48°C, ideal for EBV, the λ-phage reaction failed while EBV was easily detected. When both reactions were run with the high annealing

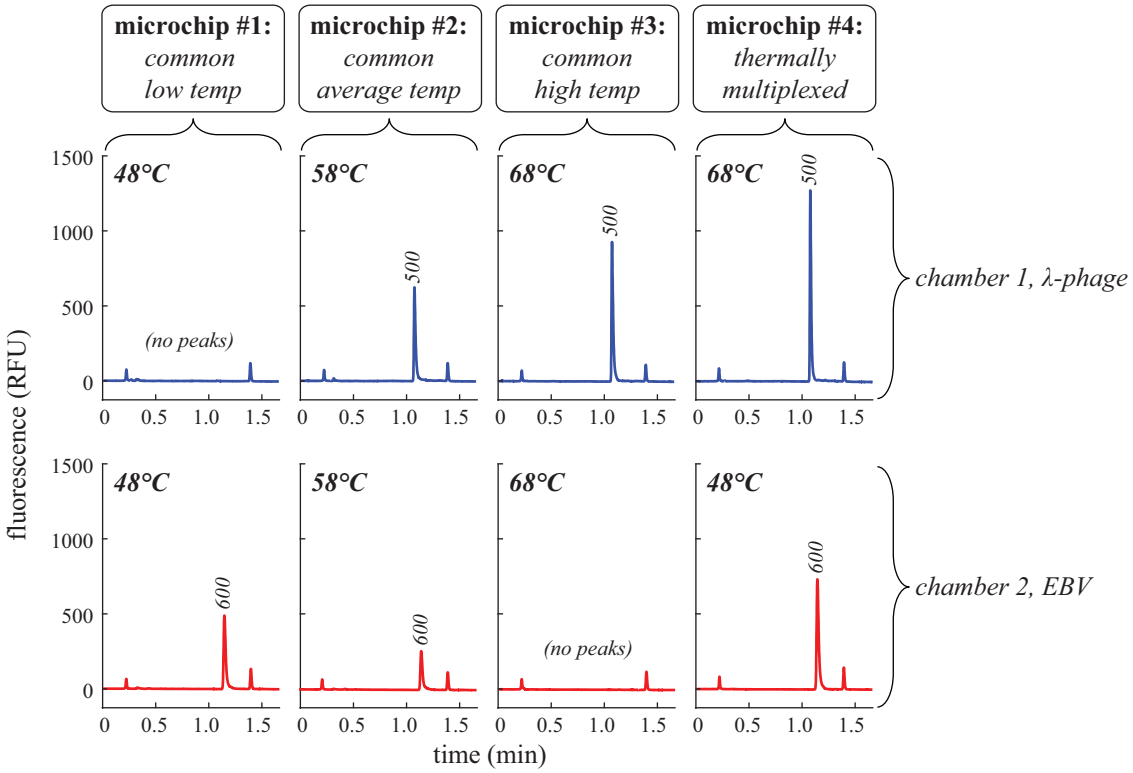

Figure 52: Electropherograms show the PCR products for λ-phage (top row) and EBV (bottom row) amplifications run in parallel using four different thermocycling runs (represented by each column). From left to right, annealing temperature was uniform across the two reaction chambers (1 µL each, 40 mm separation) at low and high values, the average of the high and low, and then thermally multiplexed to maintain the ideal temperatures for each reaction. Small peaks correspond to sizing and quantification markers (15 bp, 1500 bp).

temperature of 68°C, ideal for λ-phage, the EBV reaction failed while λ-phage was easily detected. For the condition of thermal multiplexing, where each reaction was run with its ideal annealing temperature, both products were easily detected. An expanded data set for demonstrating thermally multiplexed virus detection is presented in Section 4.3.

Such results indicate the importance of operating at ideal reaction conditions. In cases where primer design is inflexible to annealing temperature considerations and biochemical multiplexing is infeasible, the freedom to perform reactions with independent thermal conditions is advantageous.

3.4 Conclusions

In pursuit of a method for controlling the temperature of a 1 µL aqueous sample in our polymer microfluidic device, a series of technological innovations for the distribution and modulation of infrared radiation and subsequent temperature measurement for rapid thermocycling were developed. We sought to match or improve upon the speed and accuracy of conventional PCR instrumentation while bringing the novel functionality of thermal multiplexing to a microfluidic PCR platform.

The optical system developed for achieving rapid thermocycling of a microfluidic sample was built around a 1450 nm laser diode. This radiation source provided a wavelength efficiently absorbed by water while being minimally absorbed by our microchip substrate material (PMMA), providing enough energy to achieve ramping rates up to 60°C/sec while consuming a relatively low amount of electrical power, potentially amenable to a point-of-care application. Coupling the laser to appropriate optical elements and making use of a combination of off-the-shelf optomechanics and precision fabricated components yielded an optical system capable of accurate control of focal spot size and alignment to a corresponding target reaction chamber. Miniature solenoids were implemented as optical shutters and demonstrated to

be an effective and low-cost method of laser modulation, providing the full range of temperatures required for PCR.

A method for temperature feedback was developed in which miniature thermocouples were embedded in our microchip during the thermal bonding process with the tip within close proximity to our reaction chambers. Through a careful calibration process, this reference temperature could be reliably related to sample temperature. Still, temperature sensing proved to be the most challenging task in the development of our instrument and our solution has a number of limitations. In addition to the cumbersome steps required for fabricating our microchips with embedded thermocouples, reproducibility and the effects of ambient conditions must be considered. Without the use of environmental control measures as implemented for our open-loop instrument, changing ambient temperature has the potential to affect the accuracy of the microchip calibration, requiring on-site calibration and verification of negligible changes in ambient temperature. Another potential issue relating to environmental conditions is the ability to achieve reasonable ramping rates in extreme temperatures. In a cold climate, heating rates and maximum achievable temperature could be severely limited, potentially preventing the ability to achieve denaturation and causing longer temperature transitions that could contribute to a higher likelihood of non-specific products. Similarly, a hot climate could diminish cooling rates and prevent the ability to reach low annealing temperatures since the warmest conditions observed in some places approaches the low end of the annealing regime. A non-contact temperature measurement approach using a thermal camera was also explored and showed promise for future applications of our technology. Further discussion of this topic can be found in Section 5.2.2.

We combined our microchip, radiative heating system, and temperature measurement technique to develop two platforms: 1) an open-loop approach with real-time fluorescence monitoring capabilities and 2) a closed-loop approach capable to thermal

multiplexing of multiple samples. Each of the platforms were used to demonstrate the unique power of our laser-mediated thermocycling system to achieve accurate temperature control, rapid sample processing, real-time detection, and independent control of each reaction chamber (i.e., thermal multiplexing) to operate at the ideal conditions for each target screened. The further application of our technology toward virus detection is presented in Chapter 4.

CHAPTER IV

VIRUS DETECTION

The validation of our microfluidic platform was conducted by performing amplifications of various genetic targets, demonstrating the ability of our polymer microchip (detailed in Chapter 2) and laser-mediated thermocycler (detailed in Chapter 3) to sensitively and specifically detect viruses. We first established the viability of our microchips for PCR through the use of a custom water bath thermocycler. Once protocols were proven with our microchips, we proceeded to perform these reactions using the our laser-based thermocycling system. We then examined the performance of our system to assess its viability as a diagnostic instrument.

4.1 Water bath PCR testing

During the development of our microchips, we realized the need for a method of testing the compatibility of our microchips with the chemistry of PCR independent of our laser heating system. Initially, a 96-well plate thermocycler (Eppendorf, Mastercycler) with an in-situ block adapter, which is designed to accommodate glass slides, was used for thermocycling our microchips but insufficient temperature homogeneity through the thickness of the microchip prevented accurate thermocycling. An experiment in which a microchip with a thermocouple inserted into a reaction chamber was run on the plate thermocycler revealed a significant temperature gradient between the sample and the block adapter on which the microchip was installed. This resulted in under-heating of the sample. Efforts to bias the setpoints to counteract the gradient were mostly unsuccessful.

Instead, a water bath thermocycling system was developed. This device was introduced in Section 2.4.3 and can be seen in Figure 24. It functioned as a 2-axis gantry

system for transferring microchip(s) between a set of three beakers, each maintained at the three particular setpoints required for the denature, anneal, and extension steps. A LabVIEW program provided the control interface for selecting the thermocycling parameters. Initial tests using a microchip with an embedded in-chamber thermocouple revealed the transition times for shifting between various setpoints, which proved to be longer than the transition times observed for our laser-mediated heating and even conventional thermocyclers. This made sense considering the insulating behavior of the polymers, its thickness, and the indirect delivery of heat from water to sample. From this characterization, conservative hold times were programmed to allow enough time for samples to reach steady state. In addition, the extended initial denature step typically included in thermocycling routines was omitted for the water bath tests since this simplified the programming and seemed unnecessary considering the relatively long denature hold used for every cycle. Thermocycling parameters for these tests can be found in Table 7 in Appendix A.

Since the constraints of radiation delivery were not applicable to the microchips when using the water bath system, special versions were fabricated with arrays of eight chambers. This enabled much higher throughput per experiment and provided a more user-friendly way to screen serial dilutions on a single microchip to test limits of detection.

Samples were prepared according to the protocols provided in Appendix A. Once the 1 µL samples were loaded into the microchip(s), the ports were sealed. Early experiments made use of heat-resistant adhesive-backed polypropylene film (Excel Scientific, ThermalSeal) for this purpose but extended exposure to the heated water baths weaker the adhesive and sample loss via leakage was occasionally encountered. Instead, a custom clamping fixture was fabricated by laser cutting 3 mm thick PMMA into rectangular frames large enough to sandwich our microchip with an overhang featuring holes to secure the two frames with 8-32 machine screws and nuts. A

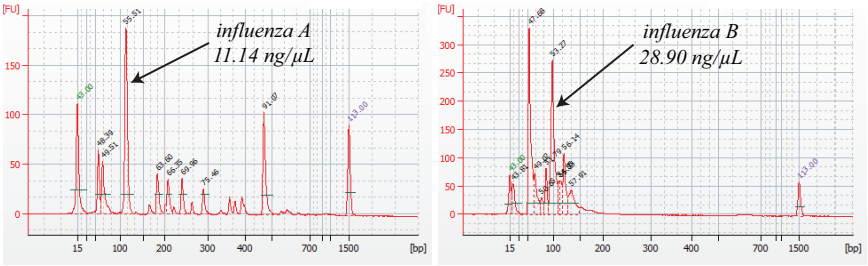

Figure 53: Sample electropherograms for the detection of influenza A (*left*) and influenza B (*right*) extracted from clinical patient samples. Amplifications were performed in 1 µL reaction volumes using our polymer microchip and water bath thermocycling system. The outer peaks correspond to the markers used for quantification while the other unlabeled peaks resulted from primer-primer interactions and non-specific amplification products due to the presence of host DNA.

laser cut gasket was applied to one side of the microchip along the ports and the PMMA frames were clamped over the microchip, sealing the ports and keeping the samples contained for the duration of the thermocycling. After cycling, the clamping fixture was removed, samples were extracted from the microchip using a pipettor and transferred to a 0.2 mL PCR tube for storage at 4°C until ready for detection via electrophoresis using the Agilent Bioanalyzer.

The water bath system was used to successfully amplify a variety of genetic targets, both DNA and RNA, as shown throughout this thesis, including purified λ-phage and Epstein Barr virus (EBV) DNA. Initial tests of microchip passivation strategies made use of the water bath system for a comparison of λ-phage amplifications (Figure 28). Sensitivity tests using the EBV amplification also made use of the water bath system to demonstrate successful on-chip reactions down to approximately 100 starting copies (Figure 29). The ability of our microchip to amplify viral targets in a clinical sample was also tested for RNA viruses Influenza A and Influenza B. Leftover nasopharyngeal swab samples from pediatric patients with known infections were provided by Egleston Pediadric Hospital. As detailed in Appendix A, nucleic acids were extracted using the Qiagen QIAamp Viral RNA Mini Kit and prepared using a one-tube RT-PCR premix. A fourth hot plate and beaker was used for the initial reverse transcription

before being thermocycled using the automated system. Resulting electropherograms are shown in Figure 53 indicating the detected 100 bp peaks for the influenza targets as well as many non-specific peaks due to primer-primer interaction and the presence of host (human) DNA.

4.2 Experimental procedures

Once a reaction had been confirmed as compatible with our microchip using the water bath thermocycler, the protocol was ready to be demonstrated using our laser-mediated thermocycler. Although the reaction chemistry translated between thermocycling methods, we needed to address factors unique to our instrument such as alignment, calibration, and thermocycling parameters.

First, the layers of our microchips were micro-milled in large batches using the techniques described in Section 2.2. By producing many devices during a single session with the CNC milling center, any errors such as inaccurate zeroing of tooling are uniform over the entire batch of microchips and therefore avoiding potential problems of dimensional inconsistencies. Microchip layers were then cleaned by sonicating in deionized water, rinsing with isopropanol and water, and drying with compressed nitrogen. A calibration microchip was first thermally bonded with thermocouples aligned for in-chamber temperature measurement. After the 30 min bonding process, the fixture was allowed to cool for 30 min. Then standard microchips with near-chamber embedded thermocouples were bonded, with care given to the thermocouple tip position to ensure chip-to-chip consistency.

The calibration microchip was first installed in the system, using the alignment pins on the pressure manifold to mount the microchip against the sealing gaskets then sliding the manifold over the 6 mm construction rods of the optical system. Toner-coated burn paper (see Figure 34) was then secured over each reaction chamber and the two lasers, driven by a common power supply, were used to irradiate the microchip

and determine the approximate alignment of the laser focal spots. If necessary, small adjustments to collimating lens position were made using the x-y translating mounts housing the lenses. After removing the burn paper, the pressure manifold / microchip assembly was unmounted from the optical system and the two reaction chambers were loaded with 1 µL mock samples consisting of reaction buffer using the mineral oil technique described in Section 2.4.3. The pressure manifold with a loaded calibration microchip was remounted to the optical system and the pressure lines were attached to the manifold with luer connectors and the regulated N_2 tank was opened to supply 40 psi of pressure. The lasers were then powered, allowing the reaction chambers to reach steady state and small adjustments to collimating lens positions were made, if needed, to match the temperatures in each reaction chamber.

Next, the calibration process, detailed in Section 3.2 and briefly summarized here, was carried out to generate a correlation between laser driving voltage and approximate in-chamber temperature. With the lasers turned off, the pressure was vented and the calibration microchip was unmounted from the system and replaced with a standard microchip to be used for the second half of the calibration. By repeating the series of laser driving voltages used for heating the calibration microchip, near-chamber temperatures could be recorded and correlated with approximate in-chamber temperature. Based on this correlation, a series of calibration curves were generated by pivoting the original calibration around the common room temperature measurements. This was done to correct for the bias introduced by the interactions between the in-chamber thermocouple and laser radiation when collecting the data with the calibration microchip. By testing each calibration curve with our λ-phage amplification protocol and locating the calibration that provided maximum PCR yield, the accurate calibration curve was identified.

Since slight variations in the thermal dynamics of our microchips due to the tolerances of manual positioning of the thermocouple tips resulted in a need for tuning our

calibrations for each unique microchip. Since the need to repeat the entire calibration process for every microchip would be prohibitively time-consuming if screening multiple subjects, we first examined the possibility of repeated use for our microchip. Although they were designed to be low-cost and therefore disposable, avoiding potential cross-contamination and the need for a thorough cleaning process, the ability to reuse our microchips during the testing phase would save time. We tested the viability of reuse by running λ-phage amplification in one of the reaction chambers, cleaning the chamber by rinsing with isopropanol and deionized water and drying with compressed N_2, then repeating the amplification. This was performed eight times and the results from end-point detection of the PCR products are shown in Table 3. It was found that after two to three tests, the device was unable to demonstrate successful amplification. We suspect the cause of this limited use is a combination of the microscale damage (e.g., crazing) induced by heat and pressure experienced by the reaction chamber surfaces during operation and the effects of isopropanol during the cleaning process. We therefore limited the use of our microchips to two runs before delaminating the microchip, removing the thermocouples, and disposing of the used microchip layers as biohazards waste.

Table 3: Repeated use of our microchips exhibits stable thermal performance, as indicated by consistent heating and cooling times, but decreasing PCR yield until the device is unable to perform successful amplification.

sample	**heating time (sec)**	**cooling time (sec)**	**PCR yield (ng/µL)**
1	21.14 ± 0.66	16.76 ± 0.45	29.33
2	20.32 ± 0.57	17.54 ± 1.01	23.27
3	18.32 ± 1.00	15.94 ± 0.70	15.89
4	15.34 ± 0.72	15.61 ± 0.40	0.84
5	14.10 ± 1.04	16.42 ± 0.21	0
6	14.90 ± 0.28	15.20 ± 0.61	0
7	15.50 ± 0.72	15.50 ± 0.63	0
8	16.60 ± 0.30	16.24 ± 0.67	0

Since we could only safely use a microchip twice, we developed a method for

quickly calibrating new microchips. It was found that we could use the original calibration curve and adjust only the slope for the calibration of the new microchip. This adjustment was guided by the measurements of the heating rates of the new device. This was performed by loading the microchip with reaction buffer and running the first ten cycles of our λ-phage thermocycling routine. Heating rates during the ramping phase from extension to denature steps were then averaged and compared the those exhibited by the original, accurately calibrated microchip. If heating rates are faster, the slope of the calibration curve is decreased and vice versa. Within a few iterations, a reliable heuristic had been developed for calibrating all new microchips, dramatically reducing the preparation time required for each experiment.

The first reaction used to validate our system was λ-phage amplification. In determining the ideal thermocycling parameters for this reaction, we began by implementing the same conditions used with a conventional thermocycler. Next, following advice from collaborators who had demonstrated rapid thermocycling with a microfluidic system using minimal temperature hold times, we did the same for our thermocycling program, arriving at hold times of 4 sec for denaturing, 5 sec for annealing, and 5 sec for extension, resulting in a total runtime of 10 min [118]. This success with reducing hold times agrees with the revised thermocycling paradigm that acknowledges the ranges of temperatures at which the biochemical activity necessary for PCR occurs [167].

Once our methods had been proven effective for the repeatable amplification of λ-phage, more challenging reactions such as the herpesvirus amplification, specifically using Epstein Barr virus (EBV) as template, were tested, making use of consensus degenerate primers as developed by the CDC. This particular reaction required an annealing temperature of 48°C, making it an ideal candidate for demonstrating thermal multiplexing with our two-chamber system. After running the EBV reaction in both chambers to confirm our capability of performing the amplification, we tuned

the thermocycling parameters and discovered that only slightly reduced hold times (see Table 8 in Appendix A) generated the highest PCR yields.

The λ-phage and EBV amplifications were then performed simultaneously on a single microchip using thermal multiplexing. Although the λ-phage thermocycling could be performed faster, the longer hold times required for EBV amplification were used for the multiplexed operation, since the thermocycling needed to be synchronized and the longer hold times were not detrimental to λ-phage amplification. The preliminary results for this demonstration were presented in Section 3.3.2. In order to establish repeatable performance and illustrate the utility of our novel multiplexing approach, a set of 12 microchips were used to process 24 samples, with λ-phage loaded in to chamber 1 and EBV loaded into chamber 2, to test (in triplicate) four "annealing modes": 1) low annealing, in which both samples were cycled with an annealing temperature of 48°C; 2) high annealing, in which both samples were cycled with an annealing temperature of 68°C; 3) average annealing, in which both samples were cycled with an annealing temperature of 58°C; 4) thermally multiplexed annealing, in which samples were cycled independently with annealing temperatures of 68°C and 48°C for chambers 1 and 2, respectively.

The protocols listed in Appendix A were followed for preparing our microfluidic samples. Template concentrations of 5.4 pg/μL (1×10^5 copies/μL) and 500 fg/μL (1×10^5 copies/μL) were used for λ-phage and EBV, respectively, resulting in 540 fg of λ-phage and and 50 fg of EBV. (Note: The λ-phage DNA was provided in purified form with a known concentration while EBV template was supplied by the CDC, which they use for positive controls during herpesvirus screening, and was quantified using the procedure listed in Appendix A.) These dilutions provided 1,000 starting copies for each reaction. Following the execution of all twelve microchip runs, PCR products were detected by electrophoresis.

4.3 End-point detection

Electrophoretic detection via Agilent 2100 Bioanalyzer, which requires only 1 µL sample volumes, was used to determine the performance of our system. As acknowledged in previous sections, end-point detection can only be considered semi-quantitative, which proved to be suitable for measuring the basic trends exhibited by the data. The results for our testing of the four "annealing modes" described above are shown in Table 4, reported as yields, which are measured by the Bioanalyzer by comparing detected peaks to markers of known concentration included with each sample loaded into the instrument for detection. The corresponding electropherograms for the four data sets are shown in Figures 54–57.

As the data reveals, when microchips were run with identical annealing temperatures, only the reaction operating at its ideal annealing condition was successful while the other failed, with the exception of one of the λ-phage samples that produced a detectable peak when run with the non-ideal low annealing temperature of 48°C. This

Table 4: Detection results for λ-phage and EBV amplification using our laser-mediated thermocycler to test four distinct thermal conditions to demonstrate the advantage of thermal multiplexing for optimal performance. Each condition was tested in triplicate.

annealing mode	**microchip**	**annealing temp (°C)**		**PCR yield (ng/µL)**	
		chamber 1	*chamber 2*	*chamber 1*	*chamber 2*
		λ-phage	*EBV*	*λ-phage*	*EBV*
low	1	48		0.13	11.16
	2			0	6.38
	3			0	8.58
high	4	68		25.14	0
	5			9.16	0
	6			8.20	0
average	7	58		0.46	0.56
	8			0.40	1.29
	9			0.50	0.50
thermally multiplexed	10	68	48	11.71	12.31
	11			5.12	8.95
	12			7.33	10.35

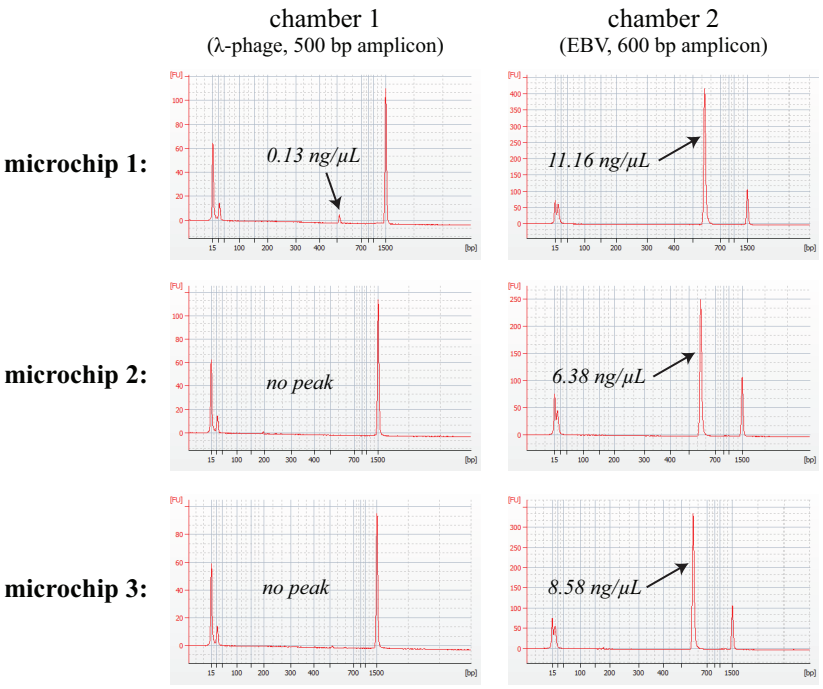

Figure 54: Electropherograms for dual-chamber PCR using our polymer microchip and laser-mediated thermocycler. Both samples were cycled in parallel at the low annealing temperature of 48°C, ideal for EBV amplification. (540 fg λ-phage template, 50 fg EBV template, n=3)

is not surprising considering the tendency for primers to anneal within a large range of temperatures under its melting temperature. A major consequence of operating at an excessively low annealing temperature not captured with this demonstration is the appearance of non-specific products due to non-specific annealing observed when host DNA is present. Since only purified template was used for these experiments, 100% specificity was observed as expected. Average yields at the low annealing condition were 0.04 and 8.71 ng/μL for λ-phage and EBV, respectively. For the high annealing condition, average yield was 14.17 and 0 ng/μL for λ-phage and EBV, respectively.

When the microchips were run at the average annealing temperature, weak performance was observed as indicated by the relatively low yield for all samples. Although still detectable with the 1,000 starting copies used here, more sensitive detections would most likely be impossible. Average yields at the low annealing condition were 0.45 and 0.78 ng/μL for λ-phage and EBV, respectively.

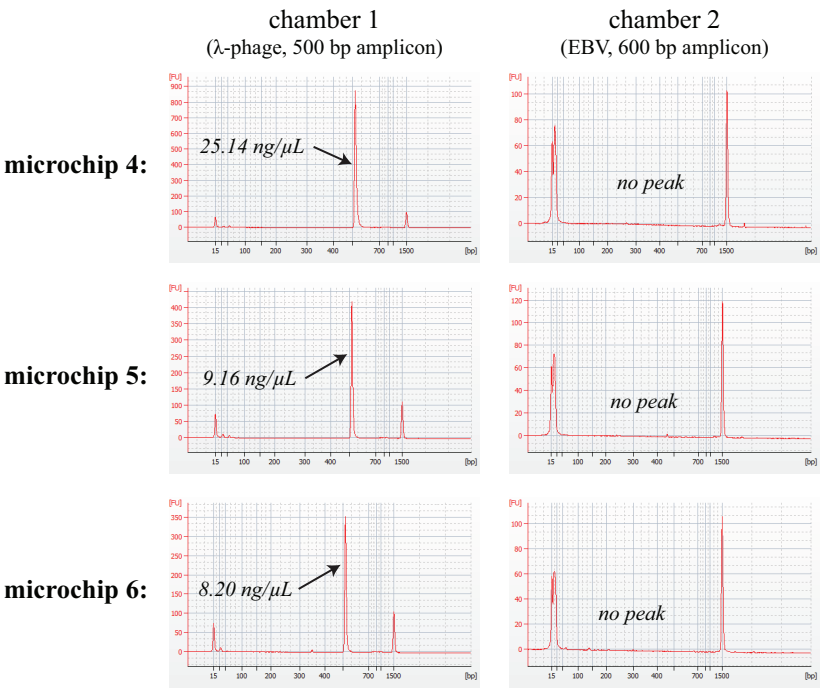

Figure 55: Electropherograms for dual-chamber PCR using our polymer microchip and laser-mediated thermocycler. Both samples were cycled in parallel at the high annealing temperature of 68°C, ideal for λ-phage amplification. (540 fg λ-phage template, 50 fg EBV template, n=3)

When thermal multiplexing was employed for the dual amplification at the ideal conditions for each reaction, electropherograms indicate efficient amplifications. Average yields for the multiplexed annealing conditions were 8.05 and 10.54 ng/μL for λ-phage and EBV, respectively. These experiments demonstrate the importance of operating at the optimal thermal conditions and the ability of our instrument to reliably provide this functionality.

4.4 Conclusions

Having established and validated novel methods for fabricating and characterizing a microfluidic PCR platform featuring a low-cost microfluidic device for handling 1 μL samples and a laser-based thermocycling system for rapid heating and accurate temperature control, we sought to apply our technology towards practical applications in virus detection.

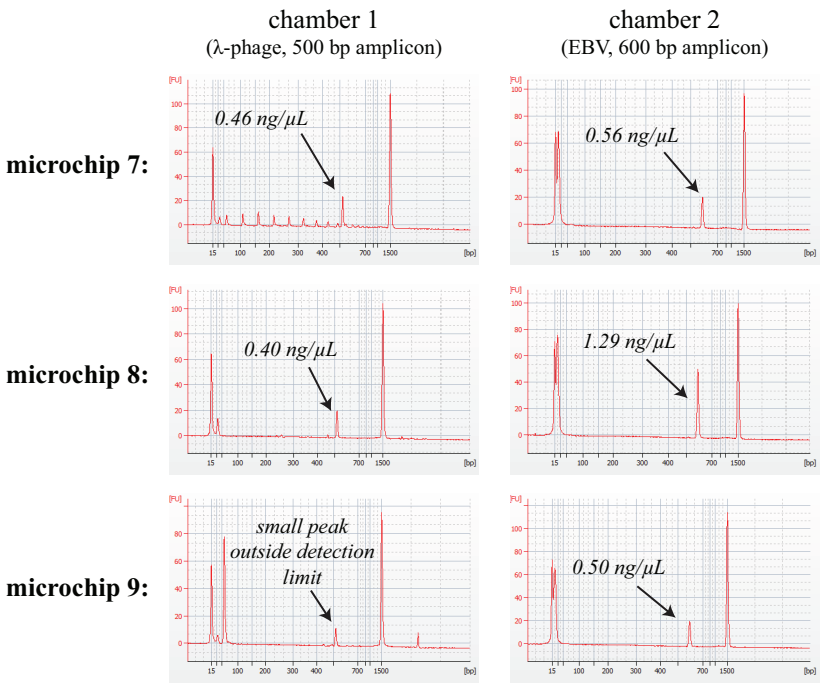

Figure 56: Electropherograms for dual-chamber PCR using our polymer microchip and laser-mediated thermocycler. Both samples were cycled in parallel at the average of the two targets' ideal annealing temperatures, 58°C. (540 fg λ-phage template, 50 fg EBV template, n=3)

Our initial efforts to explore the variety of microfluidic PCR protocols and their compatibility with our microchip made use of a robotic system we built to perform PCR with our microchips independent of our infrared laser heating system to isolate issues specific to our microchip. This allowed us determine the optimal passivation strategy of loading samples with mineral oil to eliminate dead volume and reduce inhibitory effects of adsorption. We also demonstrated high sensitivity amplification down to 100 starting copies of EBV template.

We next demonstrated virus detection using our complete platform, including the harnessing of thermal multiplexing to perform efficient PCR on distinct genetic targets requiring their own unique thermal conditions. A detailed procedure was developed for preparing our microchips to ensure repeatable performance, including a protocol for first performing an baseline calibration and then using an abbreviated calibration technique for subsequent devices to expedite processing of multiple samples while

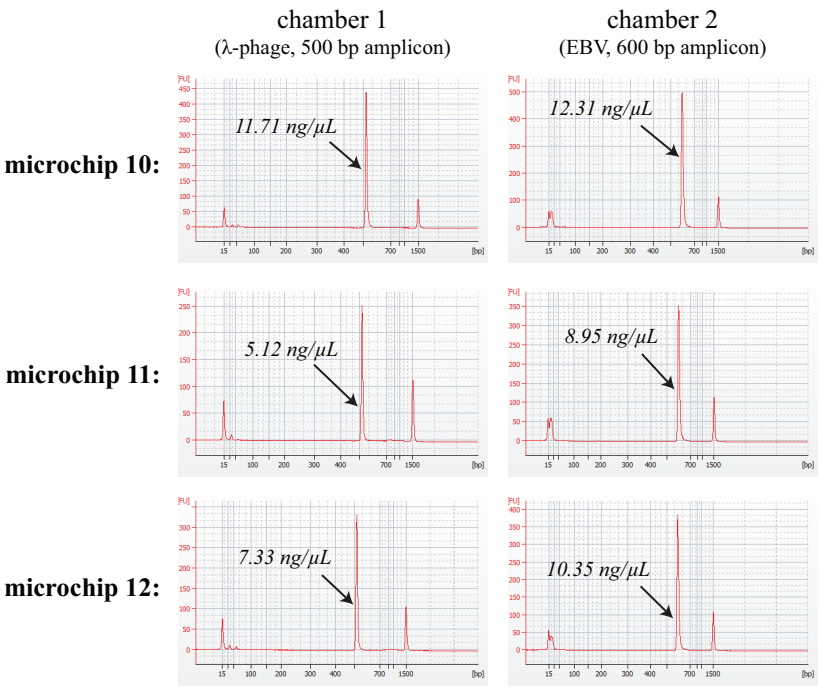

Figure 57: Electropherograms for dual-chamber PCR using our polymer microchip and laser-mediated thermocycler. Samples were cycled independently using thermal multiplexing via optical modulation, each run at its optimal annealing temperature of 68°C and 48°C for λ-phage and EBV amplification, respectively. (540 fg λ-phage template, 50 fg EBV template, n=3)

accounting for inherent fabrication inconsistencies to maintain accurate temperature control. These techniques were applied to the co-amplification of λ-phage and EBV template on a single microchip in separate chambers. By performing reactions in triplicate and comparing our thermal multiplexing approach to thermocycling with uniform temperatures (i.e., no independent control of chamber-to-chamber temperature), as a user would be restricted to if using a conventional thermocycler, the power of our technology was demonstrated. Future work will focus on scaling the system for higher throughput and testing a greater variety of genetic targets, including clinical samples.

CHAPTER V

CONCLUSIONS AND FUTURE WORK

Despite the availability of powerful bioanalytical tools, the need for more sophisticated and more easily deployable technologies for the detection of pathogens shows no signs of diminishing. There is an urgent need to provide timely treatment of not only routine infections such as influenza and RSV, which will reduce cases of needless hospital admission and minimize the growing problem of overprescription of antibiotics, but also the early detection and surveillance of pandemic infections. Molecular diagnostics, specifically the polymerase chain reaction (PCR), have provided some of the most effective solutions to addressing this need. But available PCR instrumentation has yet to deliver the speed, usability, deployability, and financial practicality required of a system capable of meeting the most demanding needs of pathogen detection scenarios, as evidenced by current news headlines regarding the Ebola virus outbreak. There are widespread complaints regarding the lack of appropriate tools for efficiently detecting the virus. Microfluidics show the greatest promise for reducing volumes and increasing the speed of analysis, but the state-of-the-art microfluidic PCR instrumentation (research-grade and commercial) has introduced only incrementally improved performance while still operating within the paradigms of conventional instruments. In addition, complexity and costs of microfluidic devices remain prohibitively high for many potential users, especially in low resource settings.

Towards the development an instrument to fill this void and overcome the challenges of high performance yet affordable pathogen detection, we designed, fabricated, and validated a PCR platform capable of sensitive, multiplexed amplification using 1 µL sample volumes. Chapter 2 describes the development and testing of a low-cost

polymer microchip. Finite element modeling guided the design of our reaction chambers, allowing us to simulate the thermal response of a variety of chamber geometries and spacing when undergoing radiative heating. Fabrication by micro-milling proved to be an effective technique for prototyping devices and enabled three-dimensional geometries difficult to achieve with traditional microfabrication methods. Next, a systematic study of geometry and material-related reaction inhibition was conducted, combining an experimental exploration of the phenomenon with the groundwork for a theoretical model to predict inhibition effects due to irreversible adsorption of reagents. Chapter 3 details the construction of both open-loop and closed-loop temperature control systems to perform thermocycling with our microchip. First, an optical system for delivering and modulating infrared radiation to our microchip was built and tested. Next, a temperature feedback system was developed in which embedded thermocouple provide indirect measurement of sample temperature through a rigorous calibration process. An open-loop version of our instrument was first used to perform quantitative PCR towards the application of rapid gene expression measurement. Next, a closed-loop version was built to perform two simultaneous amplifications, making use of real-time temperature feedback for more complex operations, including the preliminary demonstration of thermal multiplexing. Finally, Chapter 4 covers the implementation of our complete platform towards repeatable and sensitive thermally multiplexed amplification of λ-phage and Epstein Barr virus (EBV) targets, demonstrating our instrument's ability to operate at the extremes of potential annealing temperatures and showing the importance of amplifying at optimal thermal conditions compared to a compromised condition, as one would be restricted to with a conventional instrument. A comparison of our platform to commercial PCR technologies can be seen in Table 5. Although the state of the art instrumentation typically has higher sample capacity, integration with upstream processing (e.g. extraction as performed with the FilmArray system), and real-time detection capabilities, our

microfluidic system offers several advantages, notably the low sample input volume (as distinct from reaction volume, which can be on the order of a few nanoliters for instruments such as those offered by Fluidigm), and the ability to achieve thermally multiplexed conditions. Factors that are difficult to quantify or unpublished, such as ease-of-use and thermal accuracy, were not considered for this comparison but are important nonetheless.

Table 5: Comparison of our microfluidic platform with common PCR instrumentation.

	Biorad MJ Mini	**Roche LightCycler 2.0**	**Fluidigm EP1**	**BioFire FilmArray**	***our system***
sample volume	5-100 µL	10–100 µL	4–8 µL	200 µL	1 µL
sample capacity	48	32	12	1	2
sample container disposability	single use	single use	single or multiple use	single use	single use
sample container cost per test	$0.10	$0.75	$500	$150	$0.50
instrument cost	$4k	$60k	$100k	$40k	$4k*
heating modality	conductive	convective	conductive	conductive	radiative
max ramping rate (°C/s)	3	20	5	2	60
thermal capabilities	uniform or gradient	uniform	uniform	uniform	multiplexed
sample recoverable?**	yes	yes	no	no	yes

* estimate based primarily on materials and hardware costs
** important for downstream analysis such as sequencing

Cost was considered throughout the development of our instrument, especially in the design of our microchip. By avoiding traditional microfabrication techniques and pursuing low-cost materials such as PMMA to yield a disposable device, microchip cost can be estimated at around $0.50 per device. This is based on material and labor cost and discounts one-time investments such as a capable CNC vertical milling center, which in the case of the Haas OM-1A costs $60,000, as well as tooling, which totaled approximately $100. The cost of the laser-mediated thermocycling system built for our two-chamber microchip can be broken down as follows – Infrared laser

and accompanying electronics (e.g., driver, power supply): $500; Optical components for alignment, collimation, and modulation: $750; Temperature measurement system, including thermocouples and signal conditioning circuitry: $500; Data acquisition module: $2,000. These cost estimates combine to total $3,750. Some of these figures represent overestimates since most of the off-the-shelf and custom items were purchased in small quantities. Lower unit prices would be paid for production scale orders. Costs that were not accounted for in this estimate include custom fabricated parts, such as the pressure manifold, and software, since although NI LabVIEW was used for our programming and user interface purposes, a lower level program with a custom GUI would be developed for a commercial version of the instrument. The greatest opportunity for cost savings is data acquisition hardware, since the National Instruments DAQ module used in this work, USB-6221 BNC, offers far more features than we require. A custom PCB would eventually be fabricated to perfectly match our system specifications to provide significant cost savings.

5.1 Major contributions

To summarize the major contributions of this work:

- **Generalized model of radiative heating in microfluidic devices**: A generalized model was developed for the prediction of thermal response for any combination of radiation source and device given optical properties of the source, device geometry, and substrate material properties [178].

- **Fabrication method for polymer microfluidics**: Instead of using traditional microfabrication methods, a technique was developed combining micromilling and thermal bonding. Unlike most microfabrication methods, it accommodates a variety of materials, simplifies prototyping, offers more options for three-dimensional geometries, and yields a durable device [179].

- **Open and closed-loop control schemes for microfluidic thermocycling**: Both open-loop and closed-loop systems were developed for thermocycling with our microfluidic device. Open-loop offers ease-of-use and straightforward integration with real-time fluorescent monitoring. Closed-loop provides more precise, flexible, and scalable temperature control.

- **Highly sensitive PCR using consensus degenerate reactions from the CDC**: Performed PCR with consensus degenerate primers, a CDC chemistry used for screening any virus, known or unknown, within a particular viral families. Sensitivity down to 100 copies was demonstrated. This is a challenging type of reaction that had never been done with a microfluidic device [169].

- **qRT-PCR for stem cell engineering**: Performed quantitative, reverse transcription PCR with RNA extracted from mouse embryonic stem cells. This can serve as a platform for rapid genetic feedback to drive stem cell engineering studies [87].

- **Systematic study of the role of material and geometry in PCR inhibition**: Conducted a systematic study of the role of material and geometry on PCR inhibition in microfluidics. Despite pervasive concern over this issue, only anecdotal accounts of addressing inhibition issues associated with high SA:V environments had been reported. We quantitatively studied the effect of SA:V on PCR yield for multiple materials and passivation strategies along with a basic theoretical model of the inhibition process [169].

- **Sample loading technique for improving PCR yield**: Developed a sample loading method that eliminates dead volume and provides optimal passivation using mineral oil to partially encapsulate the PCR sample, enabling more sensitive detection than prevailing methods.

- **Invented mode of multiplexed temperature control**: Invented a mode of multiplexed temperature control that enables independent control of temperature in adjacent PCR reaction simultaneously.

- **IRB-approved work with clinical samples**: Applied our microchip technology to detect influenza A and B from patient samples sourced from Egleston Pediatric Hospital (CHOA).

5.2 Future work

5.2.1 PCR inhibition model

The theoretical model of adsorption-based PCR inhibition presented in Section 2.4.2 was useful in its application for the characterization of the polymers tested in our experimental study, quantifying their suitability as PCR device substrates. Future efforts should be dedicated to expanding the model for more deterministic purposes, combining geometry with known material properties of the substrate and considering the adsorption of other reagents. The incorporation of the temperature dependence of molecular diffusion would also better capture the mechanisms at work. Another important step towards a better understanding of adsorption-based PCR inhibition would be an experimental study in which reagent concentrations are independently varied better delineate the molecules most prone to irreversible adsorption.

5.2.2 Temperature feedback

One of the deficiencies of our current instrument that would need to be addressed for future iterations is the temperature measurement system. The task of manually embedding and calibrating the thermocouples used for monitoring near-chamber temperature is one of the most impractical steps in the use of our platform in its current state. To avoid the tedious and error-prone step of embedding thermocouples, a reusable comb-like device consisting of a series of thin-film temperature probes arrayed

on a rigid substrate could be inserted into the series of slots running along the microchip and terminating along the edge of each reaction chamber with an adequately sizes barrier dividing the chamber and probe to avoid deformation due the heat and pressure. Another measure to improve the temperature measurement system would avoid the need for a special calibration microchip with thermocouples measuring biased in-chamber temperature; instead, a standard microchip would be filled with a temperature sensitive dye (e.g., Rhodamine B), mounted on an inverted fluorescence microscope, and heated to various temperatures. Using a known calibration between fluorescence and temperature, the in-chamber temperature could be directly correlated with the near-chamber measurement, obviating the process of iterative PCR attempts to locate an accurate calibration. Finally, the most desirable configuration would be completely non-contact (i.e. all optical) through the implementation of a thermal camera for temperature sensing. The potential for this method has already been demonstrated with our microchip (see Section 3.2.2) and with more sophisticated calibration methods and an enclosure for consistent environmental conditions, this approach would yield a simple and scalable system for microfluidic temperature measurement.

5.2.3 Scaling

Increasing the scale of our instrument would be a critical step for a commercially viable configuration of our technology. The two-chamber version reported in this thesis was for proof-of-concept purposes. The instrument would need to perform amplification of at least eight targets to be diagnostically useful, since the parallelized screening made possible with our technology would need to cover not only a range of potential infectious agent but also controls. Towards this scaling, we have already conceptualized an eight-chamber system as shown in Figure 58. Fiber-coupled infrared lasers would be constrained under an optical system for focusing and modulating each

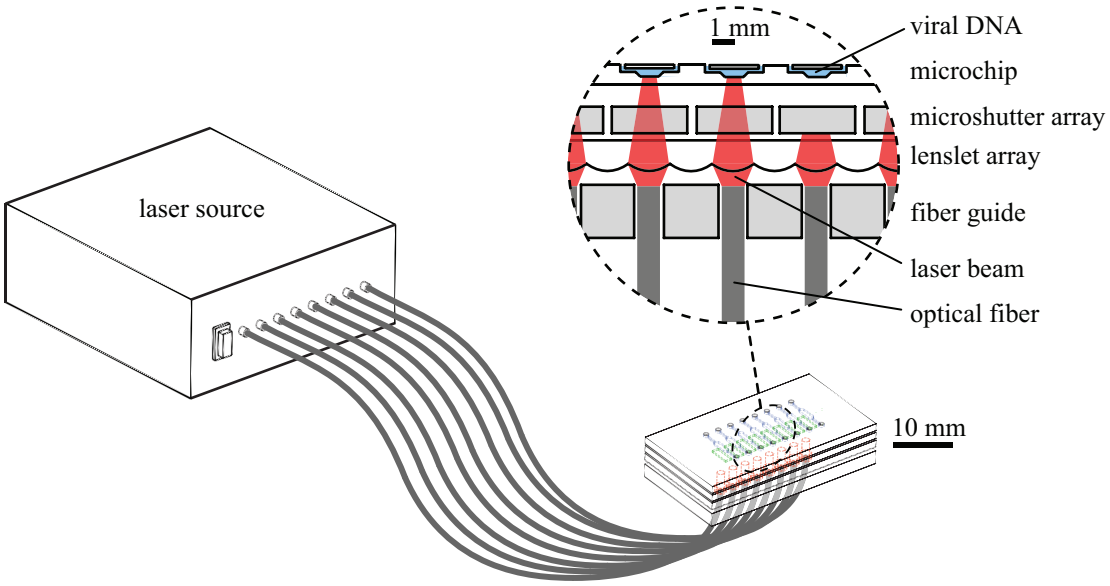

Figure 58: A concept for increasing the throughput of our PCR platform, using fiber-coupled infrared lasers to deliver radiation to an array of 1 µL reaction chambers spaced at the minimum 3 mm. An optical system (*inset*), including an optical shutter array, provides spatial modulation for thermal multiplexing.

channel of radiation. Reaction chamber spacing could be collapsed to its minimum of 3 mm to maintain adequate thermal isolation while minimizing device footprint. A lower power alternative to solenoids would be implements for modulation. The most elegant solution would be a custom liquid crystal optical shutter with individually addressable pixels, which can easily be fabricated by companies such as Boulder Nonlinear systems, who supplied a quote for such a device. The major downsides to this option would be cost and baseline attenuation, since 50% of incident radiation would be absorbed due to the polarization dependence of the liquid crystal system.

To enhance the ease of use of a scaled version of our instrument, a future addition would be the use of lyophilized primers immobilized in each chamber. By including the unique primers for each reaction in each chamber, sample preparation and loading would require only a single reaction mix and one-step microchip loading.

APPENDIX A

PROTOCOLS

A.1 Nucleic acid extraction

Nasopharyngeal swabs provided by collaborators at Egleston Pediatric Hospital were screened for three possible RNA viruses (Influenza A, Influenza B, and RSV). To prepare the nucleic acids for RT-PCR, RNA extraction was performed using a Qiagen QIAamp Viral RNA Mini Kit.

A.2 PCR, qPCR, RT-PCR, and qRT-PCR preparation

All PCR reactions were prepared from a commercial master mix (Bioneer AccuPower PCR PreMix). The premix consists of a lyophilized pellet of 2.5 U Top DNA polymerase, 250 µM dNTPs (dATP, dCTP, dGTP, dTTP), 10 mM Tris-HCl (pH 9.0), 30 mM KCl, 1.5 mM $MgCl_2$, tracking dye, and stabilizer. Similarly, all RT-PCR reactions were prepared from a commercial master mix (Bioneer, AccuPower one-step RT-PCR PreMix). This premix consists of M-MLV Reverse Transcriptase, RNA dependent DNA polymerase, and a thermostable DNA polymerase in a lyophilized mix of dNTPs, reaction buffer, RNase inhibitor, tracking dye, and stabilizer. For use with our open-loop system, quantitative PCR and RT-PCR reactions were prepared using the same master mixes with the added component of an intercalating dye. A cooling rack was used during all steps of the reaction preparation to maintain reagents near 0°C. All laboratory bench surfaces and pipettes were decontaminated using DNA AWAY and RNase AWAY.

To prepare (RT-)PCR mix:

1. Add 44 µL of nuclease-free water* to a 50 µL premix tube.
2. Vortex until pellet is dissolved and spin down.
3. Add 1 µL of 20 µM** forward and reverse primers.

To prepare (RT-)PCR reaction mix:

- For a conventional 50 µL reaction, add 5 µL template DNA to the master mix.
- For a conventional 5 µL reaction, divide the 45 µL master mix into ten 4.5 µL aliquots and add 0.5 µL template DNA to each tube.
- For a 1 µL microchip reaction, prepare 5 µL reaction mixes according to the above step and use 1 µL.

To prepare qPCR master mix:

1. Add 11 µL of nuclease-free water to the 20 µL premix tube.
2. Vortex until pellet is dissolved and spin down.
3. Add 6 µL BSA (1 µg/µL).
4. Add 0.6 µL SYBR Green I (10×).
5. Add 0.4 µL of 20 µM forward and reverse primers.

To prepare qPCR reaction mix:

- For a conventional 20 µL reaction, add 2 µL template DNA to the master mix.
- For a 1 µL microchip reaction, follow the above step to first prepare a 20 µL reaction mix, divide this into 5 µL aliquots and use 1 µL.

To prepare qRT-PCR master mix:

1. Add 14.1 µL of nuclease-free water to the 20 µL premix tube.
2. Vortex until pellet is dissolved and spin down.
3. Add 3 µL BSA (1 µg/µL).
4. Add 0.4 µL SYBR Green I (10×).
5. Add 0.75 µL of 10 µM forward primer.
6. Add 0.75 µL of 10 µM reverse primer.

To prepare qRT-PCR reaction mix:

- For a conventional 20 µL reaction, add 1 µL template RNA (109 ng/µL) to the master mix.
- For a 1 µL microchip reaction, follow the above step to first prepare a 20 µL reaction mix, divide this into 5 µL aliquots and use 1 µL.

*HyClone, HyPure Molecular Biology Grade Water

**Except for the herpesvirus reaction, which used 50 µM primers

Note: For all conventional reactions, 10 µL of mineral oil (Fisher BioReagents) was added to the top of the reaction volume.

To quantify Epstein Barr virus (EBV) template DNA: Template concentration is calculated based on OD and with the known the template size of 4485 bp, copy numbers were determined. Then the detection limit was calculated as follows:

1. The concentration of primer set A Herpes Virus Engineered positive control plasmid DNA (EBV) was 94 µg/mL (by OD measurement), primer set A Herpes Virus Engineered positive control EBV-TA-M-1-1 plasmid DNA was serially

diluted from 10×10^{-1} to 10×10^{-12}, nested PCR was performed from 10×10^{-5} to 10×10^{-12} dilution according to primer set A Herpes Virus Consensus Primer PCR Protocol (internal CDC documentation), for first round positive band appeared at end of 10×10^{-6} dilution, for second round positive band appeared at end of 10×10^{-9} dilution.

2. Calculate the PCR reaction sensitivity using the formula of Calculate RNAPlasmid Copy Number Detected in S/PDD/Primer Info (internal CDC documentation), noting plasmid concentration, MW of plasmid and end point detected.

3. Since the Plasmid concentration of primer set A Herpes Virus Engineered positive control is 94 µg/mL, the MW of plasmid of primer set A Herpes Virus Engineered positive control is 4485 bp, the End point detected for Adenovirus Engineered positive control is 10×10^{-9} dilution, the sensitivity of Pan primer set B Herpes Virus PCR assay is 95.5 molecules with 5 µL total nucleotides acid in total 50 µ PCR reaction using adenovirus engineered positive control plasmid DNA.

A.3 Thermocycling parameters

Table 6: Thermocycling parameters for conventional PCR using a Bio-Rad MJ Mini for 5–50 µL reaction volumes.

reaction	**step**	*temperature (°C)*	*time (sec)*
λ-phage	initial denature	95	2 min
	denature	95	30 sec
	annealing	68	30 sec
	extension	72	30 sec
	final extension	72	2 min
herpesvirus	initial denature	95	2 min
	denature	95	15 sec
	annealing	48	30 sec
	extension	72	30 sec
	final extension	72	7 min
mouse GAPDH	RT	42	1 hr
	initial denature	95	5 min
	denature	95	10 sec
	annealing	56	30 sec
	extension	72	30 sec
RSV	RT	42	1 hr
	initial denature	95	5 min
	denature	95	15 sec
	annealing	50	30 sec
	extension	72	30 sec
	final extension	72	7 min
human β-globin	initial denature	95	2 min
	denature	95	5 sec
	annealing	60	15 sec
	extension	72	20 sec
	final extension	72	2 min
influenza A	RT	42	1 hr
	initial denature	95	2 min
	denature	95	15 sec
	annealing	55	30 sec
	extension	72	30 sec
	final extension	72	7 min
influenza B	RT	42	1 hr
	initial denature	95	2 min
	denature	95	15 sec
	annealing	61	30 sec
	extension	72	30 sec
	final extension	72	7 min

Table 7: Thermocycling parameters for microfluidic PCR using our custom water bath system for 1 µL reaction volumes.

reaction	**step**	*temperature (°C)*	*time (sec)*
λ-phage	denature	95	1 min
	annealing	68	2 min
	extension	72	2 min
	final extension	72	5 min
herpesvirus	denature	95	1 min
	annealing	48	3 min
	extension	72	3 min
	final extension	72	5 min
mouse GAPDH	RT	42	1 hr
	denature	95	1 min
	annealing	56	2 min
	extension	72	2 min
	final extension	72	5 min
RSV	RT	42	1 hr
	denature	95	1 min
	annealing	50	3 min
	extension	72	3 min
	final extension	72	5 min
influenza A	RT	42	1 hr
	denature	95	1 min
	annealing	55	3 min
	extension	72	3 min
	final extension	72	5 min
influenza B	RT	42	1 hr
	denature	95	1 min
	annealing	61	3 min
	extension	72	3 min
	final extension	72	5 min

Table 8: Thermocycling parameters for microfluidic PCR using our laser platform for 1 µL reaction volumes.

reaction	**step**	*temperature (°C)*	*time (sec)*
λ-phage	initial denature	95	1 min
	denature	95	10 sec
	annealing	68	20 sec
	extension	72	20 sec
	final extension	72	3 min
herpesvirus	initial denature	95	1 min
	denature	95	10 sec
	annealing	48	20 sec
	extension	72	20 sec
	final extension	72	3 min
mouse GAPDH	RT	42	30 min
	initial denature	95	1 min
	denature	93	10 sec
	annealing	56	20 sec
	extension	72	20 sec
influenza A	RT	42	30 min
	initial denature	95	1 min
	denature	95	10 sec
	annealing	55	20 sec
	extension	72	20 sec
	final extension	72	3 min
influenza B	RT	42	30 min
	initial denature	95	1 min
	denature	95	10 sec
	annealing	61	20 sec
	extension	72	20 sec
	final extension	72	3 min

APPENDIX B

PCR PRIMERS

Table 9: Primer sequences for all reactions used in the development of our PCR technologies.

genetic target	primer sequence	
λ-phage	forward:	5'-GATGAGTTCGTGTTCGTACAACTGG-3'
	reverse:	5'-GGTTATCGAAATCAGCCACAGCGCC-3'
herpesviruses	forward:	5'-G(GT)TIGACTTTGCCAGC(TC)T(GC)TACCC-3'
	reverse:	5'-GGGAGTC(AC)GTGTC(GC)CCGTA(GT)ATGA-3'
mouse GAPDH	forward:	5'-GCCTCCCGTGTTCCTACC-3'
	reverse:	5'-GCCTGCTTCACCACCTTC-3'
RSV	forward:	5'-GTCTTACAGCCGTGATTAGG-3'
	reverse:	5'-GGGCTTTCTTTGGTTACTTC-3'
human β-globin	forward:	5'-AACTGTTGGTTTATAGCATTTT-3'
	reverse:	5'-AGGAGCTTATTGATAACTCAGAC-3'
influenza A	forward:	5'-GACCRATCCTGTCACCTCTGAC-3'
	reverse:	5'-AGGGCATTYTGGACAAAKCGTCTA-3'
influenza B	forward:	5'-TCCTCAAYTCACTCTTCGAGCG-3'
	reverse:	5'-CGGTGCTCTTGACCAAATTGG-3'

Note: Primers were purchased in lyophilized form and resuspended to 100 µM to be stored as stock. Dilutions to 20 µM (expect for herpesvirus, which required 50 µM, and GAPDH, which required 10 µM) were then made for preparation of the master mix.

REFERENCES

[1] Rainer, T. H., Cameron, P. A., Smit, D., Ong, K. L., Hung, A. N. W., Nin, D. C. P., Ahuja, A. T., Si, L. C. Y., and Sung, J. J. Y., "Evaluation of WHO criteria for identifying patients with severe acute respiratory syndrome out of hospital: prospective observational study," *BMJ*, vol. 326, pp. 1354–1358, June 2003. Objectives To determine the clinical and radiological features of severe acute respiratory syndrome (SARS) and to evaluate the accuracy of the World Health Organization's guidelines on defining cases of SARS. Design Prospective observational study. Setting A newly set up SARS screening clinic in the emergency department of a university hospital in Hong Kong's New Territories. Participants 556 hospital staff, patients, and relatives who attended the screening clinic and who had had contact with someone with SARS. Main outcome measure Number of confirmed cases of SARS. Results Of the 556 people, 141 were admitted to hospital, and 97 had confirmed SARS. Fever, chills, malaise, myalgia, rigor, loss of appetite, vomiting, diarrhoea, and neck pain but not respiratory tract symptoms were significantly more common among the 97 patients than among the other patients. The overall accuracy of the WHO guidelines for identifying suspected SARS was 83% and their negative predictive value was 86% (95% confidence interval 83% to 89%). They had a sensitivity of 26% (17% to 36%) and a specificity of 96% (93% to 97%). Conclusions Current WHO guidelines for diagnosing suspected SARS may not be sufficiently sensitive in assessing patients before admission to hospital. Daily follow up, evaluation of non-respiratory, systemic symptoms, and chest radiography would be better screening tools.

[2] "Ebola haemorrhagic fever in sudan, 1976," *Bulletin of the World Health Organization*, vol. 56, no. 2, pp. 247–270, 1978.

[3] Leroy, E., Baize, S., Lu, C., McCormick, J., Georges, A., Georges-Courbot, M.-C., Lansoud-Soukate, J., and Fisher-Hoch, S., "Diagnosis of ebola haemorrhagic fever by RT-PCR in an epidemic setting," *Journal of Medical Virology*, vol. 60, pp. 463–467, Apr. 2000.

[4] Elden, L. J. R. v., Kraaij, M. G. J. v., Nijhuis, M., Hendriksen, K. A. W., Dekker, A. W., Rozenberg-Arska, M., and Loon, A. M. v., "Polymerase chain reaction is more sensitive than viral culture and antigen testing for the detection of respiratory viruses in adults with hematological cancer and pneumonia," *Clinical Infectious Diseases*, vol. 34, pp. 177–183, Jan. 2002.

[5] Virolainen, A., Salo, P., Jero, J., Karma, P., Eskola, J., and Leinonen, M., "Comparison of PCR assay with bacterial culture for detecting streptococcus pneumoniae in middle ear fluid of children with acute otitis media.," *Journal of Clinical Microbiology*, vol. 32, pp. 2667–2670, Nov. 1994.

[6] Loeffelholz, M. J., Thompson, C. J., Long, K. S., and Gilchrist, M. J. R., "Comparison of PCR, culture, and direct fluorescent-antibody testing for detection of bordetella pertussis," *Journal of Clinical Microbiology*, vol. 37, pp. 2872–2876, Sept. 1999.

[7] Mullis, K., Faloona, F., Scharf, S., Saiki, R., Horn, G., and Erlich, H., "Specific enzymatic amplification of DNA in vitro: The polymerase chain reaction," *Cold Spring Harbor Symposia on Quantitative Biology*, vol. 51, pp. 263–273, Jan. 1986.

[8] Henderson, D. A., Inglesby, T. V., O'Toole, T., Fine, A., and Layton, M., "Lessons from the west nile viral encephalitis outbreak in new york city, 1999: Implications for bioterrorism preparedness," *Clinical Infectious Diseases*, vol. 32, pp. 277–282, Jan. 2001.

[9] Kim, Y. H., Yang, I., Bae, Y.-S., and Park, S.-R., "Performance evaluation of thermal cyclers for PCR in a rapid cycling condition," *BioTechniques*, vol. 44, pp. 495–496, 498, 500 passim, Apr. 2008.

[10] Yang, I., Kim, Y.-H., Byun, J.-Y., and Park, S.-R., "Use of multiplex polymerase chain reactions to indicate the accuracy of the annealing temperature of thermal cycling," *Analytical Biochemistry*, vol. 338, pp. 192–200, Mar. 2005.

[11] Chamberlain, J. S., Gibbs, R. A., Rainer, J. E., Nguyen, P. N., and Thomas, C., "Deletion screening of the duchenne muscular dystrophy locus via multiplex DNA amplification," *Nucleic Acids Research*, vol. 16, pp. 11141–11156, Dec. 1988.

[12] Edwards, M. C. and Gibbs, R. A., "Multiplex PCR: advantages, development, and applications.," *Genome Research*, vol. 3, pp. S65–S75, Feb. 1994.

[13] Markoulatos, P., Siafakas, N., and Moncany, M., "Multiplex polymerase chain reaction: A practical approach," *Journal of Clinical Laboratory Analysis*, vol. 16, pp. 47–51, Jan. 2002.

[14] Henegariu, O., Heerema, N. A., Dlouhy, S. R., Vance, G. H., and Vogt, P. H., "Multiplex PCR: critical parameters and step-by-step protocol," *BioTechniques*, vol. 23, pp. 504–511, Sept. 1997.

[15] Rose, T. M., Schultz, E. R., Henikoff, J. G., Pietrokovski, S., McCallum, C. M., and Henikoff, S., "Consensus-degenerate hybrid oligonucleotide primers for amplification of distantly related sequences," *Nucleic Acids Research*, vol. 26, pp. 1628–1635, Apr. 1998.

[16] Rose, T. M., Henikoff, J. G., and Henikoff, S., "CODEHOP (COnsensus-DEgenerate hybrid oligonucleotide primer) PCR primer design," *Nucleic Acids Research*, vol. 31, pp. 3763–3766, July 2003.

[17] Tong, S., Chern, S.-W. W., Li, Y., Pallansch, M. A., and Anderson, L. J., "Sensitive and broadly reactive reverse transcription-PCR assays to detect novel paramyxoviruses," *Journal of Clinical Microbiology*, vol. 46, pp. 2652–2658, Aug. 2008.

[18] Kaur, T., Singh, J., Tong, S., Humphrey, C., Clevenger, D., Tan, W., Szekely, B., Wang, Y., Li, Y., Alex Muse, E., Kiyono, M., Hanamura, S., Inoue, E., Nakamura, M., Huffman, M. A., Jiang, B., and Nishida, T., "Descriptive epidemiology of fatal respiratory outbreaks and detection of a human-related metapneumovirus in wild chimpanzees (pan troglodytes) at mahale mountains national park, western tanzania," *American Journal of Primatology*, vol. 70, pp. 755–765, Aug. 2008.

[19] Boyer, L. A., Lee, T. I., Cole, M. F., Johnstone, S. E., Levine, S. S., Zucker, J. P., Guenther, M. G., Kumar, R. M., Murray, H. L., Jenner, R. G., Gifford, D. K., Melton, D. A., Jaenisch, R., and Young, R. A., "Core transcriptional regulatory circuitry in human embryonic stem cells," *Cell*, vol. 122, pp. 947–956, Sept. 2005.

[20] Sperger, J. M., Chen, X., Draper, J. S., Antosiewicz, J. E., Chon, C. H., Jones, S. B., Brooks, J. D., Andrews, P. W., Brown, P. O., and Thomson, J. A., "Gene expression patterns in human embryonic stem cells and human pluripotent germ cell tumors," *Proceedings of the National Academy of Sciences*, vol. 100, pp. 13350–13355, Nov. 2003.

[21] "Making the most of microarrays," *Nature Biotechnology*, vol. 24, pp. 1039–1039, Sept. 2006.

[22] Schena, M., Shalon, D., Davis, R. W., and Brown, P. O., "Quantitative monitoring of gene expression patterns with a complementary DNA microarray," *Science*, vol. 270, pp. 467–470, Oct. 1995.

[23] Liang, P., "MAQC papers over the cracks," *Nature Biotechnology*, vol. 25, pp. 27–28, Jan. 2007.

[24] Spurgeon, S. L., Jones, R. C., and Ramakrishnan, R., "High throughput gene expression measurement with real time PCR in a microfluidic dynamic array," *PLoS ONE*, vol. 3, p. e1662, Feb. 2008.

[25] Itzkovitz, S. and van Oudenaarden, A., "Validating transcripts with probes and imaging technology," *Nature Methods*, vol. 8, pp. S12–S19, Apr. 2011.

[26] Santangelo, P. J., Lifland, A. W., Curt, P., Sasaki, Y., Bassell, G. J., Lindquist, M. E., and Crowe, J. E., "Single moleculesensitive probes for imaging RNA in live cells," *Nature Methods*, vol. 6, pp. 347–349, May 2009.

[27] Bao, G., Rhee, W. J., and Tsourkas, A., "Fluorescent probes for live-cell RNA detection," *Annual review of biomedical engineering*, vol. 11, pp. 25–47, 2009.

[28] Santangelo, P. J., Nix, B., Tsourkas, A., and Bao, G., "Dual FRET molecular beacons for mRNA detection in living cells," *Nucleic Acids Research*, vol. 32, pp. e57–e57, Mar. 2004.

[29] Malone, J. H. and Oliver, B., "Microarrays, deep sequencing and the true measure of the transcriptome," *BMC Biology*, vol. 9, p. 34, May 2011.

[30] Dahl, A., Sultan, M., Jung, A., Schwartz, R., Lange, M., Steinwand, M., Livak, K. J., Lehrach, H., and Nyarsik, L., "Quantitative PCR based expression analysis on a nanoliter scale using polymer nano-well chips," *Biomedical Microdevices*, vol. 9, pp. 307–314, June 2007.

[31] Sanchez-Freire, V., Ebert, A. D., Kalisky, T., Quake, S. R., and Wu, J. C., "Microfluidic single-cell real-time PCR for comparative analysis of gene expression patterns," *Nature Protocols*, vol. 7, pp. 829–838, May 2012.

[32] Stahlberg, A. and Bengtsson, M., "Single-cell gene expression profiling using reverse transcription quantitative real-time PCR," *Methods*, vol. 50, pp. 282–288, Apr. 2010.

[33] White, A. K., VanInsberghe, M., Petriv, O. I., Hamidi, M., Sikorski, D., Marra, M. A., Piret, J., Aparicio, S., and Hansen, C. L., "High-throughput microfluidic single-cell RT-qPCR," *Proceedings of the National Academy of Sciences*, vol. 108, pp. 13999–14004, Aug. 2011.

[34] Zare, R. N. and Kim, S., "Microfluidic platforms for single-cell analysis," *Annual Review of Biomedical Engineering*, vol. 12, no. 1, pp. 187–201, 2010.

[35] Zeng, Y., Novak, R., Shuga, J., Smith, M. T., and Mathies, R. A., "High-performance single cell genetic analysis using microfluidic emulsion generator arrays," *Analytical Chemistry*, vol. 82, pp. 3183–3190, Apr. 2010.

[36] Zhong, J. F., Chen, Y., Marcus, J. S., Scherer, A., Quake, S. R., Taylor, C. R., and Weiner, L. P., "A microfluidic processor for gene expression profiling of single human embryonic stem cells," *Lab on a Chip*, vol. 8, pp. 68–74, Dec. 2007.

[37] Zhong, J., Feng, Y., and Taylor, C., "Microfluidic devices for investigating stem cell gene regulation via single-cell analysis," *Current Medicinal Chemistry*, vol. 15, pp. 2897–2900, Dec. 2008.

[38] Cao, Q., Mahalanabis, M., Chang, J., Carey, B., Hsieh, C., Stanley, A., Odell, C. A., Mitchell, P., Feldman, J., Pollock, N. R., and Klapperich, C. M., "Microfluidic chip for molecular amplification of influenza a RNA in human respiratory specimens," *PLoS ONE*, vol. 7, Mar. 2012.

[39] Easley, C. J., Karlinsey, J. M., Bienvenue, J. M., Legendre, L. A., Roper, M. G., Feldman, S. H., Hughes, M. A., Hewlett, E. L., Merkel, T. J., Ferrance, J. P., and Landers, J. P., "A fully integrated microfluidic genetic analysis system with sample-inanswer-out capability," *Proceedings of the National Academy of Sciences*, vol. 103, pp. 19272–19277, Dec. 2006.

[40] Kaigala, G. V., Hoang, V. N., Stickel, A., Lauzon, J., Manage, D., Pilarski, L. M., and Backhouse, C. J., "An inexpensive and portable microchip-based platform for integrated RTPCR and capillary electrophoresis," *Analyst*, vol. 133, pp. 331–338, Feb. 2008.

[41] Lien, K.-Y., Lee, W.-C., Lei, H.-Y., and Lee, G.-B., "Integrated reverse transcription polymerase chain reaction systems for virus detection," *Biosensors and Bioelectronics*, vol. 22, pp. 1739–1748, Mar. 2007.

[42] Liu, P., Seo, T. S., Beyor, N., Shin, K.-J., Scherer, J. R., and Mathies, R. A., "Integrated portable polymerase chain reaction-capillary electrophoresis microsystem for rapid forensic short tandem repeat typing," *Analytical Chemistry*, vol. 79, pp. 1881–1889, Mar. 2007.

[43] Woolley, A. T., Hadley, D., Landre, P., deMello, A. J., Mathies, R. A., and Northrup, M. A., "Functional integration of PCR amplification and capillary electrophoresis in a microfabricated DNA analysis device," *Analytical Chemistry*, vol. 68, pp. 4081–4086, Dec. 1996.

[44] Warren, L., Bryder, D., Weissman, I. L., and Quake, S. R., "Transcription factor profiling in individual hematopoietic progenitors by digital RT-PCR," *Proceedings of the National Academy of Sciences*, vol. 103, pp. 17807–17812, Nov. 2006.

[45] Lopez-Maury, L., Marguerat, S., and Bhler, J., "Tuning gene expression to changing environments: from rapid responses to evolutionary adaptation," *Nature Reviews Genetics*, vol. 9, pp. 583–593, Aug. 2008.

[46] Yosef, N. and Regev, A., "Impulse control: Temporal dynamics in gene transcription," *Cell*, vol. 144, pp. 886–896, Mar. 2011.

[47] Yang, S. and Rothman, R. E., "PCR-based diagnostics for infectious diseases: uses, limitations, and future applications in acute-care settings," *The Lancet Infectious Diseases*, vol. 4, pp. 337–348, June 2004.

[48] Louie, M., Louie, L., and Simor, A. E., "The role of DNA amplification technology in the diagnosis of infectious diseases," *Canadian Medical Association Journal*, vol. 163, pp. 301–309, Aug. 2000.

[49] Nakane, J., Broemeling, D., Donaldson, R., Marziali, A., Willis, T. D., O'Keefe, M., and Davis, R. W., "A method for parallel, automated, thermal cycling of submicroliter samples," *Genome Research*, vol. 11, pp. 441–447, Mar. 2001.

[50] Salas-Solano, O., Ruiz-Martinez, M. C., Carrilho, E., Kotler, L., and Karger, B. L., "A sample purification method for rugged and high-performance DNA sequencing by capillary electrophoresis using replaceable polymer solutions. b. quantitative determination of the role of sample matrix components on sequencing analysis," *Analytical Chemistry*, vol. 70, pp. 1528–1535, Apr. 1998.

[51] Wittwer, C. T., Fillmore, G. C., and Hillyard, D. R., "Automated polymerase chain reaction in capillary tubes with hot air," *Nucleic Acids Research*, vol. 17, pp. 4353–4357, June 1989.

[52] Wilding, P., Shoffner, M. A., and Kricka, L. J., "PCR in a silicon microstructure.," *Clinical Chemistry*, vol. 40, pp. 1815–1818, Sept. 1994.

[53] Burns, M. A., Johnson, B. N., Brahmasandra, S. N., Handique, K., Webster, J. R., Krishnan, M., Sammarco, T. S., Man, P. M., Jones, D., Heldsinger, D., Mastrangelo, C. H., and Burke, D. T., "An integrated nanoliter DNA analysis device," *Science*, vol. 282, pp. 484–487, Oct. 1998.

[54] Zhang, C., Xu, J., Ma, W., and Zheng, W., "PCR microfluidic devices for DNA amplification," *Biotechnology Advances*, vol. 24, pp. 243–284, May 2006.

[55] Zhang, Y. and Ozdemir, P., "Microfluidic DNA amplificationa review," *Analytica Chimica Acta*, vol. 638, pp. 115–125, Apr. 2009.

[56] Wittwer, C. T. and Garling, D. J., "Rapid cycle DNA amplification: time and temperature optimization," *BioTechniques*, vol. 10, pp. 76–83, Jan. 1991.

[57] Cady, N. C., Stelick, S., Kunnavakkam, M. V., and Batt, C. A., "Real-time PCR detection of listeria monocytogenes using an integrated microfluidics platform," *Sensors and Actuators B: Chemical*, vol. 107, pp. 332–341, May 2005.

[58] Hou, C.-S. J., Godin, M., Payer, K., Chakrabarti, R., and Manalis, S. R., "Integrated microelectronic device for label-free nucleic acid amplification and detection," *Lab on a Chip*, vol. 7, pp. 347–354, Mar. 2007.

[59] Belgrader, P., Young, S., Yuan, B., Primeau, M., Christel, L. A., Pourahmadi, F., and Northrup, M. A., "A battery-powered notebook thermal cycler for rapid multiplex real-time PCR analysis," *Analytical Chemistry*, vol. 73, pp. 286–289, Jan. 2001.

[60] Liu, P., Yeung, S. H. I., Crenshaw, K. A., Crouse, C. A., Scherer, J. R., and Mathies, R. A., "Real-time forensic DNA analysis at a crime scene using a portable microchip analyzer," *Forensic Science International: Genetics*, vol. 2, pp. 301–309, Sept. 2008.

[61] Neuil, P., Campos, C. D. M., Wong, C. C., Soon, J. B. W., Reboud, J., and Manz, A., "From chip-in-a-lab to lab-on-a-chip: towards a single handheld electronic system for multiple application-specific lab-on-a-chip (ASLOC)," *Lab on a Chip*, vol. 14, pp. 2168–2176, June 2014.

[62] Liu, C. N., Toriello, N. M., and Mathies, R. A., "Multichannel PCR-CE microdevice for genetic analysis," *Analytical Chemistry*, vol. 78, pp. 5474–5479, Aug. 2006.

[63] Giordano, B. C., Copeland, E. R., and Landers, J. P., "Towards dynamic coating of glass microchip chambers for amplifying DNA via the polymerase chain reaction," *ELECTROPHORESIS*, vol. 22, pp. 334–340, Jan. 2001.

[64] Focke, M., Stumpf, F., Faltin, B., Reith, P., Bamarni, D., Wadle, S., Mller, C., Reinecke, H., Schrenzel, J., Francois, P., Mark, D., Roth, G., Zengerle, R., and Stetten, F. v., "Microstructuring of polymer films for sensitive genotyping by real-time PCR on a centrifugal microfluidic platform," *Lab on a Chip*, vol. 10, pp. 2519–2526, Sept. 2010.

[65] Becker, H. and Grtner, C., "Polymer microfabrication technologies for microfluidic systems," *Analytical and Bioanalytical Chemistry*, vol. 390, pp. 89–111, Jan. 2008.

[66] Yu, X., Zhang, D., Li, T., Hao, L., and Li, X., "3-d microarrays biochip for DNA amplification in polydimethylsiloxane (PDMS) elastomer," *Sensors and Actuators A: Physical*, vol. 108, pp. 103–107, Nov. 2003.

[67] Yang, J., Liu, Y., Rauch, C. B., Stevens, R. L., Liu, R. H., Lenigk, R., and Grodzinski, P., "High sensitivity PCR assay in plastic micro reactors," *Lab on a Chip*, vol. 2, pp. 179–187, Nov. 2002.

[68] Angione, S. L., Chauhan, A., and Tripathi, A., "Real-time droplet DNA amplification with a new tablet platform," *Analytical Chemistry*, vol. 84, pp. 2654–2661, Mar. 2012.

[69] Hua, Z., Rouse, J. L., Eckhardt, A. E., Srinivasan, V., Pamula, V. K., Schell, W. A., Benton, J. L., Mitchell, T. G., and Pollack, M. G., "Multiplexed real-time polymerase chain reaction on a digital microfluidic platform," *Analytical Chemistry*, vol. 82, pp. 2310–2316, Mar. 2010.

[70] Wang, F. and Burns, M. A., "Performance of nanoliter-sized droplet-based microfluidic PCR," *Biomedical Microdevices*, vol. 11, pp. 1071–1080, Oct. 2009.

[71] Giordano, B. C., Ferrance, J., Swedberg, S., Hhmer, A. F. R., and Landers, J. P., "Polymerase chain reaction in polymeric microchips: DNA amplification in less than 240 seconds," *Analytical Biochemistry*, vol. 291, pp. 124–132, Apr. 2001.

[72] Slyadnev, M. N., Lavrova, M. V., Erkin, M. A., Kazakov, V. A., and Ganeev, A. A., "Development of a multireactor microfluidic system for the determination of DNA using real-time polymerase chain reaction," *Journal of Analytical Chemistry*, vol. 63, pp. 192–198, Feb. 2008.

[73] Liao, C.-S., Lee, G.-B., Liu, H.-S., Hsieh, T.-M., and Luo, C.-H., "Miniature RTPCR system for diagnosis of RNA-based viruses," *Nucleic Acids Research*, vol. 33, pp. e156–e156, Jan. 2005.

[74] Agrawal, N., Hassan, Y., and Ugaz, V., "A pocket-sized convective PCR thermocycler," *Angewandte Chemie International Edition*, vol. 46, pp. 4316–4319, June 2007.

[75] Wittwer, C. T., Ririe, K. M., Andrew, R. V., David, D. A., Gundry, R. A., and Balis, U. J., "The LightCycler: a microvolume multisample fluorimeter with rapid temperature control," *BioTechniques*, vol. 22, pp. 176–181, Jan. 1997.

[76] Huhmer, A. F. R. and Landers, J. P., "Noncontact infrared-mediated thermocycling for effective polymerase chain reaction amplification of DNA in nanoliter volumes," *Analytical Chemistry*, vol. 72, pp. 5507–5512, Nov. 2000.

[77] Terazono, H., Hattori, A., Takei, H., Takeda, K., and Yasuda, K., "Development of 1480 nm photothermal high-speed real-time polymerase chain reaction system for rapid nucleotide recognition," *Japanese Journal of Applied Physics*, vol. 47, p. 5212, June 2008.

[78] Braun, D., Goddard, N. L., and Libchaber, A., "Exponential DNA replication by laminar convection," *Physical Review Letters*, vol. 91, p. 158103, Oct. 2003.

[79] Quinto-Su, P. A., Lai, H.-H., Yoon, H. H., Sims, C. E., Allbritton, N. L., and Venugopalan, V., "Examination of laser microbeam cell lysis in a PDMS microfluidic channel using time-resolved imaging," *Lab on a Chip*, vol. 8, no. 3, p. 408, 2008.

[80] Abi-Samra, K., Hanson, R., Madou, M., and Iii, R. A. G., "Infrared controlled waxes for liquid handling and storage on a CD-microfluidic platform," *Lab on a Chip*, vol. 11, pp. 723–726, Jan. 2011.

[81] Braun, D. and Libchaber, A., "Trapping of DNA by thermophoretic depletion and convection," *Physical Review Letters*, vol. 89, p. 188103, Oct. 2002.

[82] Duhr, S., Arduini, S., and Braun, D., "Thermophoresis of DNA determined by microfluidic fluorescence," *The European Physical Journal E*, vol. 15, pp. 277–286, Nov. 2004.

[83] Oda, R. P., Strausbauch, M. A., Huhmer, A. F. R., Borson, N., Jurrens, S. R., Craighead, J., Wettstein, P. J., Eckloff, B., Kline, B., and Landers, J. P., "Infrared-mediated thermocycling for ultrafast polymerase chain reaction amplification of DNA," *Analytical Chemistry*, vol. 70, pp. 4361–4368, Oct. 1998.

[84] Kim, H., Vishniakou, S., and Faris, G. W., "Petri dish PCR: laser-heated reactions in nanoliter droplet arrays," *Lab on a Chip*, vol. 9, pp. 1230–1235, May 2009.

[85] Slyadnev, M. N., Tanaka, Y., Tokeshi, M., and Kitamori, T., "Photothermal temperature control of a chemical reaction on a microchip using an infrared diode laser," *Analytical Chemistry*, vol. 73, pp. 4037–4044, Aug. 2001.

[86] Roper, M. G., Easley, C. J., Legendre, L. A., Humphrey, J. A. C., and Landers, J. P., "Infrared temperature control system for a completely noncontact polymerase chain reaction in microfluidic chips," *Analytical Chemistry*, vol. 79, pp. 1294–1300, Feb. 2007.

[87] Saunders, D. C., Holst, G. L., Phaneuf, C. R., Pak, N., Marchese, M., Sondej, N., McKinnon, M., and Forest, C. R., "Rapid, quantitative, reverse transcription PCR in a polymer microfluidicchip," *Biosensors and Bioelectronics*, vol. 44, pp. 222–228, June 2013.

[88] Liu, R. H., Yang, J., Lenigk, R., Bonanno, J., and Grodzinski, P., "Self-contained, fully integrated biochip for sample preparation, polymerase chain reaction amplification, and DNA microarray detection," *Analytical Chemistry*, vol. 76, pp. 1824–1831, Apr. 2004.

[89] Yeung, S.-W., Lee, T. M.-H., Cai, H., and Hsing, I.-M., "A DNA biochip for on-the-spot multiplexed pathogen identification," *Nucleic Acids Research*, vol. 34, pp. e118–e118, Oct. 2006.

[90] Chow, A. W., "Protein separations," in *Microchip Capillary Electrophoresis* (Henry, C. S., ed.), no. 339 in Methods in Molecular Biology, pp. 145–158, Humana Press, Jan. 2006.

[91] Li, S., Anderson, L. M., Yang, J.-M., Lin, L., and Yang, H., "DNA transformation via local heat shock," *Applied Physics Letters*, vol. 91, p. 013902, July 2007.

[92] Murphy, K. C. and Campellone, K. G., "Lambda red-mediated recombinogenic engineering of enterohemorrhagic and enteropathogenic e. coli," *BMC Molecular Biology*, vol. 4, p. 11, Dec. 2003.

[93] Tanaka, Y., Slyadnev, M. N., Hibara, A., Tokeshi, M., and Kitamori, T., "Non-contact photothermal control of enzyme reactions on a microchip by using a compact diode laser," *Journal of Chromatography A*, vol. 894, pp. 45–51, Oct. 2000.

[94] Easley, C. J., Humphrey, J. A. C., and Landers, J. P., "Thermal isolation of microchip reaction chambers for rapid non-contact DNA amplification," *Journal of Micromechanics and Microengineering*, vol. 17, p. 1758, Sept. 2007.

[95] Kelly, R. T. and Woolley, A. T., "Thermal bonding of polymeric capillary electrophoresis microdevices in water," *Analytical Chemistry*, vol. 75, pp. 1941–1945, Apr. 2003.

[96] Assael, M. J., Botsios, S., Gialou, K., and Metaxa, I. N., "Thermal conductivity of polymethyl methacrylate (PMMA) and borosilicate crown glass BK7," *International Journal of Thermophysics*, vol. 26, pp. 1595–1605, Sept. 2005.

[97] Kibbe, W. A., "OligoCalc: an online oligonucleotide properties calculator," *Nucleic Acids Research*, vol. 35, pp. W43–W46, July 2007.

[98] Forest, C. R., Saez, M. A., and Hunter, I. W., "Microforging technique for rapid, low-cost fabrication of lens array molds," *Applied Optics*, vol. 46, pp. 8668–8673, Dec. 2007.

[99] Khashan, M. A. and Nassif, A. Y., "Dispersion of the optical constants of quartz and polymethyl methacrylate glasses in a wide spectral range: 0.23 m," *Optics Communications*, vol. 188, pp. 129–139, Feb. 2001.

[100] Waters, L. C., Jacobson, S. C., Kroutchinina, N., Khandurina, J., Foote, R. S., and Ramsey, J. M., "Microchip device for cell lysis, multiplex PCR amplification, and electrophoretic sizing," *Analytical Chemistry*, vol. 70, pp. 158–162, Jan. 1998.

[101] Liu, J., Enzelberger, M., and Quake, S., "A nanoliter rotary device for polymerase chain reaction," *ELECTROPHORESIS*, vol. 23, pp. 1531–1536, May 2002.

[102] Ranjit Prakash, A., Adamia, S., Sieben, V., Pilarski, P., Pilarski, L. M., and Backhouse, C. J., "Small volume PCR in PDMS biochips with integrated fluid control and vapour barrier," *Sensors and Actuators B: Chemical*, vol. 113, pp. 398–409, Jan. 2006.

[103] Sun, Y. and Kwok, Y. C., "Polymeric microfluidic system for DNA analysis," *Analytica Chimica Acta*, vol. 556, pp. 80–96, Jan. 2006.

[104] Ziaie, B., Baldi, A., Lei, M., Gu, Y., and Siegel, R. A., "Hard and soft micromachining for BioMEMS: review of techniques and examples of applications in microfluidics and drug delivery," *Advanced Drug Delivery Reviews*, vol. 56, pp. 145–172, Feb. 2004.

[105] Xia, Y. and Whitesides, G. M., "Soft lithography," *Annual Review of Materials Science*, vol. 28, no. 1, pp. 153–184, 1998.

[106] Manz, A., Fettinger, J. C., Verpoorte, E., Ldi, H., Widmer, H. M., and Harrison, D. J., "Micromachining of monocrystalline silicon and glass for chemical analysis systems a look into next century's technology or just a fashionable craze?," *TrAC Trends in Analytical Chemistry*, vol. 10, pp. 144–149, May 1991.

[107] Lucio do Lago, C., Torres da Silva, H. D., Neves, C. A., Alves Brito-Neto, J. G., and Fracassi da Silva, J. A., "A dry process for production of microfluidic devices based on the lamination of laser-printed polyester films," *Analytical Chemistry*, vol. 75, pp. 3853–3858, Aug. 2003.

[108] Tomazelli Coltro, W. K., Fracassi da Silva, J. A., Torres da Silva, H. D., Richter, E. M., Furlan, R., Angnes, L., do Lago, C. L., Mazo, L. H., and Carrilho, E., "Electrophoresis microchip fabricated by a direct-printing process with end-channel amperometric detection," *ELECTROPHORESIS*, vol. 25, pp. 3832–3839, Nov. 2004.

[109] Liu, A.-l., He, F.-y., Wang, K., Zhou, T., Lu, Y., and Xia, X.-h., "Rapid method for design and fabrication of passive micromixers in microfluidic devices using a direct-printing process," *Lab on a Chip*, vol. 5, pp. 974–978, Aug. 2005.

[110] Cheng, J.-Y., Wei, C.-W., Hsu, K.-H., and Young, T.-H., "Direct-write laser micromachining and universal surface modification of PMMA for device development," *Sensors and Actuators B: Chemical*, vol. 99, pp. 186–196, Apr. 2004.

[111] McCormick, R. M., Nelson, R. J., Alonso-Amigo, M. G., Benvegnu, D. J., and Hooper, H. H., "Microchannel electrophoretic separations of DNA in injection-molded plastic substrates," *Analytical Chemistry*, vol. 69, pp. 2626–2630, July 1997.

[112] Ford, S. M., Kar, B., Mcwhorter, S., Davies, J., Soper, S. A., Klopf, M., Calderon, G., and Saile, V., "Microcapillary electrophoresis devices fabricated using polymeric substrates and x-ray lithography," *Journal of Microcolumn Separations*, vol. 10, pp. 413–422, Jan. 1998.

[113] Mathur, A., Roy, S. S., Tweedie, M., Mukhopadhyay, S., Mitra, S. K., and McLaughlin, J. A., "Characterisation of PMMA microfluidic channels and devices fabricated by hot embossing and sealed by direct bonding," *Current Applied Physics*, vol. 9, pp. 1199–1202, Nov. 2009.

[114] Lee, G.-B., Chen, S.-H., Huang, G.-R., Sung, W.-C., and Lin, Y.-H., "Microfabricated plastic chips by hot embossing methods and their applications for DNA separation and detection," *Sensors and Actuators B: Chemical*, vol. 75, pp. 142–148, Apr. 2001.

[115] Koerner, T., Brown, L., Xie, R., and Oleschuk, R. D., "Epoxy resins as stamps for hot embossing of microstructures and microfluidic channels," *Sensors and Actuators B: Chemical*, vol. 107, pp. 632–639, June 2005.

[116] Becker, H. and Heim, U., "Hot embossing as a method for the fabrication of polymer high aspect ratio structures," *Sensors and Actuators A: Physical*, vol. 83, pp. 130–135, May 2000.

[117] Rainelli, A., Stratz, R., Schweizer, K., and Hauser, P. C., "Miniature flow-injection analysis manifold created by micromilling," *Talanta*, vol. 61, pp. 659–665, Dec. 2003.

[118] Pak, N., Saunders, D. C., Phaneuf, C. R., and Forest, C. R., "Plug-and-play, infrared, laser-mediated PCR in a microfluidic chip," *Biomedical Microdevices*, vol. 14, pp. 427–433, Apr. 2012.

[119] Sodemann, A. A. and Rhett, J., M., "Parametric investigation of precision in tool-workpiece conductivity touch-off method in micromilling," *Transactions of the North American Research Institution of SME*, vol. 37, pp. 565–572, 2009.

[120] Scherag, F. D., Brandstetter, T., and Rhe, J., "Raising the shields: PCR in the presence of metallic surfaces protected by tailor-made coatings," *Colloids and Surfaces B: Biointerfaces*, vol. 122, pp. 576–582, Oct. 2014.

[121] Unger, M. A., Chou, H.-P., Thorsen, T., Scherer, A., and Quake, S. R., "Monolithic microfabricated valves and pumps by multilayer soft lithography," *Science*, vol. 288, pp. 113–116, Apr. 2000.

[122] Sung, J. H. and Shuler, M. L., "Prevention of air bubble formation in a microfluidic perfusion cell culture system using a microscale bubble trap," *Biomedical Microdevices*, vol. 11, pp. 731–738, Aug. 2009.

[123] Zheng, W., Wang, Z., Zhang, W., and Jiang, X., "A simple PDMS-based microfluidic channel design that removes bubbles for long-term on-chip culture of mammalian cells," *Lab on a Chip*, vol. 10, pp. 2906–2910, Nov. 2010.

[124] Yang, Z., Matsumoto, S., and Maeda, R., "A prototype of ultrasonic micro-degassing device for portable dialysis system," *Sensors and Actuators A: Physical*, vol. 95, pp. 274–280, Jan. 2002.

[125] Kohlheyer, D., Eijkel, J. C. T., Schlautmann, S., van den Berg, A., and Schasfoort, R. B. M., "Bubble-free operation of a microfluidic free-flow electrophoresis chip with integrated pt electrodes," *Analytical Chemistry*, vol. 80, pp. 4111–4118, June 2008.

[126] Taylor, T. B., Winn-Deen, E. S., Picozza, E., Woudenberg, T. M., and Albin, M., "Optimization of the performance of the polymerase chain reaction in silicon-based microstructures," *Nucleic Acids Research*, vol. 25, pp. 3164–3168, Aug. 1997.

[127] Panaro, N. J., Lou, X. J., Fortina, P., Kricka, L. J., and Wilding, P., "Surface effects on PCR reactions in multichip microfluidic platforms," *Biomedical Microdevices*, vol. 6, pp. 75–80, Mar. 2004.

[128] Prakash, A. R., Amrein, M., and Kaler, K. V. I. S., "Characteristics and impact of taq enzyme adsorption on surfaces in microfluidic devices," *Microfluidics and Nanofluidics*, vol. 4, pp. 295–305, Apr. 2008.

[129] Kodzius, R., Xiao, K., Wu, J., Yi, X., Gong, X., Foulds, I. G., and Wen, W., "Inhibitory effect of common microfluidic materials on PCR outcome," *Sensors and Actuators B: Chemical*, vol. 161, pp. 349–358, Jan. 2012.

[130] Shoffner, M. A., Cheng, J., Hvichia, G. E., Kricka, L. J., and Wilding, P., "Chip PCR. i. surface passivation of microfabricated silicon-glass chips for PCR," *Nucleic Acids Research*, vol. 24, pp. 375–379, Jan. 1996.

[131] Sweryda-Krawiec, B., Devaraj, H., Jacob, G., and Hickman, J. J., "A new interpretation of serum albumin surface passivation," *Langmuir*, vol. 20, pp. 2054–2056, Mar. 2004.

[132] Erill, I., Campoy, S., Erill, N., Barb, J., and Aguil, J., "Biochemical analysis and optimization of inhibition and adsorption phenomena in glasssilicon PCR-chips," *Sensors and Actuators B: Chemical*, vol. 96, pp. 685–692, Dec. 2003.

[133] Christensen, T. B., Pedersen, C. M., Grndahl, K. G., Jensen, T. G., Sekulovic, A., Bang, D. D., and Wolff, A., "PCR biocompatibility of lab-on-a-chip and MEMS materials," *Journal of Micromechanics and Microengineering*, vol. 17, p. 1527, Aug. 2007.

[134] Kolari, K., Satokari, R., Kataja, K., Stenman, J., and Hokkanen, A., "Real-time analysis of PCR inhibition on microfluidic materials," *Sensors and Actuators B: Chemical*, vol. 128, pp. 442–449, Jan. 2008.

[135] Gonzalez, A., Grimes, R., Walsh, E. J., Dalton, T., and Davies, M., "Interaction of quantitative PCR components with polymeric surfaces," *Biomedical Microdevices*, vol. 9, pp. 261–266, Apr. 2007.

[136] Elbert, D. L. and Hubbell, J. A., "Surface treatments of polymers for biocompatibility," *Annual Review of Materials Science*, vol. 26, no. 1, pp. 365–394, 1996.

[137] Koutsopoulos, S., van der Oost, J., and Norde, W., "Adsorption of an endoglucanase from the hyperthermophilic pyrococcus furiosus on hydrophobic (polystyrene) and hydrophilic (silica) surfaces increases protein heat stability," *Langmuir*, vol. 20, pp. 6401–6406, July 2004.

[138] Orasanu-Gourlay, A. and Bradley, R., "Protein adsorption by basal plane graphite surfaces: Molecular images and nano-structured films," *Adsorption Science & Technology*, vol. 24, pp. 117–130, Mar. 2006.

[139] Pancera, S. M. and Petri, D. F. S., "Formation of enzymatic biofilms on polymer films and on silicon wafers," in *Molecular crystals and liquid crystals science and technology. Section A, Molecular crystals and liquid crystals*, vol. 374, pp. 611–616, Gordon and Breach, 2002.

[140] Noinville, S., Revault, M., and Baron, M.-H., "Conformational changes of enzymes adsorbed at liquid solid interface: Relevance to enzymatic activity," *Biopolymers*, vol. 67, pp. 323–326, Jan. 2002.

[141] Assis, O. B. G., "Scanning electron microscopy study of protein immobilized on SIO2 sol-gel surfaces," *Brazilian Journal of Chemical Engineering*, vol. 20, pp. 339–342, Sept. 2003.

[142] Haynes, C. A., Sliwinsky, E., and Norde, W., "Structural and electrostatic properties of globular proteins at a polystyrene-water interface," *Journal of Colloid and Interface Science*, vol. 164, pp. 394–409, May 1994.

[143] Yoon, J.-Y. and Garrell, R. L., "Preventing biomolecular adsorption in electrowetting-based biofluidic chips," *Analytical Chemistry*, vol. 75, pp. 5097–5102, Oct. 2003.

[144] Haynes, C. A. and Norde, W., "Structures and stabilities of adsorbed proteins," *Journal of Colloid and Interface Science*, vol. 169, pp. 313–328, Feb. 1995.

[145] Norde Willem and Haynes Charles A., "Reversibility and the mechanism of protein adsorption," in *Proteins at Interfaces II*, vol. 602 of *ACS Symposium Series*, pp. 26–40, American Chemical Society, May 1995.

[146] Beverung, C. J., Radke, C. J., and Blanch, H. W., "Protein adsorption at the oil/water interface: characterization of adsorption kinetics by dynamic interfacial tension measurements," *Biophysical Chemistry*, vol. 81, pp. 59–80, Sept. 1999.

[147] Luk, Y.-Y., Kato, M., and Mrksich, M., "Self-assembled monolayers of alkanethiolates presenting mannitol groups are inert to protein adsorption and cell attachment," *Langmuir*, vol. 16, pp. 9604–9608, Nov. 2000.

[148] Moskovitz, Y. and Srebnik, S., "Mean-field model of immobilized enzymes embedded in a grafted polymer layer," *Biophysical Journal*, vol. 89, pp. 22–31, July 2005.

[149] Sofia, S. J., Premnath, V., and Merrill, E. W., "Poly(ethylene oxide) grafted to silicon surfaces: Grafting density and protein adsorption," *Macromolecules*, vol. 31, pp. 5059–5070, July 1998.

[150] Beer, N. R., Hindson, B. J., Wheeler, E. K., Hall, S. B., Rose, K. A., Kennedy, I. M., and Colston, B. W., "On-chip, real-time, single-copy polymerase chain reaction in picoliter droplets," *Analytical Chemistry*, vol. 79, pp. 8471–8475, Nov. 2007.

[151] Liu, Y., Rauch, C. B., Stevens, R. L., Lenigk, R., Yang, J., Rhine, D. B., and Grodzinski, P., "DNA amplification and hybridization assays in integrated plastic monolithic devices," *Analytical Chemistry*, vol. 74, pp. 3063–3070, July 2002.

[152] Gulley, M. L. and Tang, W., "Using epstein-barr viral load assays to diagnose, monitor, and prevent posttransplant lymphoproliferative disorder," *Clinical Microbiology Reviews*, vol. 23, pp. 350–366, Apr. 2010.

[153] Martinez, O. M. and De Gruijl, F. R., "Molecular and immunologic mechanisms of cancer pathogenesis in solid organ transplant recipients," *American Journal of Transplantation*, vol. 8, pp. 2205–2211, Nov. 2008.

[154] Snow, A. L. and Martinez, O. M., "Epstein-barr virus: Evasive maneuvers in the development of PTLD," *American Journal of Transplantation*, vol. 7, pp. 271–277, Feb. 2007.

[155] Wagner, H. J., Wessel, M., Jabs, W., Smets, F., Fischer, L., Offner, G., and Bucsky, P., "Patients at risk for development of posttransplant lymphoproliferative disorder: plasma versus peripheral blood mononuclear cells as material for quantification of epstein-barr viral load by using real-time quantitative polymerase chain reaction," *Transplantation*, vol. 72, pp. 1012–1019, Sept. 2001.

[156] Arya, M., Shergill, I. S., Williamson, M., Gommersall, L., Arya, N., and Patel, H. R., "Basic principles of real-time quantitative PCR," *Expert Review of Molecular Diagnostics*, vol. 5, pp. 209–219, Mar. 2005.

[157] Kirby, B. J., *Micro- and Nanoscale Fluid Mechanics: Transport in Microfluidic Devices*. Cambridge University Press, July 2010.

[158] Duarte, G. R. M., Price, C. W., Augustine, B. H., Carrilho, E., and Landers, J. P., "Dynamic solid phase DNA extraction and PCR amplification in polyester-toner based microchip," *Analytical Chemistry*, vol. 83, pp. 5182–5189, July 2011.

[159] Li, X.-J. J. and Zhou, Y., *Microfluidic Devices for Biomedical Applications*. Elsevier, Oct. 2013.

[160] Kim, K., Park, S. W., and Yang, S. S., "The optimization of PDMS-PMMA bonding process using silane primer," *BioChip Journal*, vol. 4, pp. 148–154, June 2010.

[161] Long, T. M., Prakash, S., Shannon, M. A., and Moore, J. S., "Water-vapor plasma-based surface activation for trichlorosilane modification of PMMA," *Langmuir*, vol. 22, pp. 4104–4109, Apr. 2006.

[162] Popat, K. C., Johnson, R. W., and Desai, T. A., "Vapor deposited poly(ethylene glycol) films for surface modification of microfluidic systems," *Journal of the Association for Laboratory Automation*, vol. 7, pp. 65–67, June 2002.

[163] Kreader, C. A., "Relief of amplification inhibition in PCR with bovine serum albumin or t4 gene 32 protein.," *Applied and Environmental Microbiology*, vol. 62, pp. 1102–1106, Mar. 1996.

[164] Jeyachandran, Y. L., Mielczarski, E., Rai, B., and Mielczarski, J. A., "Quantitative and qualitative evaluation of adsorption/desorption of bovine serum albumin on hydrophilic and hydrophobic surfaces," *Langmuir*, vol. 25, pp. 11614–11620, Oct. 2009.

[165] Wittwer, C. T., Fillmore, G. C., and Garling, D. J., "Minimizing the time required for DNA amplification by efficient heat transfer to small samples," *Analytical Biochemistry*, vol. 186, pp. 328–331, May 1990.

[166] Motosuke, M., Akutsu, D., and Honami, S., "Temperature measurement of microfluids with high temporal resolution by laser-induced fluorescence," *Journal of Mechanical Science and Technology*, vol. 23, pp. 1821–1828, July 2009.

[167] Innis, M. A., Gelfand, D. H., and Sninsky, J. J., *PCR Applications: Protocols for Functional Genomics*. Academic Press, May 1999.

[168] Oosterbroek, E. and Berg, A. v. d., *Lab-on-a-Chip: Miniaturized Systems for (Bio)Chemical Analysis and Synthesis*. Elsevier, Oct. 2003.

[169] Phaneuf, C. R., Oh, K., Pak, N., Saunders, D. C., Conrardy, C., Landers, J. P., Tong, S., and Forest, C. R., "Sensitive, microliter PCR with consensus degenerate primers for epstein barr virus amplification," *Biomedical Microdevices*, vol. 15, pp. 221–231, Apr. 2013.

[170] Lee, D., Chen, P.-J., and Lee, G.-B., "The evolution of real-time PCR machines to real-time PCR chips," *Biosensors and Bioelectronics*, vol. 25, pp. 1820–1824, Mar. 2010.

[171] van Pelt-Verkuil, E., van Belkum, A., and Hays, J. P., *Principles and Technical Aspects of PCR Amplifi cation*. Springer, 2008.

[172] Schefe, J. H., Lehmann, K. E., Buschmann, I. R., Unger, T., and Funke-Kaiser, H., "Quantitative real-time RT-PCR data analysis: current concepts and the novel gene expressions c t difference formula," *Journal of Molecular Medicine*, vol. 84, pp. 901–910, Nov. 2006.

[173] Tichopad, A., Dilger, M., Schwarz, G., and Pfaffl, M. W., "Standardized determination of realtime PCR efficiency from a single reaction setup," *Nucleic Acids Research*, vol. 31, pp. e122–e122, Oct. 2003.

[174] Zhang, C. and Xing, D., "Miniaturized PCR chips for nucleic acid amplification and analysis: latest advances and future trends," *Nucleic Acids Research*, vol. 35, pp. 4223–4237, July 2007.

[175] Yu, Y., Li, B., Baker, C. A., Zhang, X., and Roper, M. G., "Quantitative polymerase chain reaction using infrared heating on a microfluidic chip," *Analytical Chemistry*, vol. 84, pp. 2825–2829, Mar. 2012.

[176] Legendre, L. A., Bienvenue, J. M., Roper, M. G., Ferrance, J. P., and Landers, J. P., "A simple, valveless microfluidic sample preparation device for extraction and amplification of DNA from nanoliter-volume samples," *Analytical Chemistry*, vol. 78, pp. 1444–1451, Mar. 2006.

[177] Nair, R., Ngangan, A. V., Kemp, M. L., and McDevitt, T. C., "Gene expression signatures of extracellular matrix and growth factors during embryonic stem cell differentiation," *PLoS ONE*, vol. 7, p. e42580, Oct. 2012.

[178] Phaneuf, C. R., Pak, N., and Forest, C. R., "Modeling radiative heating of liquids in microchip reaction chambers," *Sensors and Actuators A: Physical*, vol. 167, pp. 531–536, June 2011.

[179] Phaneuf, C. R. and Forest, C. R., "Direct, high-speed milling of polymer microchamber arrays," in *Proceedings of the 25th Annual Meeting of the American Society for Precision Engineering, Atlanta, GA*, vol. 50, pp. 345–347, 2010.